UNIONE EUROPEA
Fondo Sociale Europeo

UNIVERSITÀ DEGLI STUDI DI TORINO

DIPARTIMENTO DI SCIENZE MEDICHE

DOTTORATO DI RICERCA IN FISIOPATOLOGIA MEDICA

CICLO: 37°

TITOLO DELLA TESI: Regulatory Mechanisms of Chemotherapy-induced Cardiotoxicity and CFTR Trafficking: Molecular Insights for Translational Medicine”

TESI PRESENTATA DA: Marco Mergiotti

SUPERVISORE: Prof. Alessandra Ghigo

COORDINATORE DEL DOTTORATO: Prof. Benedetta Bussolati

ANNI ACCADEMICI: 2022-2024

SETTORE SCIENTIFICO-DISCIPLINARE DI AFFERENZA*: MED04

(*N.B. Nel caso di più settori disciplinari interessati, deve essere indicato quello più presente nella trattazione della tesi).

Progetto svolto grazie al sostegno finanziario del **Programma Operativo Nazionale Ricerca e Innovazione 2014-2020 (CCI2014IT16M2OP005), risorse FSE REACT-EU, Azione IV.5 “Dottorati su tematiche Green”**

Ministero dell'Università e della Ricerca

PON RICERCA E INNOVAZIONE 2014 - 2020

REACT EU

UNIVERSITÀ DI TORINO

Index

Part I

Unveiling transcriptional changes of doxorubicin-induced cardiotoxicity at single-cell resolution

ABSTRACT

Background

Doxorubicin (DOX) is a potent chemotherapy agent used to treat various malignancies, but its clinical application is limited by dose-dependent cardiotoxicity, which can lead to heart failure and increased mortality in cancer survivors. Despite extensive research, the molecular basis of DOX-induced cardiotoxicity (DIC) remains unclear, as no study has yet conducted an unbiased characterization of the transcriptional landscape of DOX-treated hearts, distinguishing an early but reversible phase of the disease.

Aim

Identifying early transcriptional changes in DIC could be key to developing new cardioprotective strategies aimed at preventing disease progression.

Methods

Using our established murine model of DIC, BALB/c mice received either saline or DOX (3 weekly injections of 4 mg/kg). Hearts were collected at 3 days (DOX_3D, early) or 6 weeks (DOX_6W, late) post-injection. Nuclei isolated from frozen hearts underwent single-nuclei transcriptomic analysis (snRNAseq). Seurat pipeline along with Drug2cell, Milo and CellChat tools were used for downstream bioinformatic analysis.

Results

SnRNAseq of 12 hearts identified 8 major cell types, including cardiomyocytes (CM), endothelial (EC) and mural cells, fibroblasts (FB), immune cells (B, T, and myeloid, MYE), and neuronal-like cells. To identify key cell populations targeted by DOX, we applied Drug2Cell, which revealed CM, FB, and MYE as primarily affected. Milo analysis further highlighted significant perturbations in these cell types, suggesting that DOX-induced transcriptomic alterations driving DIC primarily occur within these populations. CellChat was used to further explore these key cell types and predict major pathogenic signaling in response to DOX. Interestingly, CellChat analysis mapped an intricate crosstalk between FB and immune cells, highlighting pro-fibrotic remodeling and a complex immune response involving different subtypes of cardiac resident myeloid cells. Notably, at DOX-6 weeks, CD8+ T cells were found to contribute to cytotoxic signaling directed toward a stressed cardiomyocyte population (CM_Stressed), characterized by elevated cardiac stress markers such as Nppb and Myh7. ScFate trajectory analysis of CM uncovered two unbiased clusters of gene signatures, depicting a progression from a CM_Basal cell state to CM_Stressed, suggesting that maladaptive cardiac remodeling driven by DOX underlies profound and specific transcriptional changes. Among these gene signatures, we identified Golgi-associated kinase 1B (*Gask1b*), which has never been associated with cardiac pathophysiology, as one of the top differentially upregulated genes specifically in CM in both 3-day and 6-week DOX-treated groups. Importantly, functional validation in zebrafish and mice showed that Gask1b silencing partially prevents DOX-induced decline in heart function, identifying Gask1b as a

potential novel player in DIC. Finally, snRNAseq data and immunohistochemistry staining from human cardiotoxic hearts confirmed Gask1b overexpression following anthracycline treatment, highlighting Gask1b as a novel marker of DIC in humans.

Conclusions

We generated a single-nucleus dataset of DOX-treated mouse hearts and identified transcriptional changes driven by DOX in CM at early and late stages of the disease. Furthermore, we identified Gask1b gene, whose role in cardiac pathophysiology was previously unappreciated, as a new potential marker and determinant of DIC.

1. INTRODUCTION

1.1 The Rise of Cardio-Oncology: Addressing Cardiotoxicity in Cancer Survivors

Cardiovascular diseases (CVD) and cancers are the two leading causes of morbidity and mortality worldwide, particularly in aging populations (Alam et al. 2020). These diseases are closely interlinked, sharing several risk factors such as obesity, hypertension, diabetes, smoking, and genetic predispositions. Both also exhibit similar pathological hallmarks, including elevated oxidative stress, chronic inflammation, and abnormal neurohormonal activation (DeBoer 2019). Despite the rising incidence of cancer, its mortality rates have steadily declined over the past three decades. Since 1991, the cancer mortality rate has decreased by 33%, saving an estimated 3.8 million lives as of 2023 (Siegel et al. 2023); the 10-year survival rate for individuals diagnosed with cancer now exceeds 50% on average and, for certain malignancies, such as lymphoma and leukemia, survival rates reach as high as 90% in childhood cancer survivors (Hemminki et al. 2024), (Tonorezos and Marcil 2023). This progress is largely due to advancements in early and precise diagnosis as well as development of multimodal therapies, including chemotherapy, radiation, and targeted treatments, which have significantly enhanced effectiveness and precision (Chrischilles et al. 2017, Tarantino and Tolaney 2024). While these therapies have dramatically improved survival rates, this has come with a growing awareness of the long-term health complications faced by cancer survivors. Studies have highlighted that many cancer survivors experience severe and life-threatening, late effects of treatment, including secondary malignancies, endocrine dysfunction, cognitive impairments and, most importantly, cardiotoxicity (Chrischilles et al. 2017), (Chang et al. 2022). Remarkably, both pediatric and adult cancer survivors exhibit a significantly higher prevalence of CVDs, including heart failure, ischemic heart disease, and arrhythmias, when compared to individuals in the general population (Wilcox et al. 2024), (Lyon et al. 2022). Follow-up studies on patients in cancer remission revealed that mortality due to CVD reached 20–30% after 15 years, surpassing the mortality of the primary cancers (Ramin et al. 2021). On the other hand, acute cardiovascular toxicity may also considerably affect the overall prognosis of cancer patients, as severe cases of toxicity can lead to premature termination of cancer treatments, thereby increasing the risk of cancer recurrence and all-cause mortality (López-Sendón et al. 2020). Consequently, higher burden of patients requires ongoing cardiovascular care, frequent hospitalizations, and increased healthcare resource utilization, underlying a critical need for long-term cardiovascular monitoring and specialized care to improve quality of life and survival for these patients (Lyon et al. 2022). In response to these challenges, cardio-oncology has emerged to primarily address cardiovascular risks associated with cancer therapies. This field focuses on preventing and managing treatment-induced cardiotoxicity while maintaining the effectiveness of cancer treatments. Meanwhile, there is an urgent need to intensify current research and translational studies in cardio-oncology, as understanding the molecular mechanisms of this cardiotoxicity is essential for developing targeted interventions and identifying risk factors, paving the way for personalized and safer cancer treatments.

1.2 Anthracycline Chemotherapy-related Cardiac Dysfunction

It is now widely recognised that nearly all anti-cancer treatments, including chemotherapy, targeted therapy and radiotherapy, have adverse effects on the heart (Moslehi 2016). Classes of anti-cancer therapies with the most well-documented cardiac impacts include anthracyclines, HER2-targeted therapies, proteasome inhibitors, vascular endothelial growth factor inhibitors, BCR-ABL inhibitors, and RAF and MEK inhibitors (Lyon et al. 2022). Among these, the most effective chemotherapeutics are anthracyclines, which are widely used for a variety of cancers, but are notorious for their dose-dependent cardiotoxic effects. In anthracycline-induced cardiotoxicity (AIC), cardiac dysfunction progresses from an initial subclinical myocardial damage and asymptomatic reduction in left ventricular ejection fraction (LVEF), to an irreversible state of end-stage heart failure in which treatments are no longer effective (Sawicki et al. 2021) (Figure 1). While most research has focused on preventing or treating late-stage cardiac damage, understanding the earliest stages of injury—before the onset of severe clinical symptoms—is critical for developing effective cardioprotective strategies. This early phase of AIC is particularly crucial, as it may involve subtle molecular alterations that serve as initial triggers for disease progression. Identifying and characterizing these changes could provide crucial insights into the pathways leading to irreversible cardiac dysfunction, presenting opportunities for early intervention when damage remains reversible and cardiac function can still be preserved. Among these anthracycline chemotherapeutics, doxorubicin (DOX) is one of the most widely used, due to its broad spectrum of effectiveness against both solid and liquid malignancies (Kciuk et al. 2023), (Sawicki et al. 2021). This study focuses on DOX-induced cardiotoxicity (DIC) (Zheng et al.), and the following introduction will explore the definition, current understanding of mechanisms, along with preventative and therapeutic strategies.

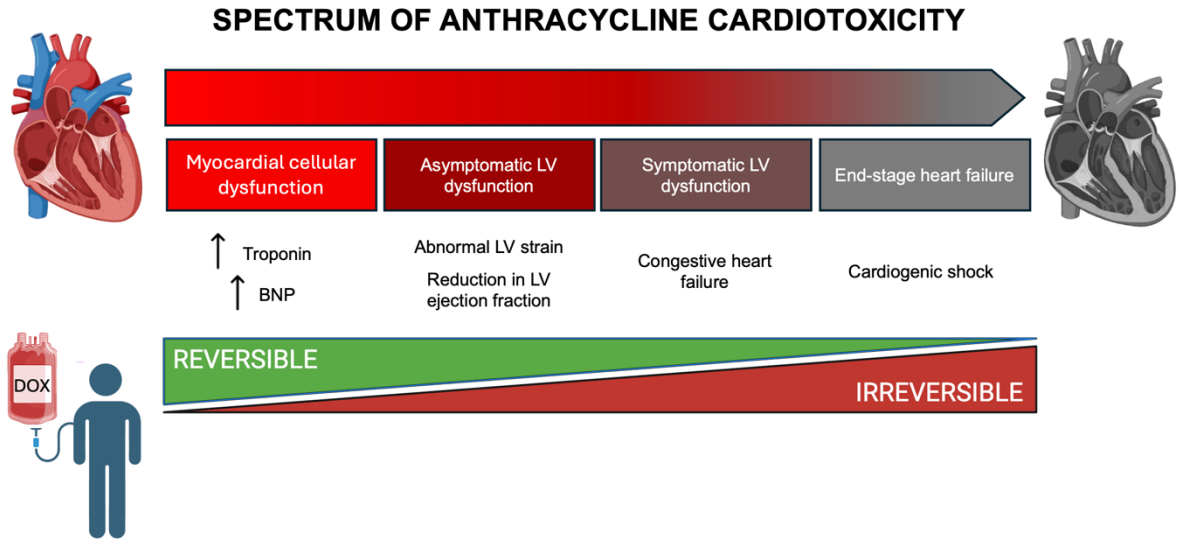

Figure A. The spectrum of anthracycline cardiotoxicity ranges from an asymptomatic phase in which the cardiac damage remains reversible and manageable, to an advanced stage of irreversible heart failure, at which point treatments become ineffective. Abbreviations: BNP, brain natriuretic peptide; LV, left ventricular. (adapted from Sawicki et al., 2022)

1.3 Mechanisms of Doxorubicin-induced Cardiotoxicity

Preclinical and clinical studies have proposed several mechanisms underlying DIC. DOX is a highly potent medication for tumour targeting, mainly through intercalating into the nucleotides of tumour cells and catalytically inhibiting topoisomerase 2α (Top 2α) after DNA cleavage, thus preventing DNA and RNA synthesis and causing DNA double strand breaks (DSBs) (K M Tewey 1984), (Van Ravenstein et al. 2022). Additionally, DOX also induces overproduction of reactive oxygen species (ROS), causing DNA damage and mitochondria dysfunction in tumour cells (Ewer and Ewer 2015). DOX cardiotoxicity shares a number of mechanisms with its tumour killing effect, but due to the difference of cardiomyocytes and cancer cells in nature, the killing/impairment pathways are not identical (Golforoush and Schneider 2020). Below, detailed mechanisms of DOX toxicity in cardiac cells are listed, starting with the major pathological hallmarks (Figure B) including DNA damage, oxidative stress and mitochondrial dysfunction, followed by a summary of various cell death pathways involved in DIC along with current therapeutic strategies.

1.3.1 Pathological Hallmarks

DNA Damage and Transcription Inhibition

DOX intercalates into DNA and inhibits topoisomerase 2 (Top 2), disrupting DNA replication, transcription, and repair. Top 2α and Topoisomerase 2β (Top 2β) are isoforms of Top 2 expressed in cells in different cell cycle position. Top 2α is a marker for proliferative cells (e.g., tumour cells) while Top 2β is mostly expressed in quiescent cells (e.g., cardiomyocytes)(Tan et al. 1992). As a matter of fact, the inhibition of Top 2β in cardiomyocytes has been proved to be the central event of DOX cardiotoxicity (Henriksen 2018). Moreover, Top 2β inhibition in quiescent cardiomyocytes induces DNA double-strand breaks (DSBs), activating p53-dependent apoptosis (Zhang et al. 2012), (Zhu et al. 2009). Interestingly, Top2β cardiac-specific knockout models show reduced DSBs and mitochondrial dysfunction. Additionally, Top 2β inhibition suppresses the transcription of genes regulating antioxidant defence and mitochondrial biogenesis, contributing to oxidative stress and mitochondrial impairment (Zhang et al. 2012)

Oxidative Stress

The “ROS and iron hypothesis” proposes that DOX undergoes redox cycling, generating excessive ROS through quinone/semiquinone transitions and Fenton reactions. These processes produce lipid peroxides and damage cellular and mitochondrial membranes, leading to cell death (Doroshow and Davies 1986). DOX also forms complex with iron in the cell and releases free radicals into the cytoplasm in either reducing-system dependent or independent way (Keizer et al. 1990) However, antioxidant and iron chelation therapies alone failed to fully prevent DOX-induced cardiac dysfunction, suggesting oxidative stress is only part of the mechanism (Martin et al. 2009).

Mitochondrial Dysfunction

In recent years, more attention has been driven to the mitochondrial determinants of DOX cardiotoxicity (Wallace et al. 2020). DOX preferentially accumulates in mitochondria due to its affinity for cardiolipin, thus directly disrupting mitochondrial function through direct inhibition of complex I, a key component of the electron transport chain, along with excess ROS generation, leading to oxidative stress that damages mitochondrial DNA, proteins and lipids, which ultimately compromise cellular energy production (Rawat et al. 2021). Additionally, DOX interferes with mitochondrial quality control (Wu et al. 2023), inhibiting mitochondrial biogenesis through the aforementioned PGC1α axis (Zhang et al. 2012), inducing excessive mitochondrial fission by activating dynamin-related protein 1 (DRP1) and down-regulating key fusion protein mitofusin 2 (Mfn2) (Ding et al. 2022).

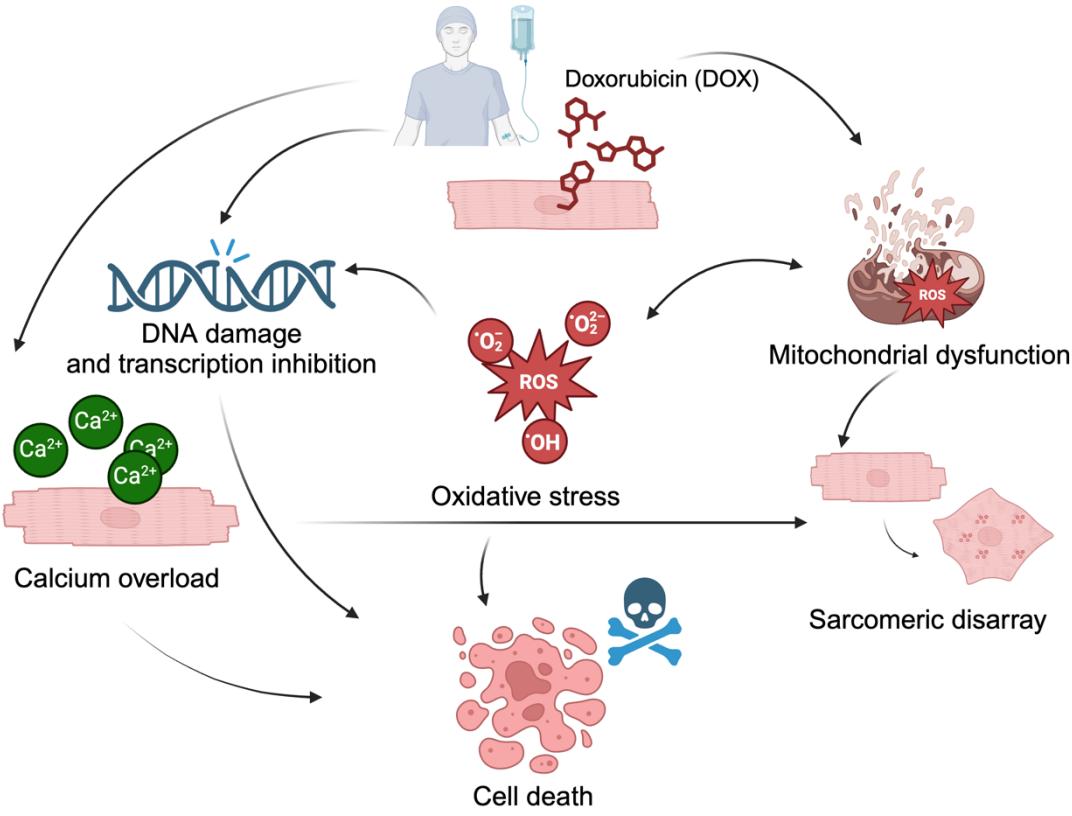

Figure B. Upon DOX exposure in cardiomyocytes, DNA damage, oxidative stress, mitochondrial dysfunction, and calcium overload contribute to cardiomyocte injury. DOX intercalates into DNA, inhibiting topoisomerase 2β (Top2β), leading to double-strand breaks (DSBs) and p53-dependent apoptosis. It generates reactive oxygen species (ROS), causing oxidative stress and mitochondrial dysfunction by impairing the electron transport chain (ETC). DOX also disrupts calcium homeostasis by activating RYR2 and inhibiting SERCA2a, leading to calpain activation, sarcomeric disarray, and apoptosis via calcium-dependent signaling. Mitochondrial dysfunction contribute to ATP depletion, which can indirectly affects sarcomeric structure These pathological hallmarks collectively drive to cardiomyocyte cell death and DOX-induced cardiomyopathy.

Calcium Overload and sarcomeric disarray

Calcium overload is also a critical contributor of the DOX cytotoxicity, particularly for cardiomyocytes. DOX binds to the cardiac ryanodine receptor (RYR2) on the sarcoplasmic reticulum (Hao et al.),

increasing calcium release. In parallel, also down-regulates the sarcoplasmic/endoplasmic reticulum calcium ATPase 1 (SERCA2a), a key protein for calcium reuptake into the SR, exacerbating the calcium overload (Saeki et al. 2002), (Hanna et al. 2014). This calcium dyshomeostasis impairs cardiac contractility and promotes cell death. Moreover, DOX-induced calcium overload is known to activate calpains, degrading sarcomeric proteins like titin**,** leading to myofilament instability, cardiac atrophy, and sarcomeric disarray (Lim et al. 2004), (Wallace et al. 2020).

1.3.2 Dis-regulated Cell Death Pathways

Apoptosis

Numerous studies demonstrated that the apoptosis is a major form of regulated cell death (RCD) in DOX-induced cardiotoxicity. DOX-induced DNA damage, oxidative stress and mitochondrial dysfunction all contribute to the development of apoptosis. Apoptosis consists of the intrinsic and extrinsic pathways, both of which are activated by DOX (Wallace et al. 2020). In the intrinsic pathway, DOX undergoes redox cycling particularly in mitochondria, leading to excessive ROS. Lipid peroxides generated on the plasma and mitochondrial membrane also contributed to the oxidative stress (Tadokoro et al. 2020). Interestingly, pharmacological inhibition of the pro-apoptotic factor BAX via BAI1 has been reported as a promising target to mitigate DOX cardiotoxicity (Amgalan et al. 2020). On the other hand, over-expression of BCL2, serving as an anti-apoptotic factor, protects against DOX-induced cardiomyopathy (Yoshida, 2009 #49). In the extrinsic pathway, DOX triggers the extrinsic apoptotic pathway through activating nuclear factor of activated T cells (NFAT) (Kalivendi et al. 2005), resulting in the up-regulation of Fas, as well as p53 (Nakamura et al. 2000).

Necroptosis

Necroptosis is a form of regulated necrosis that shares some features similar to apoptosis but occurs independently of caspase activation. In this context, DOX has been shown to increase TNFα, activating TNFR1, TRADD, and RIPK1, which phosphorylates RIPK3 to form the necrosome complex. RIPK3 phosphorylates MLKL, disrupting the plasma membrane and releasing inflammatory factors (Christidi and Brunham 2021), (Dhingra et al. 2022). Notably, RIPK3 is up-regulated following DOX treatment in the heart, and calcium/calmodulin-dependent protein kinase II (CaMKII) was recently identified as a RIPK3 substrate that regulates mPTP opening, coupling necroptosis and apoptosis pathways (Zhang et al. 2016). In line with these findings, Necroptosis-specific inhibitors like Nec-1 has been shown to restore cardiomyocyte viability, indicating the critical role of necroptosis in DOX cardiotoxicity (Yu et al. 2020).

Pyroptosis

Pyroptosis is defined as cell death associated with inflammation (Bergsbaken et al. 2009). It is characterised by activation of NLR family pyrin domain containing 3 (NLRP3), followed by caspase 1-mediated cleavage of the gasdermin D (GSDMD) and formation of nonselective pores on plasma membrane, resulting in cell rupture and release of inflammatory factors (Bergsbaken et al. 2009). Importantly, inhibition of NLRP3 via pharmacological inhibitors, exosomes, or sirtuin 1 (SIRT1)

activation both attenuated DOX-induced cell death in cardiomyocytes (Meng et al. 2019), (Dargani and Singla 2019). Alternatively, DOX increases BCL2 interacting protein 3 (BNIP3) expression in cardiomyocytes, which not only promotes cell death via mitochondrial pathways (Dhingra et al. 2014) (Dhingra et al., 2014), but also activates caspase 3 and leads to GSDME-dependent pyroptosis (Zheng and Kanneganti 2020).

Ferroptosis

Ferroptosis is iron-dependent RCD characterized by lipid peroxidation and ROS accumulation. Ferroptosis is driven by iron-dependent production of ROS, resulting in peroxidation of fatty acids in cellular and mitochondrial membrane, disrupting membrane integrity and eventually leading to cell death DOX disrupts iron homeostasis by forming iron complexes, downregulating ferritin and ferroportin, and increasing transferrin receptor expression, leading to mitochondrial iron overload (Dixon et al. 2012). DOX interferes with cells' iron homeostasis through direct binding to iron, forming a DOX-iron complex which catalyses the conversion of oxygen into ROS such as hydroxyl radicals (Fenton redox) (Xu et al. 2005). Indeed, DOX treatment induced the accumulation of iron in the heart particularly in mitochondria, as found in the heart biopsy specimens from patients with DOX-induced cardiomyopathy (Ichikawa et al. 2014). Notably, the only FDA-approved cardioprotectant against anthracycline is Dexrazoxane (DRZ), which acts at least in part by chelating iron and mitigating iron overload in the heart during DOX treatment (Yu et al. 2020).

1.4 Critical Gaps in the Existing Knowledge

Despite numerous mechanistic studies conducted over the past two decades, few therapeutics have been developed to specifically target DIC. This underscores a pressing need to further elucidate the molecular mechanisms underlying DOX-induced cardiotoxicity. While current therapeutic strategies have been proposed, their efficacy remains contentious or limited, failing to comprehensively prevent cardiomyocyte loss or provide robust cardioprotection.

1.4.1 Current Preventative Therapeutic Countermeasures

Preventative and therapeutic strategies for mitigating anthracycline-induced cardiac dysfunction primarily aim to reduce DOX toxicity or protect cardiac function (Vejpongsa and Yeh 2014). Efforts to optimize DOX administration include limiting cumulative doses, prolonging infusion times (El-Kareh and Secomb, 2000), and utilizing liposomal formulations to alter pharmacokinetics and tissue distribution, which minimize uptake by healthy tissues while enhancing tumor accumulation (Makwana et al. 2021). Liposomal DOX has demonstrated reduced cardiotoxicity compared to conventional formulations, potentially due to its role in inducing interferon-mediated DNA damage resistance (Gyöngyösi et al. 2020). However, DOX still retains a severe cardiotoxicity, necessitating the exploration of additional cardioprotective strategies and novel therapeutic agents to further mitigate its adverse effect.

Conventional heart failure therapies, such as angiotensin-converting enzyme (ACE) inhibitors, angiotensin receptor blockers (ARB), and β-blockers, have also been used to mitigate DOX-induced left ventricular dysfunction (Brown et al. 2020), (Lyon et al. 2022). Among these, enalapril, an ACE

inhibitor, improves cardiac remodeling and mitochondrial function in DOX-treated heartsm(Hiona et al. 2011), although its ability to consistently preserve left ventricular function in anthracycline-treated patients remains debated (Zhang, 2020 #69). Carvedilol, a β-blocker with antioxidant properties, prevents oxidative stress and apoptosis in vitro (Spallarossa et al. 2004) and reduces troponin release in patients, although its effects on left ventricular ejection fraction (LVEF) remain inconclusive(Ayub-Ferreira et al. 2020). Recent large-scale clinical trial and its follow up study showed that Carvedilol administration did not preserve LVEF at either early onset or during two-year follow-up, but significantly reduced Troponin release and improved diastolic function in patients (Ayub-Ferreira et al. 2020), (Avila et al. 2018).

DRZ is the only approved drug specifically targeting DOX-induced cardiotoxicity (Hensley et al. 1999) despite controversies in mitigating the tumour-targeting effect of DOX (Henriksen 2018). Initially believed to act as an iron chelator, DRZ's cardioprotective mechanism was later linked to its ability to block DOX interaction with Top 2β, thereby preventing cardiomyocyte damage (Lyu et al. 2007).

Other emerging cardioprotective agents include sodium-glucose co-transporter 2 (SGLT2) inhibitors, which, beyond their glucose-lowering effects, have demonstrated anti-inflammatory and antifibrotic benefits in DOX-treated models (Quagliariello et al. 2021). Early studies suggest SGLT2 inhibitors like Empagliflozin may reduce cardiac events in patients receiving anthracyclines, though larger trials are needed (Daniele et al. 2024). Moreover, statins, traditionally used to lower cholesterol, have also shown potential in preventing DOX-induced LVEF decline, with meta-analyses supporting their role as cardioprotective agents(Shahid et al. 2021). Additionally, remote ischemic conditioning (RIC), a non-invasive therapy involving intermittent limb ischemia, has shown promise in preclinical models, reducing fibrosis and preserving cardiac function following DOX administration (Galán-Arriola et al. 2021). A large clinical trial is currently evaluating RIC in patients at risk of anthracycline-induced cardiotoxicity(Moreno-Arciniegas et al. 2024).

Despite these advances, most current strategies rely on repurposing treatments initially developed for other conditions, with limited ability to prevent irreversible cardiomyocyte loss. This limitation underscores the urgent need for novel therapeutic targets to preserve myocardial integrity and reduce the long-term cardiac burden for cancer survivors.

Type of Therapy	Outcome in DOX-Induced Cardiotoxicity	Reference
Dosing Strategies	Limiting cumulative doses, prolonging infusion times to reduce toxicity	*El-Kareh and Secomb, 2000*
Liposomal DOX	Reduces cardiotoxicity, enhances tumor accumulation	*Makwana et al., 2021; Gyöngyösi et al., 2020*

ACE Inhibitors (e.g., Enalapril)	Improves cardiac remodeling, mitochondrial function; mixed results on LVEF preservation	*Brown et al., 2020; Lyon et al., 2022; Hiona et al., 2011; Zhang et al., 2020*
β-Blockers (e.g., Carvedilol)	Prevents oxidative stress, apoptosis; reduces troponin release but inconsistent effect on LVEF	*Spallarossa et al., 2004; Ayub-Ferreira et al.,, 2020; Avila et al., 2018*
Dexrazoxane (DRZ)	Prevents cardiomyocyte damage by blocking DOX interaction with Top 2β. Only drug approved by FDA.	*Hensley et al., 1999; Henriksen et al., 2018; Lyu et al., 2007*
SGLT2 Inhibitors (e.g., Empagliflozin)	Demonstrates anti-inflammatory, antifibrotic effects; potential reduction in cardiac events	*Quagliariello et al., 2021; Daniele et al., 2024*
Statins	Potentially prevents LVEF decline	*Shahid et al., 2021*
Remote Ischemic Conditioning (RIC)	Reduces fibrosis, preserves cardiac function; under clinical evaluation	*Galán-Arriola et al., 2021; Moreno-Arciniegas et al., 2024*

Table 1. Preventative and Therapeutic Strategies for DOX-Induced Cardiotoxicity

Summary of current approaches to mitigate DOX-induced cardiac dysfunction, including dosing strategies, cardioprotective agents, and emerging therapies. While some directly target DOX toxicity, most are repurposed cardiovascular drugs with limited ability to prevent irreversible cardiomyocyte death.

1.4.2 Comprehensive Profiling of Doxorubicin-treated Hearts

DOX is implicated in multiple regulated cell death pathways that mediate its toxicity in cardiomyocytes. However, the molecular mediators and the mechanisms by which these pathways intersect remain poorly understood. Moreover, the lack of efficacy of conventional treatments implemented for heart failure underscores the notion that DIC may evolve differently from other cardiomyopathies, highlighting its distinct and unique disease profile. In this regard, implementing robust preclinical cardiovascular models, from cellular systems to whole animal platforms, is essential for both mechanistic and phenotypic investigations, with an ultimate goal of identifying novel biomarker and therapeutic targets, and developing effective therapies to improve patient outcomes (Asnani 2021). Thus, a comprehensive dissection of the molecular changes driving these processes, ideally through unbiased profiling approaches, could uncover critical insights into their regulation and interplay. Moreover, while cardiomyocytes are thought to be the main target of DOX-induced cardiotoxicity, other cell types and the interaction between cells also play a role in the pathological processes. However, little is known about how DOX alters the transcriptome of each cardiac cell type and their interactions, nor has it been

characterised the heterogeneities of each cell type in response to DOX. This critical research gap calls for an unbiased, systematic profiling of DOX-injured hearts on single-cell level.

1.5 Single-cell/single-nucleus to Decipher Doxorubin-induced Cardiotoxicity

Single-cell RNA sequencing (scRNA-seq) is the state-of-art technology allowing transcriptomic profiling and analysis on each individual cell. One of the approaches to implement “single-cell” sequencing is via a microdroplet-based system where the transcripts of each cell can be encapsulated in a lipid droplet (Zheng et al. 2017). Due to large size of cardiomyocytes (~ 100 μm in length), it is difficult to capture the whole cell with microdroplet-based techniques (upper size limit for cells of ~ 25–40 μm) for scRNA-seq (Paik et al. 2020), without introducing a selection bias of only including small-sized CMs. However, single-nucleus RNA sequencing (snRNA-seq), which profiles the nuclei transcripts, provides an alternative allowing to capture and examine all cardiac cell types, including cardiomyocytes. Importantly, snRNA-seq generates overall similar molecular features with scRNA-seq in the adult human heart (Litvinukova et al. 2020). Therefore, it has been widely accepted for cardiac transcriptomics studies, and has provided a plethora of knowledge for both non-diseased and diseased human hearts (Litvinukova et al. 2020), (Tucker et al. 2020), (Kanemaru et al. 2023), (Reichart et al. 2022), (Wang et al, 2020). As part of the Human Cell Atlas scheme (Regev et al. 2017), a major ground-breaking study profiling 14 healthy human hearts provided to-date the largest cardiac cell reference emphasised the heterogeneity of cells, defined and annotated the major cell types in healthy human heart, identified distinct atrial and ventricular cell subtypes, and shed light on the cardiac vasculature and immune network (Litvinukova et al. 2020). Importantly, sc/snRNA-seq analysis provides unprecedented granularity, allowing examination further than cell type (well-established cellular lineages) level, but cell states (cellular subtypes with transient and/or functional cellular transcriptomics signatures) as well. DOX is known to interfere with various cell types, and the non-cardiomyocytes play a key role in mediating pathogenic tissue remodelling and inflammatory responses, contributing to DOX-induced cardiac dysfunction. To date, there has not been a systematic, single-cell level profiling of cardiac cells in response to DOX. Here, we used snRNA-seq to study the cardiac cellular landscape and molecular signatures in our previously established mouse model of DOX-induced cardiotoxicity, aiming to characterize key cellular and transcriptomic changes in the heart following DOX treatment, and to identify putative therapeutic targets. Our single-nucleus transcriptomic analysis identified a profound perturbation in intercellular crosstalk following DOX treatment, underscoring an activated fibroblast subset as key driver of ECM remodelling and a complex immune response axis involving different immune cell subpopulations, and a stressed cardiomyocyte cell state. Furthermore, we identified Gask1b, whose role in cardiac pathophysiology was previously unappreciated, as a new potential marker and determinant of DOX-induced cardiomyocyte injury.

2. MATERIALS AND METHODS

2.1 Animal model establishment and sample preparation

In vivo treatment

Wild-type BALB/c female mice aged from 8 to 10 weeks were used for this study. Mice were housed in groups and had unrestricted access to standard chow and water and were kept in a controlled environment with a 12-hr light/12-hr dark cycle.

Mice were treated with Doxorubicin as described previously (Li et al. 2018). Briefly, to replicate human therapeutic regimens, mice were administered a cumulative dose of 12 mg/kg of Doxorubicin through three weekly intraperitoneal (IP) injections (4 mg/kg on Day 0, 7, and 14), and their survival was monitored daily. Mouse hearts were collected at either 3 days (DOX_3D) or 6 weeks (DOX_6W) after the first injection. Mice cardiac function was assessed by echocardiography (Fractional shortening > 35% as normal; < 20% as impaired) before starting the treatment and before sacrificing.

Sample preparation

Mouse hearts were isolated and the atria were removed. Ventricles were minced using a razor blade and immediately transferred onto dry ice to snap freeze. Frozen tissue was then stored below -80°C for nuclei isolation.

Echocardiography

Cardiac function was evaluated in mice anesthetized with 1% isoflurane using with a Vevo 2100 High Resolution Imaging System (Visual Sonics Inc, Toronto, Canada) equipped with a 30-MHz probe (MS550D) (VisualSonics, Toronto, Canada). Echocardiographic parameters were measured under the long-axis M-mode when heart rate was about 450 bpm. Fractional shortening (FS) was calculated as FS (%) = [(LVIDED - LVIDES)/ LVIDED] x 100. All these measurements were performed by a single experienced technician in a blinded manner.

2.2 Single nuclei isolation

Nuclei Isolation Medium (NIM) was pre-made with 250 mM sucrose, 25 mM KCl, 5 mM $MgCl_2$ and 10 mM Tris using nuclease-free water. Frozen tissue was first broken into smaller pieces using pre-cooled pestle and mortar and transferred to a pre-cooled Dounce homogeniser filled with 3 mL of Homogenisation Buffer (HB, freshly made by adding 1 μM DTT, 1X Complete Protease Inhibitor Cocktail, 0.4 U/μL RNasin® Plus Ribonuclease Inhibitor and 0.2 U/μL SUPERase•In™ RNase Inhibitor to NIM). Tissue was homogenised with 8 strokes of the loose pestle and tight pestle each and filtered through a 40 μm cell strainer. The homogeniser was washed twice with 1 mL of HB and the washes were pooled together with the filtered solution. Then, nuclei suspension was centrifuged at 500 × g for 5 mins at 4˚C. Supernatant was removed and the pellet was resuspended with 500 uL Storage Buffer (SB, freshly made by adding 4% BSA and 0.2 U/μL Protector RNase Inhibitor to PBS) and transferred to a FACS tube. Nuclei were stained with NucBlue and sorted using 85N nozzle into a collection tube

containing 2 mL SB. Sorting was performed by P. Chaves in house or by LMS/NIHR Imperial Biomedical Research Centre Flow Cytometry Facility staff.

After sorting, nuclei in collection tube were centrifuged at 500 × g for 5 mins at 4˚C, counted with Trypan Blue and adjusted to concentration of 1,000 nuclei/µL.

2.3 Chromium 10X library preparation and sequencing

Samples used for this study were kindly processed by S. Barnett and R. T. Rivalta at Imperial College London, using Chromium Next GEM Single Cell 3' Kit v3.1 (10x Genomics, 1000268) and Chromium Next GEM Chip G Single Cell Kit (10x Genomics, 1000120), following manufacturer's instructions.

GEM generation and reverse transcription

To aim for 5,000 nuclei recovery, 8.3 µL nuclei suspension (~ 8,300 nuclei) was partitioned into Gel Beads-in-emulsion (GEMs). Each Gel Bead contains oligo nucleotides consisting of a TruSeq Read 1 sequence, a 16 nt 10x barcode that allows single-cell/nucleus indexing, a 12 nt unique molecular identifier (UMI) to label each transcript, and a 30 nt poly (dT) primer to capture poly-adenylated mRNA.

GEM generation Master Mix was prepared by mixing 18.8 µL RT Reagent B, 2.4 µL Template Switch Oligo, 2 µL Reducing Agent B and 8.7 µL RT Enzyme C per sample. Nuclei suspension + Master Mix, Gel Beads and Partitioning Oil were loaded to the corresponding wells on Chromium Next GEM Chip G, and processed on Chromium Controller (10x Genomics, GCG-SR-1) to generate GEMs.

Immediately after GEM generation, index primers were released from Gel Beads and were mixed with lysed nuclei and RT reagents. Samples were incubated in Veriti™ 96-Well Thermal Cycler (Applied Biosystems, 4375786), where reverse transcription was performed at 53˚C for 45 mins, followed by enzyme inactivation at 85˚C for 5 mins.

cDNA cleanup and amplification

Barcoded cDNA samples obtained from RT were washed with 125 µL Recovery Agent via phase separation. Then, Dynabeads Cleanup Mix (prepared by mixing 8 µL Dynabeads™ MyOne™ SILANE with 5 µL Reducing Agent B, 5 µL nuclease-free water and 182 µL Cleanup Buffer per sample) was used to bind and purify first-strand cDNA via magnet separation. cDNA pellet was washed with 80% ethanol twice and eluted with 35.5 µL Elution Solution I (0.1% Tween 20 and 1% Reducing Agent B in Buffer EB).

For cDNA amplification, each sample (35 µL) was mixed with 50 µL Amp Mix and 15 µL cDNA Primers, and incubated in a thermal cycler following the programme listed in Table 1. Amplified cDNAs were then cleaned up with 0.6X SPRIselect Reagent via magnetic separation, washed twice with 80% ethanol, air-dried and eluted with 40 µL Buffer EB.

Temperature	Time	
98˚C	3 minutes	/
98˚C	15 seconds	12 cycles
63˚C	20 seconds	
72˚C	1 minute	
72˚C	1 minute	/
4˚C	∞	/

Table 2. PCR programme for cDNA amplification

Library construction and sample indexing

25% of purified cDNA per sample was used for library construction, which was tested to have comparable complexity with one generated with higher proportion of total cDNA. For fragmentation, 10 µL cDNA of each sample was mixed with 5 µL Fragmentation Buffer, 10 µL Fragmentation Enzyme and 25 µL Buffer EB, and incubated in a thermal cycler pre-cooled to 4˚C. Fragmentation was performed at 32˚C for 5 mins, followed by end repair and A-tailing at 65˚C for 30 mins. Fragmented samples were then cleaned up with 0.6X and 0.8X SPRIselect Reagent successively via magnetic separation, washed twice with 80% ethanol and eluted with 50 µL Buffer EB.

For adaptor ligation, each sample (50 µL) was mixed with 20 µL Ligation Buffer, 10 µL DNA Ligase and 20 µL Adaptor Oligos, and incubated in a thermal cycler set to 20˚C for 15 mins. Post-ligation samples were then cleaned up with 0.8X SPRIselect Reagent via magnetic separation, washed twice with 80% ethanol, air-dried and eluted with 30.5 µL Buffer EB.

Samples were indexed with using Single Index Kit T Set A (10x Genomics, 1000213). For indexing, each sample (30 µL) was mixed with 50 µL Amp Mix and 10 µL SI Primer, and incubated in a thermal cycler following the protocol listed in Table 2. Indexed samples were then cleaned up with 0.6X and 0.8X SPRIselect Reagent successively via magnetic separation, washed twice with 80% ethanol and eluted with 35.5 µL Buffer EB.

Temperature	**Time**	
98˚C	45 seconds	/

98˚C	20 seconds	Cycle number determined by cDNA input, ranging from 14–15
54˚C	30 seconds	
72˚C	20 seconds	
72˚C	1 minute	/
4˚C	∞	/

Table 3. PCR programme for sample indexing

Sequencing

Indexed samples were sequenced using Illumina NovaSeq 2 × 150 bp configuration, targeting 250 million reads per sample (50,000 reads per nucleus × 5,000 nuclei). Sequencing and sample de-multiplexing were performed by Genewiz.

2.4 Pre-processing and quality control of single-nucleus transcriptomics data

Transcriptome alignment

Cell Ranger 3.1.0 (10x Genomics) was used to align FASTQ files to the mouse reference genome mm10-2020-A (10x Genomics, generated based on GENECODE vM23 and Ensembl 98), identify and filter barcodes and UMIs. A gene-by-barcode count matrix was generated for each sample sequenced, together with an estimated number of nuclei inferred from Barcode Rank Plot.

Background removal

Barcoded droplets inevitably contain a certain amount of ambient RNA introduced during tissue processing, which is shown as an “empty droplet plateau” in CellRanger Barcode Rank Plots (Figure C A). To reduce the number of background transcripts and their interference to downstream analyses, count matrices produced by CellRanger were examined and cleaned up by CellBender 0.2.0, a pipeline that learns the ambient RNA profile from data, determines the probability of a barcoded droplet containing real cells/nuclei, and generates a new count matrix after subtracting background (Fleming et al., 2023). Each count matrix was trained with 150 epochs at the learning rate of 5×10^{-5}, and barcodes with “cell probability” > 90% were regarded to contain cells/nuclei (Figure C-B). This corresponds to a false positive rate (FPR) of 0.1, where level of background removal was optimal without sacrificing true signals. Expected nuclei and total droplets included for each sample were manually determined from the CellRanger Barcode Rank Plots. R package Seurat 4.0.2 was used as the main platform for further data pre-processing and downstream analyses (Hao et al. 2024). Individual Seurat objects containing CellBender-corrected count matrix and metadata were generated for each sample.

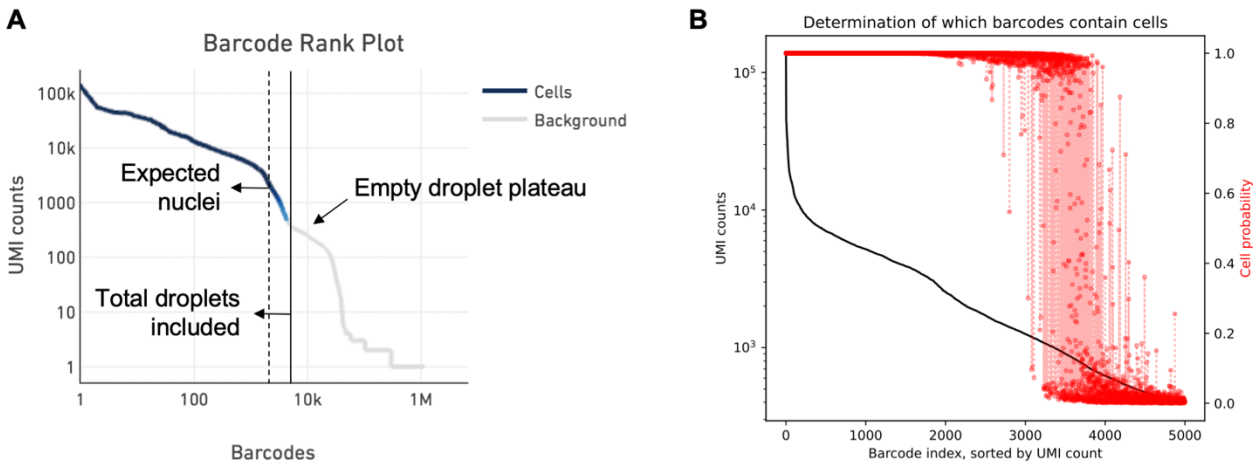

Figure C. CellBender correction of count matrix generated using CellRanger. A, Representative CellRanger-reported barcode rank plot showing ranked barcoded droplets by the number of unique molecular identifier (UMI) each barcode contains. Dark blue colour indicates barcodes containing cells/nuclei, and grey colour indicates background. An "empty droplet plateau" indicating droplets containing only ambient RNA is typically seen between cells/nuclei and background. Dashed line indicates the number of expected nuclei, and solid line indicates the total droplets to be examined using CellBender, which were manually determined based on CellRanger result, typically covering a blue-grey gradient before empty droplet plateau. **B**, Representative CellBender report indicating the determination of CellBender examines all the included droplets and calculate probability for whether each barcoded droplet contains cells/nuclei (cell probability shown in red). Barcodes passing CellBender threshold were used to generate a corrected gene-count matrix.

Doublet detection and removal

Scrublet (Wolock et al. 2019) was applied to each sample separately to identify doublets and calculate a doublet score for each barcode. The predicted doublets were removed from the matrix before further filtering and analyses.

Quality control and filtering

Doublet-removed objects were firstly merged as one Seurat object. Then, key metrics of nuclei were used for quality control, including 1) number of UMI counts (N_counts); 2) number of genes (N_genes); 3) percentage of mitochondria-encoded genes (Mito%) and 4) percentage of ribosomal genes (Ribo%). Thresholds for each metric were empirically determined by the characteristics of cell types and distribution of the metrics (Table 4). Potential doublets (reflected by abnormally high number of counts and/or genes) and low-quality nuclei (low count and/or gene number, high mitochondrial/ribosomal gene percentage) were excluded from further analyses.

	N_counts	N_genes	Mito%	Ribo%
Global	(500, 15000)	(200, 6000)	< 2	< 2
EC	(500, 4000)	(200, 2500)	< 2	< 2
FB	(500, 7000)	(200, 3000)	<2	< 2
CM	(2500, 15000)	(1500, 6000)	< 0.5	< 2
MYE	(500, 15000)	(200, 6000)	< 0.5	< 2
Mural	(500, 5000)	(200, 2000)	< 2	< 2
LYM	(500, 15000)	(200, 6000)	< 0.5	< 2

Table 4. QC metrics used for the global object and each cell type

2.5 Downstream analyses of single-nucleus transcriptomics data

Data normalisation and scaling

Raw count numbers were normalised to 10,000 counts per nucleus and natural-log transformed using log1p. To reduce noise and computing complexity, 5,000 highly variable genes were identified and used for downstream analyses. Scaling was performed to give equal weighting to each gene, so that only the variation rather than absolute abundance of their expression will be considered in the downstream analyses. Mito% as a source of variation was regressed out.

Dimensionality reduction and batch correction

To reduce dimensionalities from 5,000 highly variable genes to a lower number, principal component analysis (PCA) was performed on scaled data, which identified 50 principal components (PCs), each explaining a proportion of total variance. Harmony 1.0 (Korsunsky et al. 2019) was applied to PCA result to correct for batch and sample variance. Elbow plot showing PC rankings based on the percentage of

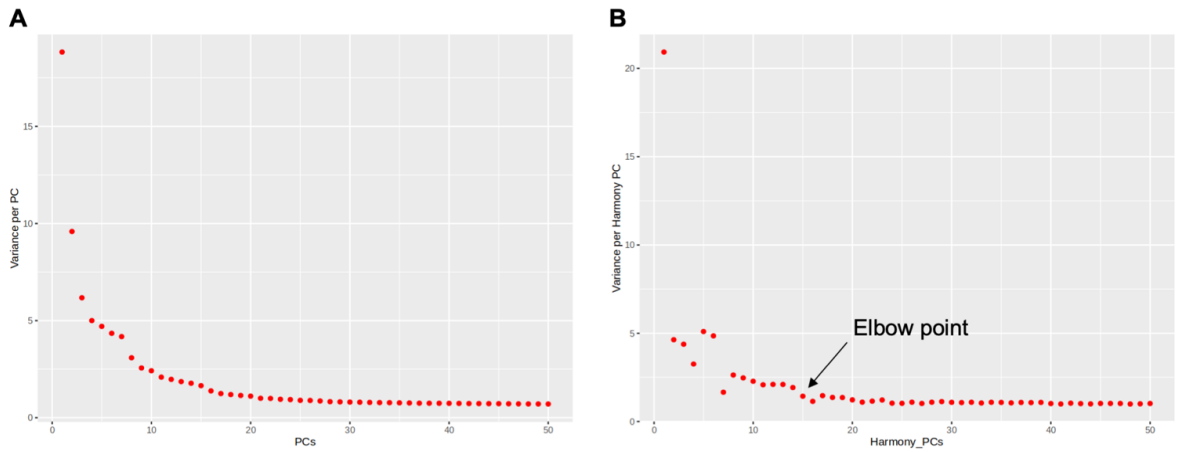

Figure D. Representative elbow plots showing raw and Harmony-corrected principal components A, Elbow plot showing the raw principal components (PCs) as ranked by the amount of variance each PC explains. **B**, Elbow plot showing the Harmony-corrected PCs in the same order of **A**, but with different amount of variance explained. Elbow point is indicated by an arrow. As both a non-linear dimensionality reduction and a data visualisation method, Uniform Manifold Approximation and Projection (UMAP) was calculated using selected number of Harmony-corrected PCs (Table 4). All nuclei were projected onto a 2D space and shown as scatters in UMAP.

variance explained by each PC was made for Harmony-corrected PC (Figure C). Number of Harmony corrected PCs used for downstream analyses was manually selected based on the elbow plot, where the elbow point suggests majority of variance explained (Table 4).

Leiden clustering and annotation

Nuclei clustering was performed in a graph-based fashion. Firstly, a nearest neighbours distance matrix was generated based on similar gene expression patterns between nuclei, using the same number of PCs as used for calculating UMAPs. Then, Leiden algorithm was called to group nuclei together based on the distance matrix. Clustering resolution was determined empirically according to the heterogeneity of the objects (Table 4).

To distinguish each cluster, marker genes were calculated either compared to all other clusters or against a subset of other clusters, statistically examined by Wilcoxon rank sum test. Genes with adjusted P value < 0.05 and $Log_2FC > 0.5$, and expressed in at least 25% nuclei in the group were considered marker genes.

Cell types were annotated at global level based on their specific expression of key marker genes. Then, each cell type (except for neuronal cells) were taken as an individual object (B cells and T cells were merged as lymphoid cells) and subclustered into cell states.

Cell states were typically annotated with the following information: 1) cell type abbreviation (e.g., MP for macrophages); 2) rank indicating the abundance of this cell state within this cell type (e.g., MP1 as the most abundant cell state in the macrophage population); 3) function (e.g., MP8_Proliferative) and/or expression level of key marker genes (e.g., MP6_Trem2Hi) of this cell state.

	Number of PCs used for Harmony	**Number of Harmony-corrected PCs used for clustering & UMAP**	**Clustering Resolution**
Global	30	30	0.07
EC	50	30	0.4
FB	50	25	0.7
CM	50	15	0.4

MYE	50	15	0.5
Mural	50	7	0.2
LYM	50	10	0.7

Table 5. Dimensionality reduction parameters used for the global object and each cell type

Data visualization

Annotated Seurat objects were converted to Scanpy AnnData objects using R package SeuratDisk 0.0.0.9019. Python package Scanpy 1.8.2 was used as the main platform for data visualisation, as well as for trajectory analysis and drug target prediction analysis (Wolf et al. 2018).

UMAPs were used to visualise: 1) integration of batches, samples or study groups; 2) cell type/state annotation; 3) localisation of specific genes and 4) other variables such as Milo neighbourhoods (described in 2.5.2) and trajectory (described in 2.5.4). Violin plots were employed to present the distribution of QC metrics or gene expression across various subsets (cell type/state, study group, sample…). Dot plots or matrix plots were used to show homogeneity/specificity and expression level of genes or pathways. Dendrograms where included indicate similarity between various subsets.

2.5.1 Differential gene expression analysis

To detect cell state-specific differentially expressed genes (DEGs) between study groups (VEH, DOX_3D and DOX_6W), counts of each sample for a specific cell state were summed (pseudo-bulk) and compared to the VEH group, using edgeR algorithm. In contrast to Wilcoxon rank sum test used for marker gene calculation, where each nucleus is considered statistically independent and sample

Raw counts	Gene A	Gene B	…
Nuc 1	a_1	b_1	…
Nuc 2	a_2	b_2	…
Nuc 3	a_3	b_3	…
Nuc 4	a_4	b_4	…
Nuc 5	a_5	b_5	…
Nuc 6	a_6	b_6	…
Nuc 7	a_7	b_7	…
Nuc 8	a_8	b_8	…
…	…		
Nuc m	a_m	b_m	…
Nuc n	a_n	b_n	…
Nuc p	a_p	b_p	…
Nuc q	a_q	b_q	…

+

Metadata	Sample	Group	Cell state
Nuc 1	VEH_1	VEH	X
Nuc 2	VEH_1	VEH	X
Nuc 3	VEH_1	VEH	Y
Nuc 4	VEH_2	VEH	X
Nuc 5	VEH_2	VEH	Y
Nuc 6	DOX_6W_1	DOX_6W	X
Nuc 7	DOX_6W_1	DOX_6W	Y
Nuc 8	DOX_6W_2	DOX_6W	X
…	…		
Nuc m	VEH_2	VEH	X
Nuc n	VEH_2	VEH	Y
Nuc p	DOX_6W_2	DOX_6W	X
Nuc q	DOX_6W_2	DOX_6W	Y

↘ ↙

Pseudo-bulk	VEH_1_X	VEH_1_Y	VEH_2_X	VEH_2_Y	DOX_6W_1_X	DOX_6W_1_Y	DOX_6W_2_X	DOX_6W_2_Y	…
Gene A	$a_1 + a_2 + …$	$a_3 + …$	$a_4 + … + a_m$	$a_5 + … + a_n$	$a_6 + …$	$a_7 + …$	$a_8 + … + a_p$	$… + a_q$	…
Gene B	$b_1 + b_2 + …$	$b_3 + …$	$b_4 + … + b_m$	$b_5 + … + b_n$	$b_6 + …$	$b_7 + …$	$b_8 + … + b_p$	$… + b_q$	…
…	…								

Figure E. Generating pseudo-bulk count matrices. Raw counts and metadata were retrieved from the original Seurat object. Then, counts of each gene from the same sample and cell state were summed to create a pseudo-bulk count matrix, with columns as sample-cell state pair, and rows as genes.

variation is obscured, pseudo-bulk edgeR takes each sample as a replicate (Junttila et al. 2022). This method aligns with the experimental design, allows batch correction, and applies false discovery rate (FDR) control to correct for multiple comparisons. Raw count matrices and metadata tables were first retrieved from Seurat objects. Then, pseudo-bulk count matrices were created by summing the gene counts of the same sample and cell state (Figure D). Next, edgeR was applied to perform counts normalization, and its built-in Quasi-Likelihood F-test (QLF) was used for differential expression analysis. Before using FDR to correct for multiple pairwise comparisons (e.g., gene A of cell state X in DOX_6W vs VEH), the following thresholds were applied: 1) for any sample to be considered valid, ≥ 3 nuclei of cell state X present in this sample; 2) for any group to be compared, ≥ 2 samples valid in this group; 3) gene A expressed in ≥ 2% of the nuclei in either the target group (DOX_6W) or the reference group (VEH); 4) gene A mean normalised expression ≥ 0.0125 in either the target group or the reference group. Only comparisons with the cell states and genes passed these thresholds were taken for FDR correction, so as to minimise redundancy and over-correction. FDR < 0.05 was considered statistically significant. Mitochondria-encoded genes were excluded from further analyses.

2.5.2 Differential abundance analysis

R package miloR 1.3.1 was used to test for differential population abundance between study groups (Dann et al. 2022). Briefly, each nucleus was assigned to partially overlapping neighbourhoods on a k-nearest neighbour (KNN) graph. Neighbourhoods were typically smaller than Leiden clusters, and were independently assigned, which allowed for detecting subtle population shifts that were masked by clusters.

Neighbourhood construction and differential abundance testing

Seurat objects of two groups (VEH + DOX_3D, and VEH + DOX_6W) were made and taken as inputs to Milo respectively, and each comparison set was converted to a Milo object. 30 Harmony-corrected PCs were used to build the KNN graph and define neighbourhoods. A key parameter *k* which affects the size of neighbourhoods was determined empirically based on the characteristics and size of the object, but was kept consistent between the two comparison sets of the same cell type (or global object). Then, each neighbourhood was tested for differential abundance (enriched in the target group or the reference group) using edgeR. FDR correction was performed based on the amount of overlap between neighbourhoods, and FDR < 0.1 was considered statistically significant.

Next, neighbourhoods were mapped to cell type/state assignment and annotated. Those with < 70% nuclei from the same cell type/state were annotated as “Mixed” and excluded.

Signature gene detection for neighbourhood subsets

Neighbourhoods were subset as desired based on significant enrichment and/or cell type/state annotation. Raw counts of the same sample and neighbourhood subset were summed, then normalised and tested for signature gene expression using edgeR. Genes with FDR < 0.05 and $Log_2FC > 0.5$ were considered signature genes for designated neighbourhood subsets. Mitochondria-encoded genes were excluded from further analyses.

Data visualization

Beeswarm plots were used to present neighbourhood distribution by cell type/state annotation and enrichment (Log_2FC). Milo data were mapped to UMAPs to show: 1) subsets of neighbourhoods; 2) neighbourhood size; 3) overlap between neighbourhoods and 4) enrichment of neighbourhoods.

2.5.3 Cell-cell interaction analysis

Cell-cell interaction analysis was performed and visualised using R package CellChat 2.1.2. Mouse CellChatDB was used as reference, which is a manually curated database of known ligand-receptor pairs, multimeric ligands and receptors. Co-factors including agonists, antagonists, co-stimulatory and co-inhibitory receptors were also taken into consideration in determining the strength of corresponding interactions (Jin et al. 2021).

Cell-cell interaction inference

Seurat objects of each study group (VEH, DOX_3D and DOX_6W) were made and taken as individual inputs to CellChat, and probability of each ligand-receptor pair was calculated per cell state. To highlight the stronger predictions, genes with expression in under 10% nuclei of a cell state were taken as zero expression ("truncatedMean" method). Population size was included as a weighting factor in the probability calculation, assuming abundant cell states produce collectively stronger signals. Interactions with less than 10 nuclei in a cell state were excluded. Then, ligand-receptor pair interactions were aggregated into signalling pathways by totalling either number or probability of interactions.

CellChat results of each group were merged and compared in the following aspects: 1) overall number and strength of interactions; 2) overall information flow of each pathway or ligand-receptor interaction; 3) differential number and strength of a specific pathway among different cell types/states; 4) differential ligand-receptor interaction among different cell types/states; 5) differential activity of each cell state as sender or receiver in a specific pathway.

Data visualization

Circle plots were made to visualise the up- or down-regulation of interaction strength between cell types and/or cell states. Chord plots were used to demonstrate the interactions of cell states in a signalling pathway.

2.5.4 Trajectory analysis

Trajectory analysis was performed and visualised using Python package scFates (Faure et al. 2023). Pre-processed and annotated Scanpy objects were used as input for scFates, and the Harmony-corrected PC was used as the dimensionality reduction embedding for curve fitting. Curve inference was performed on 10 nodes identified through an unbiased approach. Next, signature genes changing along the curve were calculated and clustered.

2.5.5 Drug target prediction analysis

Mouse genes were first transformed into human orthologs using the translate function of a python package mousipy v0.1.6. Next, python package Drug2cell (d2c) was used to predict the target cell type/state of DOX (Kanemaru et al. 2023), leveraging the ChEMBL database. A d2c score was calculated for each drug in the database targeting each cell type/state. Statistical significance was calculated using Wilcoxon rank sum test.

Gene ontology enrichment analysis

Gene ontology (GO) enrichment analysis was performed and visualised through an online interactive platform ShinyGO 0.80 (http://bioinformatics.sdstate.edu/go/). Briefly, a gene list of interest was imported to ShinyGO and mapped to the GO Biological Process database, and the enrichment P values for each pathway was derived using the hypergeometric test. Benjamini-Hochberg method was used to adjust the P value and control the false discovery rate (FDR). Pathways with FDR < 0.05 were considered significantly enriched. Fold enrichment of a pathway was defined as the ratio of the proportion of genes in the input list belonging to a pathway, to the corresponding proportion in the background (if given) or all genes. This metric was used to represent the magnitude of overrepresentation of a pathway in the input gene list.

2.5.6 Code and data availability

Shell scripts, R scripts and Jupyter notebooks used in this study have been uploaded to a GitHub repository (https://github.com/qinyue31/PhD_Thesis.git), currently accessible by request only and will be made publicly available at the end of the embargo period of this thesis. Raw sequencing data and processed objects will be uploaded to Gene Expression Omnibus (GEO) database.

2.6 Antibodies, cell lines, reagents

The anti-Gask1b antibody (PA5-52406) was purchased from Invitrogen and used for Western blotting and IF/IHC staining on mouse and human samples. A second anti-Gask1b (PA5-71113) antibody was used for Western blotting in zebrafish and purchased from Invitrogen. The anti-Thbs-1 (MA513398) and anti-Vimentin (MA5-11883) antibodies were purchased from Invitrogen. The anti-γH2A.X (07-627) and anti sarcomeric alpha-actinin (A7811) antibodies were purchased from Sigma. The anti-GAPDH (sc-3223) antibody was purchased from Santa Cruz Biotechnology. The anti-Mouse IgG (12-371), and anti-Rabbit IgG (12-370) antibodies were purchased from Sigma. The anti-Vinculin (4650) antibodies was purchased from Cell Signaling Technology.

The MOLM-13 and THP-1 cell lines were kindly provided as a gift by Isaia Barbieri (University of Torino, Italy) and cultured RPMI 1640 medium (11875093, Gibco, Invitrogen) supplemented with 10% FBS.

The adenoviral vectors human type 5 GFP-m-*Gask1b*-shRNA (*shGask1b-Ad*) or GFP-scrambled (shScrambled-Ad) and adeno-associated viral vectors serotype 9 GFP-m-Gask1b-shRNA (shGask1b-AAV9) or GFP-scrambled (hScambled-AAV9) were purchased from Vector Biolab (Malvern PA, USA).

2.7 Zebrafish treatment

Tuebingen wild-type and cmlc2:GFP zebrafish were utilized for this study. Adult zebrafish were kept under standard conditions with a 14-hour light and 10-hour dark cycle at approximately 28°C. Breeding and genotyping were performed following established protocols, ensuring allelic transmission in accordance with Mendelian ratios. Eggs were produced through natural mating, collected post-fertilization, and subsequently maintained under a 12-hour light and 12-hour dark cycle, with incubation at 28°C. Zebrafish larvae were euthanized using an overdose of tricaine. All zebrafish and mouse experiments were approved by the Ethical Committee of the University of Torino and the Italian Ministry of Health.

2.7.1 Morpholino microinjection

Antisense Morpholino Oligonucleotides against gask1b and scrambled control were purchased from GeneTools (LLC, Philomat, OR, USA). The gask1b-morpholino sequence was 5′ CTCCAAGATGATCCGCTCAGCGCAG -3′. The scrambled control-morpholino sequence was 5′-CCTCTTACCT- CAGTTACAATTTATA -3′ Tuebingen and cmlc2:GFP zygotes were e collected at 1-cell stage and injected under stereological examination with 400 mM of Gask1b-morpholino or scrambled control- morpholino in the presence of Phenol Red for subsequent selection of the injected embryos.

2.7.2 Zebrafish heart fractional shortening measurement

Zebrafish at 1-day post-fertilization (dpf) were treated with DMSO or doxorubicin (DOX) for 2 days. High-speed video microscopy was employed to assess ventricular size and function, following previously described protocols (Shin et al., 2010). Videos were acquired with a Leica Sp5 confocal microscope. Briefly, M-mode images were constructed from sequential frames along a fixed scan line using ImageJ software. Ventricular dimensions were measured at the endocardial borders during end systole and end diastole, and fractional shortening was then calculated from these measurements.

2.7.3 Protein extraction and western blotting of whole zebrafish larvae

Whole zebrafish larvae were lysed on ice for 15 minutes with the help of a pestle and using a lysis buffer containing 120 mM NaCl, 50 mM Tris-HCl (pH 8.0), 1% Triton X-100, protease inhibitor Complete (Roche Applied Science, Penzberg, Germany), and phosphatase inhibitors (50 mM sodium fluoride, 1 mM sodium orthovanadate, and 10 mM sodium pyrophosphate). The lysates were then clarified by centrifugation at 13000 rpm for 15 minutes at 4°C. Protein concentrations were measured using the Bradford method. Proteins from heart tissues or cell lysates were resolved by SDS-polyacrylamide gel

electrophoresis (SDS-PAGE) and subsequently transferred to methanol-activated polyvinylidene difluoride (PVDF) membranes (Millipore Corporation, Billerica, Massachusetts). The membranes were blocked for 1 hour with 5% bovine serum albumin (BSA)-TBST [tris-buffered saline (TBS) with 0.3% Tween 20] at room temperature, followed by an overnight incubation with primary antibodies at 4°C. Appropriate horseradish peroxidase-conjugated secondary antibodies specific to the host species were then added, and the signals were detected using enhanced chemiluminescence (Millipore Corporation, Billerica, Massachusetts). The primary antibodies utilized in this study are listed in the corresponding table.

2.8 Primary neonatal cardiomyocyte isolation

Neonatal ventricular mouse cardiomyocytes (NMCM) were isolated from one to two-day old C57BL/6 pups according to the protocol provided by the manufacturer (Miltenyi Biotech). The pups were sacrificed by decapitation and hearts were harvested using sterilized scissors and forceps. Hearts were washed and transferred into a gentleMACS C tube containing 2.5 mL enzyme mix before being incubated at 37oC for 15 min. Tissues were subjected to a mechanical dissociation process using a gentleMACS dissociator (Miltenyi Biotech). The step of enzymatic digestion and tissue dissociation was repeated three times. After that, samples were filtered through a 70 µm gauge mesh filter inserts to remove large particles. The filtrate was centrifuged at 600 g for 5 min, and the supernatant was removed. The pellet was resuspended and cultured in a flask for one hour at 37 ◦C to allow for the separation between cardiac fibroblasts and cardiomyocytes (pre-plating). After one hour, the medium enriched with cardiomyocytes was collected and plated onto dishes previously coated with fibronectin (10 µg/mL) and gelatin (0.2%).

2.9 γH2A.X staining in primary neonatal ventricular cardiomyocytes

After extraction, NMVCs were seeded in IBIDI® µ-Slide 8 Well previously coated with with fibronectin (10 µg/mL) and gelatin (0.2%) and kept for 24 hours to allow full seeding and stabilization. After 24 hours cells were infected with either shScrambled-GFP-ADV5 or shGask1b-GFP-ADV5 and kept for 48 hours in infection medium to allow efficient *Gask1b* gene silencing. Following infection, cells were exposed to either vehicle (PBS) or DOX at 1 µM concentration for 24 hours. At the end of the treatment, NMCMs were fixed in formaldehyde 4% for 15 minutes and washed 3 times in 1X PBS, prior to be blocked and incubate with primary antibody against γH2A.X (Ser 139) 1:100 (Sigma-Aldrich, #JBW301), in 0.5% triton x-100, 1% BSA in PBS in a humidified chamber overnight at 4°C. Next day, samples were incubated with the corresponding secondary antibodies (Alexa-647) for 30 min at RT and washed again 3 times with 1X PBS prior to be counter-stained with DAPI 1:1000 for 5 minutes (Thermofisher Scientific). Pictures were acquired with a Leica TCS SP8 confocal microscope (TCS SP8 Leica, Leica Microsystems GmbH, Wetzlar, Germany) and cells positive both to GFP (infected) and γH2A.X (>10 foci per nucleus) were counted with ImageJ software (https://imagej.nih.gov/ij/).

2.10 Western blotting

Whole hearts were lysed on ice for 15 minutes using a lysis buffer containing 120 mM NaCl, 50 mM Tris-HCl (pH 8.0), 1% Triton X-100, protease inhibitor Complete (Roche Applied Science, Penzberg, Germany), and phosphatase inhibitors (50 mM sodium fluoride, 1 mM sodium orthovanadate, and 10 mM sodium pyrophosphate). The lysates were then clarified by centrifugation at 13000 rpm for 15 minutes at 4°C. Protein concentrations were measured using the Bradford method. Proteins from heart tissues or cell lysates were resolved by SDS-polyacrylamide gel electrophoresis (SDS-PAGE) and subsequently transferred to methanol-activated polyvinylidene difluoride (PVDF) membranes (Millipore Corporation, Billerica, Massachusetts). The membranes were blocked for 1 hour with 5% bovine serum albumin (BSA)-TBST [tris-buffered saline (TBS) with 0.3% Tween 20] at room temperature, followed by an overnight incubation with primary antibodies at 4°C. Appropriate horseradish peroxidase-conjugated secondary antibodies specific to the host species were then added, and the signals were detected using enhanced chemiluminescence (Millipore Corporation, Billerica, Massachusetts). The primary antibodies utilized in this study are listed in the corresponding table.

2.11 Immunofluorescence staining and crossectional area measurement of mouse tissue

Mouse hearts were fixed for overnight in 4à paraformaldeyde prior to be de-hydrated through application of sucrose gradient and embedded in OCT. Mouse heart sections (6 µm) were obtained using a cryostat and stored at -80°C. Slides were equilibrated to room temperature, encircled with a PAP pen, and rehydrated with PBS 1× for 10 minutes. Sections were incubated overnight at 4°C with primary antibodies (e.g., Anti-Gask1b; alpha-actinin) diluted in PBS 1× + BSA 1% + Triton X-100 0.5%. After PBS washes, secondary antibodies (Alexa Fluor 488, 568, or 643) were applied for 30 minutes at 37°C. Nuclei were counterstained with DAPI (5 min) or Sytox Far Red (1/4000, 40 min). Slides were washed and mounted with Prolong mounting medium, dried overnight, and stored at 4°C. For mouse-on-mouse staining (MOM: VectorLabs, Newark, California, USA) blocking was performed before primary antibody incubation. For crossectional area measuremement, mouse hearts were fixed and de-hydrated as described above. Wheat Germ Agglutinin (WGA) conjugated with Alexa Fluor 488 were used according to manufacturer's instructions. Cardiomyocyte area was measured with ImageJ software as previously described (Li, 2018 #71).

2.12 Human samples

Human heart samples were collected from a 21-year-old woman diagnosed with Ewing sarcoma and subjected to triple therapy with adriamycin, cyclophosphamide, and vincristine. The patient manifested heart failure symptoms 5 years after chemotherapy and underwent heart transplantation 10 years after the diagnosis of chemotherapy-induced cardiomyopathy (ejection fraction: 40%). Samples were archived at the Institute of Pathological Anatomy of the University of Padova. Samples were anonymous to the investigators and used in accordance with the directives of authorities. Formalin-fixed, paraffin-embedded human heart samples were processed for immunohistochemistry (IHC). IHC was performed on tissue sections following antigen retrieval in citrate buffer (pH 6) using a pressure cooker. Endogenous peroxidase activity was blocked with 0.3% H_2O_2 for 10 minutes at room temperature (RT).

Sections were then blocked with TBS-Triton (0.1%), 5% BSA, and 1% goat serum for 30 minutes in a humidified chamber. Primary antibodies anti-Gask1b (PA5-52406) 1:100 was applied overnight at 4°C. After washing, biotinylated secondary antibodies were incubated for 30–45 minutes at RT, followed by ABC complex if required. DAB substrate was used for signal detection, with reaction time monitored microscopically. Counterstaining was performed with hematoxylin. Sections were dehydrated through graded alcohols and xylene. Coverslips were mounted with resin. All washes were performed with TBS-Tween.

2.13 Statistics

Data were visualised and analysed using GraphPad Prism 10. Each experiment was performed using at least three independently differentiated batches of cells (N = 3) unless otherwise specified. Data were first examined for normality using either Shapiro-Wilk test or Kolmogorov-Smirnov test. Data following normal distribution were shown as mean ± standard error of the mean (SEM) and analysed with the following tests: 1) To compare data from two groups, F test was used to examine homoscedasticity before running Student's t test. For data with significantly different variances, Welch's t test was used. 2) To compare data from multiple groups with single factor, Brown-Forsythe test was performed to examine homoscedasticity. One-way ANOVA was used to detect the overall difference among all groups, followed by Tukey's multiple comparisons test for *post hoc* pairwise comparisons. For data not meeting equal variance, Brown-Forsythe or Welch's ANOVA was used to detect the overall difference, followed by Dunnett's T3 multiple comparisons test for *post hoc* pairwise comparisons.

For data that did not pass normality test, either log-transformation was performed before re-examining for normality and equal variance, or nonparametric tests were undertaken to determine statistical difference: Mann-Whitney rank test was used for comparing two groups, and Kruskal-Wallis rank test was used for comparing multiple groups with single factor, followed by Dunn's multiple comparisons test for *post hoc* pairwise comparisons. Data analysed with nonparametric tests were presented in Tukey's box plot format including median, interquartile range (IQR), 1.5 × IQR and outliers.

3. RESULTS

3.1 Generation of a murine nucleus-gene expression heart atlas of Doxorubicin-induced cardiotoxicity

Here, we employed our previously established murine model of DOX-induced cardiotoxicity (Li et al., 2018) to investigate both early and late stages of the disease. To this end, we designed two treatment protocols: a 3-day regimen (DOX_3D) to mimic early cardiotoxicity and a 6-week regimen (DOX_6W) to reflect later-stage toxicity (Figure 1A). Using single-nucleus transcriptomic profiling (Figure 1B), we analysed heart tissues from vehicle control (VEH) and DOX-treated mice (DOX_3D and DOX_6W) to uncover DOX-induced changes in the cellular landscape and molecular signatures of the heart. Unbiased clustering of data from 12 mouse hearts (52,926 nuclei) allowed to define 8 major cell types, including endothelial cells (EC), fibroblasts (FB), ventricular cardiomyocytes (CM), myeloid cells (MYE), mural cells, including pericytes (PC) and smooth muscle cells (SMC), T cells (TC), B cells (BC) and neuronal cells (NC) (Figure 1C). The annotation was based on a panel of well recognised marker genes as shown in Figure 1D (Litvinukova et al., 2020, Skelly et al., 2018, Wolfien et al., 2020). Interestingly, although *Pecam1* is commonly used as an endothelial lineage marker and its expression in lymphoid cells (B cells and T cells) might seem unexpected (Figure 1D), the encoded protein CD31 has been found to play a key role in regulating lymphoid homeostasis (Wilkinson et al., 2002, Marelli-Berg et al., 2013). Unbiased subclustering of each cell type allowed the identification of 42 different cell states (Figure 2), whose role, at least for major cell types, will be introduced and elaborated in the following paragraphs.

Firstly, we moved to explore how DOX changed the cellular landscape of the heart. Previous works studying DOX tumour killing and cardiotoxicity mechanisms have identified many of its molecular targets. To infer the effect of DOX on cardiac cells based on the known targets, we transformed the mouse genes to human genes and utilised drug2cell (Figure 3A), which comprehensively examines drug-target interactions leveraging the ChEMBL database (Kanemaru et al., 2023) (Figure 3A). Drug2cell identified FB, CM and MYE to be the 3 major cell types targeted by DOX, based on their high expression of known DOX targets (Figure 3B). To uncover nuanced abundance perturbation that are potentially obscured by Leiden clustering, we applied milo, a sophisticated differential abundance analysis that clusters nuclei into neighbourhoods, and compares the abundance of each neighbourhood between groups (Dann et al., 2022) (Figure 3C). Milo showed that although DOX did not induce major population shifts at 3-day (Figure 3D), there was significant enrichment of FB and MYE neighbourhood subsets at 6-week (Figure 3E). DOX also perturbed the CM populations, as shown by both enrichment and depletion of neighbourhood subsets in DOX_6W group (Figure 3E). Notably, the three cell types (FB, CM, and MYE) with significant population shifts at DOX_6W overlapped with those identified by drug2cell, suggesting important roles in DOX cardiotoxicity. We then conducted detailed analyses of these cell types, while also considering the potential involvement of vascular (EC and mural) and lymphoid (TC and BC) populations. However, EC and mural cells were not included in our in-depth analysis at this stage.

3.2 Doxorubicin activates cardiac fibroblasts which play central role in pathogenic extracellular matrix remodelling

3.2.1 Doxorubicin induces expansion of an activated fibroblast subpopulation at 6-week

Mouse cardiac fibroblasts were defined by enriched expression of *Dcn* (encoding decorin), *Gsn* (gelsolin) and *Pdgfra* (platelet-derived growth factor receptor A) (Figure 4A-B). We then further identified 8 FB cell states and annotated them based on established single-cell mouse heart studies (Farbehi et al., 2019, Forte et al., 2020, McLellan et al., 2020) and cross-examined these populations with other published datasets (Hesse et al., 2021, Li et al., 2023b) (Figure 4A-B; Table 6). Despite differences in mouse strains (Forte et al., 2020), disease models and even techniques (single-cell vs single-nucleus), most reported fibroblast populations were recapitulated in our dataset (Table 6), suggesting conserved murine cardiac FB populations. Among the 8 FB cell states we identified, FB1 did not express exclusive markers, and we proposed such population to represent a basic and unspecific state of the lineage. FB2_Sca1Lo, FB4_Sca1Hi, FB5_Transitory and FB7_WntX were the 4 populations that consist of the majority of FBs in healthy mouse hearts (Patrick et al., 2024). FB6_Interferon and FB8_IR (injury response) were both related to inflammatory responses. FB3_Activated was the key state responsible for extracellular matrix (ECM) remodelling, which was found with moderate abundance in healthy hearts and expanded after MI (Patrick et al., 2024). The two large resting populations FB2_Sca1Lo and FB4_Sca1Hi were distinguished by different expression level of stem cell antigen 1 (Sca1), encoded by *Ly6a* (Patrick et al., 2024) (Figure 4B). FB4_Sca1Hi was found to correlate to a $Sca1^{+}PDGFR\alpha^{+}$ population in the murine myocardium defined by flow cytometry (Farbehi et al., 2019), which showed self-renewal and differentiation properties (Noseda et al., 2015). This population *in vivo* was speculated to be a reserve for expansion and specialisation in homeostasis and after injury (Miranda et al., 2023). FB4_Sca1Hi also featured enriched expression of *Pi16* (encoding peptidase inhibitor 16) (Regn et al., 2016) and *Cd248* (endosialin) (Smith et al., 2015) (Figure 4B). The other major resting population FB2_Sca1Lo showed lower *Sca1* expression, and was marked by *Lpl* (lipoprotein lipase), *Hsd11b1* (hydroxysteroid 11-beta dehydrogenase 1) and *G0s2* (G0/G1 switch gene 2) (Figure 4B). A distinct population FB7_WntX exclusively expressed *Wif1* and *Dkk3*, both encoding secreted Wnt antagonists (Farbehi et al., 2019) (Figure 4B). The non-canonical WNT pathway is known to activate TGFb signaling in cardiac fibroblasts and promote fibrosis (Akoumianakis et al., 2022), while *Wif1* inhibits Wnt pathway and the pro-fibrotic connective tissue growth factor (CTGF) pathway (Surmann-Schmitt et al., 2012). Therefore, the anti-WNT, anti-TGFb and anti-CTGF population FB7_WntX was considered an activated but anti-fibrotic state (Farbehi et al., 2019). A genetic tracing study revealed FB7_WntX as endocardial-derived, which made it a distinct population compared to other epicardial-derived fibroblasts (Forte et al., 2020). FB5_Transitory was marked by *Igfbp3* (insulin like growth factor binding protein 3), *Fgl2* (fibrinogen like 2) and *Inmt* (indolethylamine N-methyltransferase) (Figure 4B), which was considered a transitory state between FB2_Sca1Lo and FB7_WntX (Farbehi et al., 2019). FB6_Interferon was characterised by interferon-responsive genes including *Iigp1*, *Ifit1* and *Ifit3* (Figure 4B). FB8_IR enriched for *Ccl2* and *Ccl7*, encoding key monocyte/macrophage chemoattractant, and *Cxcl5*, a

neutrophil activator (Figure 4B). This chemokine-expressing population expanded massively 1 day after MI in murine hearts, and their role was defined as injury response (IR) (Forte et al., 2020). FB3_Activated highly expressed *Postn*, encoding a fibrogenic extracellular matrix (ECM) protein periostin, *Meox1* whose encoded transcription factor is key to cardiac fibroblast activation (Tani et al., 2023, Alexanian et al., 2021), and *Cilp* (cartilage intermediate layer protein 1) which promotes myocardial fibrosis (Zhang et al., 2021) (Figure 4B). Collectively, FB3_activated is responsible for ECM protein secretion and potential fibrosis development. We also examined whether two other specialised FB populations: myofibroblasts (MYO) and matrifibrocytes (MFC) were present. MYOs actively participate in tissue remodelling by producing ECM, and are characterised by a contractile phenotype. MYO from the FB lineage are defined by co-expression of contractile gene *Acta2* (actin alpha 2, or α-SMA) and FB markers such as *Pdgfra* (Younesi et al., 2021). Another MYO marker is *Cthrc1* (collagen triple helix repeat containing 1), which is a key regulator of ECM deposition and scar healing process (Ruiz-Villalba et al., 2020). In the DOX-induced cardiotoxicity single-nucleus transcriptome, *Acta2* was absent in the FB population, and *Cthrc1* was only expressed in a minor proportion of FB3_Activated (Figure 4B), which was not sufficient to be defined as a standalone cell state. MFCs are involved in the resolution phase of tissue remodelling, which express less contractile genes or Wnt-inhibiting genes, but feature chondrogenic or osteogenic ECM genes such as *Comp* (cartilage oligomeric matrix protein) and *Sfrp2* (secreted Frizzled related protein 2) (Forte et al., 2020). Similarly, although *Comp* and *Sfrp2* were lowly detected in FB7_WntX, FB3_Activated or FB5_Transitory (Figure 4B), their different localisation suggested absence of an independent MFC cell state.

To explore whether DOX induced any FB population shifts at either 3-day or 6-week, we compared the two DOX-treated conditions with the VEH group respectively. No significant differential abundance was detected in DOX_3D vs VEH (Figure 4C), while there was a subset of FB3_Activated neighbourhoods highly enriched in the DOX_6W group (Figure 4D), suggesting an expansion of at least a subset of this population upon DOX treatment at 6-week.

Cell state	Marker genes	Farbehi 2019	Forte 2020	McLellan 2020	Hesse 2021	Li 2023
FB1	/	F-SL?	Homeostatic epicardial derived fibroblasts (HEpiDs)?	/	/	Fibro 0?

FB2_Sca1Lo	*Lpl* *Hsd11b1* *G0s2*	F-SL	Homeostatic epicardial derived fibroblasts (HEpiDs)	/	aCSC-5?	Fibro 1
FB3_Activated	*Postn* *Meox1* *Cilp*	F-Act	Late-resolution (LR) fibroblasts	Fibroblast-*Cilp*	aCSC-2	Fibro 5
FB4_Sca1Hi	*Ly6a* *Pi16* *Cd248*	F-SH	Progenitor-like state fibroblasts (PLSs)	Fibroblast 6	aCSC-4 aCSC-9	Fibro 2
FB5_Transitory	*Igfbp3* *Fgl2* *Inmt*	F-Trans	Homeostatic epicardial derived fibroblasts (HEpiDs)	Fibroblast 2	aCSC-1? aCSC-5	Fibro 4 Fibro 6
FB6_Interferon	*Iigp1* *Ifit1* *Ifit3*	F-IFNS	Interferon-response (IFNr)	Fibroblast 9	aCSC-8	Fibro 9
FB7_WntX	*Dkk3* *Wif1* *Scara3*	F-WntX	Endocardial derived (EndD)	Fibroblast-*Wif1*	aCSC-11	Fibro 8
FB8_IR	*Ccl2* *Ccl7* *Cxcl5*	/	Injury response (IR)	Fibroblast 4?	/	/
Not found	*Acta2* *Cthrc1*	MYO	Myofibroblasts (Myofb)	Not found	aCSC-3	/

Not found	*Comp* *Sfrp2*	/	Matrifibrocytes (MFCs)	Fibroblast-*Thbs4*	/	/

Table 6. Cross-examination of fibroblast cell states with published datasets

3.2.2 Activated fibroblasts as a key player in Doxorubicin-induced extracellular matrix remodelling

To examine whether the expanded FB3_Activated population in DOX_6W group developed specialised features compared to FB3 observed under basal condition (VEH), we first mapped the Milo neighbourhoods on UMAP by either the magnitude of enrichment (Log_2FC) (Figure 5A) or neighbourhood groups (Figure 5B). Indeed, the DOX_6W-enriched FB3 neighbourhoods showed the highest Log_2FC, and were localised on the top tip of FB3, suggesting a relatively distinct population (Figure 5A-B). Then, we calculated the signature genes of FB3 neighbourhoods enriched in DOX_6W, compared to other FB3 neighbourhoods. The up-regulated signature genes featured an expression gradient: highest in DOX_6W enriched FB3 neighbourhoods, moderate in other FB3 neighbourhoods, and lowest in all other FB neighbourhoods (Figure 5C), highlighting a well distinct transcriptional profile in these enriched FB3 neighbourhoods.

Focusing on FB3_Activated up-regulated genes in the DOX_6W, *Postn* and *Meox1* were the defining markers of FB3_Activated, indicating a further activation of fibroblasts upon DOX treatment at 6-week. Interestingly, although *Acta2*, the key marker of myofibroblasts, was negligibly expressed in FB nuclei and showed no specificity in any FB cell state (Figure 4B), *Cthrc1* (encoding collagen triple helix repeat containing 1) and *Fn1* (fibronectin 1) were significantly up-regulated in DOX_6W group within FB3 population (Figure 5D). These two genes were identified as important signatures of a profibrotic myofibroblast population in the MI model (Patrick et al., 2024, Farbehi et al., 2019). Additionally, *Tagln* (or Sm22α, encoding actin-binding protein transgelin) which was typically considered a smooth muscle cell marker was up-regulated in this population (Figure 5D). Transgelin is inducible by the key tissue-remodelling transforming growth factor beta (TGFb) (Elsafadi et al., 2016, Aldeiri et al., 2017), and its overexpression in cancer-associated fibroblasts was found to activate the NF-kB pathway, and increase the release of pro-inflammatory interleukin 6 (Sun et al., 2023). Although less established than *Acta2*, *Tagln* was also considered a myofibroblast marker (Aldeiri et al., 2017). Another up-regulated gene *Actn1* encodes α-actinin (Figure 5D), which is not a contractile protein itself, but is key to the formation of large actin stress fibres that are contractile actin bundles found in non-muscle cells (Pellegrin and Mellor, 2007). Myofibroblasts also feature robust actin stress fibres (Sandbo and Dulin, 2011). Thus, we speculated that activated fibroblasts developed myofibroblast-like features upon DOX treatment at 6-week, including *Cthrc1*, *Fn1*, *Tagln* and *Actn1*.

We then explored the expression pattern of genes encoding ECM proteins in this specialised population. DOX treatment up-regulated specific collagen-encoding genes at 6-week, including *Col5a2*, *Col8a1*, *Col12a1* and *Col22a1* (Figure 5D). Their roles in regulating cardiac fibrosis were poorly defined, but

have been indicated to involve in the pathogenesis of pulmonary, vascular or dermal fibrosis (Li et al., 2024, Jin et al., 2024, Zhao et al., 2023, Watanabe et al., 2019).

Another family of genes encoding connective tissue growth factors including *Ccn1*, *Ccn2* and *Ccn4* were also enriched in the DOX_6W group of FB3 (Figure 5D). Elevated plasma level of connective tissue growth factor was found as a biomarker of cardiac dysfunction in patients with chronic heart failure (Koitabashi et al., 2008). A recent finding showed that *Ccn2* deletion ameliorated DOX-induced cardiac dysfunction and fibrosis in mice, suggesting its therapeutic potential (Tejera-Munoz et al., 2024). Moreover, *Tnc* was up-regulated in the DOX_6W group in FB3_Activated (Figure 5D), and the encoded protein tenascin-C is indeed responsible for driving continuous fibroblast activation and progression of fibrosis in multiple organs, including the heart (Bhattacharyya et al., 2022).

Lastly, *Thbs1* and *Thbs4, encoding* thrombospondin-1 and -4, were significantly up-regulated (Figure 5D). Thrombospondin-1 (TSP1) was indicated as a transforming growth factor B (TGFB) activator, and blocking TSP1 prevented the progression of cardiac fibrosis in a rat diabetic cardiomyopathy model (Belmadani et al., 2007). Interestingly, in mouse hearts administered with angiotensin II, a fibroblast population enriching for *Thbs4* emerged and promoted fibrosis in the absence of myofibroblasts (McLellan et al., 2020). Together, the two genes of the thrombospondin family may play an important role in driving cardiac fibrosis. Additionally, Thbs-1 was found to be significantly upregulated also at protein level in the DOX_6W group, corroborating our transcriptomic finding and underscoring its potential as a biomarker in DIC (Figure 5E).

To summarise, we discovered a subpopulation of FB3_Activated enriched in the DOX_6W group, which increasingly expressed canonical activated fibroblast markers and myofibroblast-like features, and showed specific patterns of matricellular protein gene expression. Moreover, we found Thrombospondin-1 as a potential biomarker of DIC and feature of FB3_Activated. Together, these findings suggested a potential role of FB3 in extracellular matrix remodelling at 6-week post DOX treatment.

3.2.3 Activated fibroblasts are predicted to mainly interact with cardiomyocytes and myeloid cells

To further unravel and validate the function of FB3_Activated in DOX-induced ECM remodelling, we utilized CellChat, a powerful tool to dissect cell-cell interactions (Jin et al., 2023, Jin et al., 2021). Briefly, CellChat systematically examined the role of each cell state as sender or receiver based on their abundance and their expression of known ligands or receptors, leveraging the mouse CellChatDB of ligand-receptor pairs. Then, the signalling strength of each ligand-receptor pair from individual sender-receiver pair was calculated. The role of a cell state/type as sender or receiver was determined by aggregating its outgoing or ingoing signalling. Signalling from various isoforms of ligands/receptors, or those serve similar or related biological function were aggregated as pathways (Figure 6A).

We observed three major ECM-receptor pathways: periostin (PERIOSTIN), fibronectin 1 (FN1) and thrombospondin (THBS) that featured FB3_Activated as the top sender in DOX_6W group (Figure 6B-

D). We then examined the CellChat-predicted cell-cell interactions of these three pathways. For PERIOSTIN pathway, myeloid cells (MYE) and fibroblasts (FB) were predicted to be the most targeted cell types (Figure 6B). Indeed, cardiac fibroblasts and macrophages were found as two main populations driving cardiac fibrosis and remodelling, at least partially regulated by periostin signalling (Frieler and Mortensen, 2015). Ablation of *Postn*-expressing cells in mouse heart decreased FB activation and fibrosis following MI (Kaur et al., 2016). Periostin was also found to stimulate the expression of matrix metalloproteinases (MMPs) in cardiac valve macrophages (Hakuno et al., 2010), suggesting a tissue remodelling role of this axis in macrophages.

For FN1 pathway, MYE was also the top predicted target cell type (Figure 6C). Fibronectin within the cardiac matrix was reported to induce the monocyte-to-macrophage conversion and their subsequent secretion of vascular endothelial growth factor (VEGF) and interleukin-6 (IL6). Those macrophages were also able to recruit mesenchymal stromal cells with anti-inflammatory and pro-angiogenic features, contributing to post-MI repairing machineries (Roy et al., 2020).

Endothelial cells (EC) and cardiomyocytes (CM) were the two cell types predicted to be the main targets of THBS pathway (Figure 6D), which has been identified with multiple roles in the heart (Kale et al., 2021). Thrombospondin 1 was found to induce EC senescence (Gao et al., 2016) and inhibit ECs' response to nitric oxide (NO), compromising the vasodilation function (Rogers et al., 2017). Thrombospondin 1 also induced autophagy in CMs, resulting in lethal cardiac atrophy (Vanhoutte et al., 2021). Notably, cardiomyocyte and cardiac atrophy is an iconic hallmark of DOX-induced cardiotoxicity (Willis et al., 2019, Chen et al., 2022a).

Collectively, we used CellChat to examine ECM-receptor signalling and revealed the key role of FB3_Activated in PERIOSTIN, FN1 and THBS pathways, particularly at 6-week post DOX treatment. Signals sent from activated fibroblasts were predicted to interfere with various cardiac cell types, particularly MYE cells, potentially driving pathogenic tissue remodelling and dysregulating normal cardiac cell function. This led us investigating on the role of immune cells in DOX-induced cardiac remodelling, with major focus on MYE cells.

3.3 Doxorubicin triggers complex immune response in the heart

3.3.1 Doxorubicin increases Trem2^{Hi} macrophage and type-2 conventional dendritic cell populations

We identified three main lineages of myeloid cells: macrophages (MP), dendritic cells (DC) and neutrophils (NEUT) (Figure 7A). MPs were defined by well-established lineage markers, including *Lyz2* (encoding lysozyme 2 which enables MP lysozyme activity), *Adgre1* (encoding the F4/80 antigen) and *C1qa* (encoding a complement component) (Figure 7B). Within the MP lineage, we further identified 8 unique MP cell states, suggesting a highly heterogenous population (Figure 7A).

Below, we provide a detailed annotation of the various MP and DC subpopulations.

MP1 did not present specific marker genes that differentiated itself to the rest of the MP population. Therefore, we did not assign a label inferring the function of this cell state, but rather took it as an unspecific and basic population of the macrophage lineage.

To annotate the other MP cell states, we first examined a set of established genes to distinguish a classic dichotomy of cardiac MPs: tissue-resident or monocyte-derived. Classic tissue-resident macrophages (TRMs) are derived from embryonic origins (yolk sac or foetal liver monocytes) (Epelman et al., 2014b), which were characterised by high expression of *Timd4* (T cell immunoglobulin and mucin domain containing 4), *Lyve1* (lymphatic vessel endothelial hyaluronan receptor 1) and *Folr2* (folate receptor 2) (Shaw et al., 2018, Cahill et al., 2021, Nalio Ramos et al., 2022). TRMs expressing either of these three genes were defined as TLF$^+$ cells (Dick et al., 2022), and were found to have self-renewal capacity and require minimum monocyte input (Dick et al., 2019). These TLF$^+$ TRMs were found to prevent fibrosis and stimulate angiogenesis upon cardiac pressure overload (Revelo et al., 2021), suggesting their homeostatic and reparative roles in the heart. In contrast, *Ccr2* (encoding C-C motif chemokine receptor 2) expression in the MP lineage typically suggests monocyte-derived macrophages (MDMs), given the function of this gene related to monocyte recruitment. Although some pointed out that *Ccr2*$^+$ MPs could also reside in the tissue (Epelman et al., 2014a) and demonstrated a pro-inflammatory phenotype (Bajpai et al., 2019), these cells still feature an adult monocytic origin. To better identify the recruited MDMs, we also examined the expression of major histocompatibility complex class II (MHC-II) molecules including *H2-Aa*, and *Cd74* whose encoded protein enables MHC-II protein binding activity. High expression of both *Ccr2* and MHC-II corresponds to a previously-identified classic MDM population, demonstrating chemotaxis and antigen presentation ability (Dick et al., 2019).

Using a combination of these 6 markers expressed at varying levels, we annotated MP2 and MP3 as TRMs. MP2 was characterised by highest level of *Timd4*, *Lyve1* and *Folr2*, as well as absence of *Ccr2* (Figure 7B), which defined it a classic TLF$^+$ TRM population (MP2_TLF+_Ccr2-). Similar features were found in MP3, but this cell state also specifically expressed *Igf1* and *Igfbp4* (Figure 7B), encoding an insulin-like growth factor and its binding protein. The IGF1 protein was found cardio-protective after myocardial infarction, through inducing an anti-inflammatory phenotype of cardiac macrophages (Heinen et al., 2019), as well as attenuating the pro-inflammatory phenotype of neutrophils (Nederlof et al., 2022). *Igf1*$^+$*Igfbp4*$^+$ cardiac macrophages were also protective against cardiac dysfunction in a mouse model of hypertension-induced cardiac stress (Zaman et al., 2021). MP3 also highly expressed *Tlr7* (encoding Toll-like receptor 7) (Figure 7B), which has been associated with an anti-inflammatory M2 macrophage phenotype (Karadimou et al., 2020). Based on these unique features, we speculated MP3_Igf1Hi_Ccr2- to play an anti-inflammatory and reparative role in the heart.

Conversely, MP4 and MP5 expressed negligible TLF but high *Ccr2* and MHC-II (Figure 7B), which suggested their origins likely monocyte-derived. When comparing MP4 and MP5 alone, MP4 showed more specific features including higher expression of *Cx3cr1* (encoding the receptor of fractalkine chemokine CX3CL1) (Figure 7B), suggesting its chemotaxis characteristic. We then annotated this population as MP4_Cx3cr1Hi_MHC-IIHi. Additionally, MP4 also enriched for *Tgfbr1* (encoding a

receptor of transforming growth factor beta) which indicated its potential role in tissue remodelling, and *Plxdc2* (encoding plexin domain-containing protein 2) which was found a receptor of phosphatase and tensin homolog (PTEN) and its activation switched tumour associated macrophages to an inflammatory phenotype (Zhang et al., 2024) (Figure 7B). Interestingly, this population also corresponds to a previously-identified *Cx3cr1*HiMHC-IIHi*Lyve1*Lo cardiac MP subset that localised close to epicardial sympathetic nerves (Chakarov et al., 2019), but its function remained unclear. MP5 had most of its features overlapped with MP4, but exhibited a higher *Ccr2* expression than MP4 (Figure 7B). We thus annotated it as MP5_Ccr2Hi_MHC-IIHi, a classic MDM population (Bajpai et al., 2019).

We also identified a special macrophage population featuring high expression of *Trem2* (encoding triggered receptor expressed on myeloid cells 2) (Figure 7B). A similar population was found in the hearts of a sepsis mouse model, which scavenged dysfunctional mitochondria and thus promoted cardiac homeostasis in sepsis (Zhang et al., 2023). In the myocardial infarction (MI) model, this population was expanded during the late phase and played a key role in tissue repair (Jung et al., 2022), featuring an anti-inflammatory but potentially pro-fibrotic phenotype (Gong et al., 2024). Indeed, MP6_Trem2Hi also enriched for *Spp1* and *Fn1* (Figure 7B), both encoding secreted protein (secreted phosphoproetin 1, or osteopontin, and fibronectin 1, respectively) that contribute to cardiac fibrosis (Sawaki et al., 2018, Valiente-Alandi et al., 2018). Importantly, an *SPP1*$^{+}$ macrophage population was identified in human failed hearts and was suggested to aggravate local tissue fibrosis (Fu et al., 2023).

MP7 featured the expression of interferon-related genes, including *Ifi44*, *Ifit2* and *Irf7* (Figure 7B). Thus, we annotated this population as MP7_Interferon.

The smallest MP cell state, MP8_Proliferative, was characterised by classic proliferation markers: *Top2a* and *Mki67*, as well as Knl1 (encoding kinetochore scaffold 1), which plays a key role regulating cytokinesis during proliferation (Gao et al., 2023) (Figure 7B).

DCs were identified by specific expression of *Zbtb46* to distinguish them from other immune lineages (Satpathy et al., 2012), as well as enriched expression of MHC-II molecules (Figure 7B). We identified 2 distinct conventional DC populations and annotated them according to a well-established nomenclature: conventional dendritic cells type 1 (cDC1) and type 2 (cDC2) (Guilliams et al., 2014, Durai and Murphy, 2016). cDC1 featured the expression of *Clec9a* and *Xcr1*, both encoding cDC1-specific surface antigens (Piva et al., 2012, Crozat et al., 2010), as well as *Irf8*, encoding a key transcription factor driving the differentiation of cDC1 during development (Jirmo et al., 2023) (Supplementary Figure 7B). cDC2 was characterised by enriched expression of *Cd209a*, encoding CD209 (or DC-SIGN) (Brown et al., 2019), as well as *Relb* and *Irf4* whose encoded transcription factors control cDC2 development (Gargaro et al., 2022, Bajana et al., 2016) (Figure 7B).

NEUT featured classic neutrophil markers *S100a8* and *S100a9*, encoding S100 calcium binding protein A8 and A9 (Sprenkeler et al., 2022), as well as *Csf3r* (colony stimulating factor 3 receptor) (Figure 7B).

We also mapped the classic markers of another important myeloid lineage monocytes, including *Ly6c1* and *Ly6c2*, which were not expressed across all the myeloid cell states, suggesting the absence of identifiable monocyte population in our dataset (Figure 7B).

Upon completion of annotation, we performed milo analysis to detect the abundance shifts of myeloid cell states following Dox treatment. We did not observe any significant population changes in the DOX_3D group (Figure 7C), but discovered significant enrichment of MP6_Trem2Hi and cDC2 in the DOX_6W group (Figure 7D). Notably, neighbourhoods of cDC2 were found exclusive to the DOX_6W group (Figure 7D), with no neighbourhood of this cell state identified in the DOX_3D or VEH group (Figure 7C-D), highlighting the disease specificity of this cell state.

3.3.2 Myeloid cells display distinct and pro-inflammatory signalling following Doxorubicin treatment

Following the annotation of MYE cell populations, we then moved on to explore the interactions within immune cells, and their crosstalk with other cardiac cell types using CellChat. In the DOX_6W group, myeloid cells were also predicted to send signal regulatory protein beta 1 (SIRPB1) signals to various cell types (Figure 8A). cDC2 was found as the primary sender, with MP4, MP5 and neutrophils (NEUT) contributing as well. Fibroblasts and other myeloid cells, including MP1, MP3 and cDC1 were predicted to be the main targets (Figure 8B). Although the exact function of SIRPB1 is poorly defined, it was found to regulate the expression of inflammatory factors in cultured macrophages (Geng et al., 2024), and a gain-of-function frameshift variant in *SIRPB1* gene promoted the synthesis of pro-inflammatory cytokines (Tang et al., 2023). These findings together suggest a potential role of SIRPB1 in activating macrophages and promoting the production of pro-inflammatory cytokine in the heart.

Another signalling pathway, SPP1, was significantly enhanced in the DOX_6W group (Figure 8C). Notably, MP6_Trem2Hi was predicted as the exclusive sender of SPP1 signal (Figure 8C). Cardiomyocytes (CM), fibroblasts (FB) and other macrophage (MP) populations were predicted as the main targeted cell types (Figure 8D). Moreover, we found increasing trend of *Spp1* expression in MP6 following DOX treatment at 6-week (Figure 8E). Indeed, SPP1 (or osteopontin, OPN) is typically lowly expressed in normal hearts, but can be elevated upon various stress signals (Mori et al., 2010, Zahradka, 2008).

We then explored potential establishment of inflammation in our DOX-induced cardiotoxicity model. We first examined the expression of genes encoding the C-C chemokines, including *Ccl6*, *Ccl8* and *Ccl12* in the sender MPs, and indeed these genes showed at least an increasing trend in Dox-treated groups, with Ccl8 being significantly up-regulated in MP2 at both timepoints, and both *Ccl6* and *Ccl8* up-regulated in MP1 in the DOX_6W group (Figure 9A). These genes all encode for ligands of the *Ccr2* receptor which is a well-established marker of immune cell recruitment and inflammatory signalling in the heart, particularly during injury and stress (Bajpai et al., 2019, Hulsmans et al., 2023). In line with these findings, DOX treatment at 6-week significantly enhanced the CCR2 pathway, mainly within the myeloid populations, with contributions from fibroblasts (FB) and signals directed towards T cells (Figure 9B). We further dissected the roles of different myeloid cell states in the CCR2 pathway, which revealed

MP3 and MP2 as the major senders, and MP4, MP5, MP6 as the predominant receivers (Figure 9C). Notably, MP3 and MP2 were both defined as tissue resident macrophages (TRMs), while MP4, MP5 and MP6 all exhibited features of monocyte-derived macrophages (MDM), expressing *Ccr2* (Figure 7A-B). FB8_IR also acted as a sender (Figure 9B), as they expressed genes encoding CCR2 ligands, including *Ccl2* and *Ccl7* (Figure 4B).

To summarise, we revealed distinct roles of various myeloid populations following DOX treatment with SIRPB1 and SPP1 signalling pathway as new potential mediators of DOX-induced cardiac remodelling. Moreover, we speculated the CCR2 signalling pathway as the main driver of DOX induced cardiotoxicity, with a crosstalk involving MYE, FBs and T cells (Figure 9D). Given the involvement of T cells in CCR2 signalling in DOX_6W, we sought to deeply investigate on the role of LYM cells and interaction with other cardiac cell types as they may greatly impact the pathological response to DOX-induced cardiac injury.

3.3.3 Doxorubicin induces expansion of CD8+ T cells

Lymphoid cells in the heart typically feature two lineages: T/natural killer (NK) cells and B cells. T/NK cells were identified using well-established lineage markers: *Ms4a4b* (encoding a CD20 homologue in T cells), *Cd247* (encoding part of the T-cell receptor complex) and *Il7r* (encoding CD127). We also distinguished $CD4^+$ and $CD8^+$ T cells based on their specific expression of surface marker-encoding genes. TC1_CD4 enriched for *Cd4*, and genes encoding $CD4^+$ T cell-specific transcription factors: *Lef1* and *Tcf7* (Figure 10A) (Yu et al., 2012). TC2_CD8 exclusively expressed CD8 complex-encoding genes *Cd8a* and *Cd8b1*, as well as *Cd44*, whose encoded surface marker is usually highly expressed on activated $CD8^+$ T cells (Figure 10B) (Klement et al., 2018). NK cells as a minor population in this lineage were characterised by enriched expression of genes encoding NK-specific surface markers: *Ncr1* (natural cytotoxicity triggering receptor 1) and *Klrd1* (killer cell lectin like receptor D1), along with *Gzma* (encoding granzyme A, a cytotoxic serine protease) (Figure 10B).

B cells were identified by enriched expression of *Ebf1* (encoding a transcription factor regulating B cell development and differentiation), as well as immunoglobulin (Ig)-encoding genes, including *Ighd* (Igδ) and *Cd79a* (Igα, part of the B-cell receptor complex) (Figure 10B). BC1 did not express any other specific genes, while BC2 featured higher expression of *Cxcr5* (encoding CXC motif chemokine receptor 5), *Tgfb1* (encoding transforming growth factor beta 1) and *Irf5* (encoding a transcription factor in NFkB pathway) (Figure 10B), which is consistent with a distinct B cell subset exclusively found in the heart, namely “heart-associated B cells”. In contrast to the antigen-driven germinal centre B cells, this unique cardiac B cell population infiltrated the infarcted heart through the CXCL13-CXCR5 axis, and contributed to fibrotic remodelling through TGFB1 production (Heinrichs et al., 2021).

Next, we applied milo to assess the lymphoid cell population shifts following DOX treatment. No significant shift was detected when comparing DOX_3D with the VEH group (Figure 10C). In the DOX_6W group, we observed an enrichment of $CD8^+$ T cells (Figure 10D), which is in line with a recent finding (Bayer et al., 2023), as well as a trend of $CD4^+$ T cells enrichment and BC1 depletion (Figure

10D).

3.3.4 CD8⁺ T cells predicted to interact with a stressed cardiomyocyte cell state upon Doxorubicin treatment

Next, we focused on the signalling of CD8⁺ T cell population, which significantly expanded at 6 weeks after DOX treatment (Figure 10D). Although CD8⁺ T cells only constitute a small population among all cell states (Figure 1C; Figure 2), their unique roles in identifying and eliminating dysfunctional cells position them as the exclusive receiver of the major histocompatibility complex class I (MHC-I) – CD8 pathway (Figure 11A-B), and the predominant sender of the Fas ligand (FASLG) pathway (Figure 10C-D). Myeloid (MYE) and endothelial cells (EC) were two main cell types predicted to present MHC-I molecules to CD8⁺ T cells, with the signalling strength of MHC-I – CD8 pairs significantly increased in the DOX_6W group (Figure 11A). Within MYE, MP1, MP3_Igf1Hi_Ccr2-, MP4_Cx3cr1Hi_MHC-IHi, as well as cDC2 were predicted as the main senders (Figure 11B).

CD8⁺ T cells acted as senders in the FASLG pathway, expressing FAS ligand as a key mechanism to exert their cytotoxic effect on FAS receptor-expressing cells. This pathway was exclusive to the DOX_6W group, with EC predicted to be the main target (Figure 10C-D), suggesting a potential role of CD8⁺ T cells in promoting EC apoptosis upon DOX treatment. In line with these results, we also observed a trend of increased expression in the genes encoding CD8 (*Cd8a* and *Cd8b1*) and FAS ligand (*Fasl*) following DOX treatment (Figure 11E), which may also contribute to the enhanced signalling, underscoring CD8+ T cells activation at dox 6-week.

We then investigated the crosstalk of CD8⁺ T cells with other major cardiac cell types, particularly cardiomyocytes (CM) and fibroblasts (FB), in the context of DOX-induced cardiotoxicity. Given that signals from CD8⁺ T cells were often overshadowed by those from larger cell populations, we used a different approach, filtering for the ligand-receptor pairs where CD8⁺ T cells acted as sender, and CM or FB as receiver. This approach allowed us to identify the Galectin-9 (Gal-9) – CD44 signalling between these populations, which was predicted to be exclusive to DOX-treated groups, primarily in DOX_6W (Figure 11F). Notably, the strongest signals were predicted in CM3_Stressed as receiver, followed by CM1_Intermediate. Two activated FB populations, FB3_Activated and FB7_WntX, were also predicted to be Gal-9 targets in the DOX_6W group (Figure 11C).

To cross-validate this finding, we examined the expression of genes encoding the ligand (*Lgasl9*) and the receptor (*Cd44*) in the corresponding cell states, respectively. *Lgals9* level in CD8⁺ T cells did not show significant changes across three groups (Figure 11G), but the expression of *Cd44* in CMs and FBs demonstrated a strong correlation with the signalling strength result (Figure 11G). Gal-9 has been indicated as a cytotoxic factor through apoptosis or non-apoptosis pathways in various cell types (Choukrani et al., 2023, Itoh et al., 2019, Fujita et al., 2017), although its direct effects on cardiomyocytes and cardiac fibroblasts remain poorly understood, particularly in DIC.

Collectively, we revealed a complex CD8⁺ T cells-centred crosstalk network with other cardiac cell types. MYE cells are predicted to present MHC-I molecules to CD8⁺ T cells via the CD8 receptor,

potentially modulating the inflammatory response following DOX treatment. Endothelial cells (EC) were also predicted to play a role in antigen presentation, and in turn were regulated through FASLG pathway, suggesting $CD8^+$ T cell-mediated apoptosis of EC. In addition to the canonical $CD8^+$ T cell signalling, we also demonstrated increased interactions between $CD8^+$ T cells and stressed cardiomyocytes (CM) and activated fibroblasts (FB) upon DOX treatment. In particular, CellChat revealed a stressed CM cell state as the main target of the CD8+ T cells via Galectin-9 – CD44 signalling (Figure 11H), which led us exploring DOX-induced damage in CMs.

3.4 Doxorubicin drives the progression of cardiomyocytes from basal to stressed cell state with Gask1b as new potential marker and determinant of cardiotoxicity

3.4.1 Doxorubicin up-regulates stressed cardiomyocyte populations

We first sought to explore the heterogeneity within the CM population by applying unbiased clustering. Using the Leiden algorithm we identified 5 subpopulations (Figure 12A). Among the 5 CM cell states, CM1_Intermediate, CM2_Basal and CM3_Stressed together consisted of nearly 90% of total CMs and formed a distinct block from the other two smaller populations, CM4_Energetic and CM5_Conduction (Figure 12A). CM3_Stressed, the most distinct state in this block, was characterised by the enrichment of *Myh7*, the foetal isoform of myosin heavy chain encoding beta-myosin heavy chain, typically upregulated in maladaptive responses (Satoh et al., 2019), *Nppb*, encoding a natriuretic peptide hormone which is a well-known marker of cardiac stress (Man et al., 2018), and *Atf3*, a well-established cardiac stress-response gene (Zhou et al., 2018) (Figure 12B). CM1_Intermediate also significantly enriched for *Nppb*, but at a lower level compared to CM3_Stressed (Figure 12B). In contrast, CM2_Basal expressed negligible levels of *Nppb* and *Myh7*, but showed the highest expression of *Tnni3k*, encoding cardiac troponin I-interacting kinase which is key to CM S-phase activity after injury (Reuter et al., 2023), *Kcnd2*, a potassium voltage-gated channel gene crucial for maintaining normal electromechanical properties (Kim et al., 2022, Bohne et al., 2021), and *Angpt1* encoding angiopoietin-1, which was found to promote myocyte survival (Dallabrida et al., 2005) (Figure 12B). Overexpression of angiopoietin-1 also prevented DOX-induced apoptosis in H9c2 cardiomyocytes, suggesting its potential cardio-protective function (Ren et al., 2012).

Moving onto two smaller states with potentially specialised functions, CM4_Energetic highly expressed nucleus-encoded mitochondrial genes such as *Cox4i1*, *Atp5g1* and *Ndufb9*, as well as sarcomeric genes like *Myh6* and *Myl2* (Figure 12B), suggesting a metabolically active cell state. A similar energetic CM state enriched for mitochondrial genes was also found in a large-scale adult human heart single-nucleus atlas study (Litvinukova et al., 2020), confirming the identity of this CM subpopulation.

The least abundant cluster, CM5_Conduction, featured specific expression of *Hcn4*, encoding pacemaker-associated channel found in sinoatrial node (SAN) and atrioventricular node (AVN) pacemaker cells (Goodyer et al., 2019, Kanemaru et al., 2023). This population also expressed ventricular conduction system markers including *Cacna1g* (encoding T-type calcium channel subunit

alpha 1g) and *Kcne1* (potassium voltage-gated channel subunit 1) (Goodyer et al., 2019, Kanemaru et al., 2023) (Figure 12B).

We then utilized Milo to detect differential abundance of CM cell states between groups. Milo revealed the enrichment of CM1_Intermediate neighbourhoods in both DOX-treated groups, while neighbourhoods of CM3_Stressed were predominantly found in the DOX_6W group only (Figure 12C-D). In contrast, neighbourhoods of CM2_Basal, representing a relatively healthy state, were enriched in the VEH group, compared to either DOX_3D or DOX_6W group (Figure 7C-D). Collectively, this data underscores a profound perturbation driven by DOX in CMs.

3.4.2 Trajectory analysis highlights a basal-to-stressed continuum in cardiomyocytes

To identify genes with continuous expression changes towards the stressed state, we performed trajectory analysis scFates (Faure et al., 2023). We uncovered a phenotypic trajectory from CM2_Basal through CM1_Intermediate to CM3_Stressed (Figure 13A), along with 252 significant signature genes. These genes were organised in 2 distinct modules based on the similarity of their expression pattern, either increasing or decreasing (Figure 13B-C).

Among genes with increasing expression along the trajectory, we found defining markers of CM3_Stressed, like Nppb and Myh7 (Figure 12B). A number of genes encoding CM structural proteins such as *Flnc* (filamin C), *Myot* (myotilin) and *Des* (desmin) also showed increased expression towards the stressed end of trajectory (Figure 13B). Genetic variants of these genes have been linked with various cardiomyopathies (Agarwal et al., 2021, Bermudez-Jimenez et al., 2024), but their role in DOX-induced cardiomyopathy is unclear. Additionally, genes encoding pro-fibrotic factors and regulators, including *Tgfb2* (encoding transforming growth factor β2), *Smad4*, *Ccn2* (encoding connective tissue growth factor) were up-regulated along the Basal-to-Stressed trajectory (Figure 13B), suggesting a potential role of stressed CMs in pathogenic tissue remodelling upon DOX treatment (Leask, 2010). Interestingly, Toll like receptor 4 encoded by *Tlr4*, which was linked to DOX-induced ferroptosis in CMs (Zhao et al., 2024), as well as being a potential early biomarker of DIC (Pop-Moldovan et al., 2017), was also among the up-regulated genes along the trajectory (Figure 13B).

Conversely, we identified a set of genes with decreasing expression from CM2_Basal to CM3_Stressed, including *Tnni3k*, *Kcnd2* and *Angpt1,* that were previously described as CM2_Basal markers (Figure 12B; Figure 13C). *Myh6* encoding the mouse adult isoform of alpha-myosin heavy chain (αMHC) also showed decreasing expression (Figure 13C), similar to that observed in a heart failure model (Lu et al., 2022a). The other down-regulating gene related to cardiomyocyte sarcomeric function was *Mylk3*, encoding myosin light chain kinase 3 (Figure 13C), whose loss-of-function mutation was linked with systolic dysfunction, and its restoration ameliorated cardiac contractility (Hitsumoto et al., 2023). Similarly, the expression of *Erbb4* (Erb-B2 receptor tyrosine kinase 4) decreased along the trajectory (Figure 13C), consistent with the finding that ErbB4 expression was significantly reduced in the hearts of mice after DOX treatment (Horie et al., 2010). Other examples of decreasing genes include those encoding peroxisome proliferator activated receptors and their coactivators (*Ppara* and *Ppargc1a*)

(Figure 13C), both key to maintaining normal mitochondrial function are protective against Dox-induced or other aetiologies of cardiomyopathy (Zhu et al., 2023, Liu et al., 2018), as well as genes encoding fibroblast growth factors like *Fgf1*, a well-characterised cardio-protective factor (Palmen et al., 2004) and *Fgf14* which was down-regulated in CMs upon oxidative stress (Zhao et al., 2020) (Figure 13C). These results together suggested a continuum of CMs from Basal to Stressed state, with CM1_Intermediate as a bridging state and a precursor of CM3_Stressed.

3.4.3 Identification of Gask1b as a novel stress gene in Doxorubicin-induced cardiotoxicity

In addition to genes with known function in DOX-induced cardiotoxicity or in other types of cardiomyopathies, a previously uncharacterized gene, *Gask1b* emerged from the trajectory analysis (Figure 13B) as significantly upregulated along the trajectory. *Gask1b,* encoding golgi associated kinase 1b, was significantly enriched in CM3_Stressed in DOX_3D and showed, despite not significant, sustained trend of overexpression in DOX-6W group by DEGs analysis (Figure 13D). In line with these data, its expression spiked at the stressed end of trajectory (Figure 13E). Intriguingly, Gask1b has been associated to cellular stress responses and cancer progression (Zheng, 2022), (Chen, 2024), suggesting a possible role in the interplay between cardiotoxicity and tumor biology. However, only a few studies have been published, and its exact function still remains largely unknown. For this reason, we decided to perform validation experiments to further investigate the role of *Gask1b* in the context of cardiotoxicity.

To validate the up-regulation of *Gask1b* at the protein level following DOX treatment., we performed western blotting on mouse heart tissues treated with both 3-day and 6-week DOX regimen. Western blot analysis showed 2-fold higher expression of Gask1b in both DOX-3D and DOX_6W treatment groups than in VEH, corroborating snRNAseq data (Figure 14A). Immunofluorescence staining of mouse heart tissues further confirmed the upregulation of Gask1b protein expression at both 3-day and 6-week (Figure 14B). Notably, Gask1b staining revealed an expression pattern reminiscent of the Golgi cisternae, in addition to the presence of the protein at the plasma membrane (Figure 14B).

Collectively, this data identifies *Gask1b* as a novel cardiac stress marker and a potential player of DIC.

3.4.4 Functional validation of *Gask1b gene* as a novel player of Doxorubin-induced cardiotoxicity

To validate the role of Gask1b in mediating CM stress response upon DOX treatment and to assess its functional conservation across different organisms, we first silenced Gask1b in cmlc2:GFP zebrafish characterized by cardiomyocyte-specific GFP expression using anti-Gask1b morpholinos (see Materials and Methods; Figure 15B). Gask1b-morphants (Gask1b-morph) and scrambled-injected control zebrafish embryos (Scrambled-morph) were subjected to 40 uM DOX treatment for 42 hours, and heart function was assessed by measuring fractional shortening (FS). In line with previous findings (Liu et al., 2014), DOX treatment significantly impaired heart contractility in Scr-morph zebrafish larvae, resulting in a 30% reduction in FS (Figure 15C-D). Conversely, DOX failed to significantly decrease FS in Gask1b-morph larvae (Figure 15C-D), suggesting a protective role for Gask1b against DOX-induced

systolic dysfunction. Notably, Gask1b silencing did not affect larval development (data not shown) and did not alter basal heart contractility (Figure 15D), indicating that Gask1b gene is not essential for early zebrafish development. To substantiate the protective role of Gask1b against DOX-induced damage, we examined the expression of γH2A.X, a marker of DNA double-strand breaks in DOX-treated zebrafish larvae. In line with FS measurements, γH2A.X was lower in Gask1b-morph than in control Scr-Morph upon DOX administration (Figure 15E), suggesting that Gask1b silencing confers protection against DOX-induced DNA damage in zebrafish.

To investigate whether *Gask1b* silencing mediate protection also in mammals, we carried out in vitro experiments by isolating neonatal mouse ventricular cardiomyocytes (NMVCs; see Materials and Methods) and infecting them with adenovirus (ADV5) carrying a short hairpin RNA (shRNA) against *Gask1b* before exposure to 1 uM DOX. Western blot analysis confirmed that Gask1b protein levels were significantly reduced in NMVCs infected with shGask1b-Ad compared to a control shScrambled-Ad (Figure 16B). In keeping with the findings in Gask1b-morph, DOX-induced γH2AX foci formation was significantly reduced in shGask1b-ADV5 NMCMs following 1uM DOX treatment, confirming that Gask1b silencing attenuates DOX-induced DNA damage also in mouse cardiomyocytes.

To confirm the protective role of Gask1b silencing *in vivo*, adult mice were injected with adeno-associated virus serotype 9 (AAV9) carrying either a shRNA targeting Gask1b (shGask1b-AAV9) or a scrambled control (shScrambled-AAV9), before treating them with DOX (Figure 16E). Global circumferential strain (GCS) analysis revealed a trend toward protection, as the DOX-induced reduction in GCS was partially attenuated in shGask1b-AAV9-injected mice (Figure 16F). Consistently, in these mice, DOX-induced cardiac atrophy was significantly reduced in the shGask1b-AAV9 compared to shScrambled-AAV9-injected mice, as evidenced by CM cross-sectional area measurements, suggesting that Gask1b targeting mitigate, at least partially, DOX-induced cardiac damage *in vivo* (Figure 16 G-H).

Altogether, these findings demonstrate that *Gask1b* plays a crucial role in pathogenesis of DIC across both zebrafish and mammalians and suggests its targeting as a way to protect against DOX-induced cardiac damage.

3.5 *GASK1B* is upregulated in failing human hearts following Doxorubicin regimen

We next sought to investigate the translational relevance of Gask1b as a new stress marker gene in DIC. *GASK1B* gene expression was examined at single nucleus level in human heart samples from a patient who developed severe DOX-induced cardiomyopathy requiring heart transplantation and 12 control donors. Human hearts were processed for snRNAseq analysis following established pipelines (Litvinukova et al., 2020; Skelly et al., 2018; Wolfien et al., 2020). Unbiased Leiden subclustering of ventricular cardiomyocytes (vCM) revealed six distinct subpopulations (Figure 17A) and *GASK1B* expression was examined across these six subpopulations. Notably, vCM1 and vCM3 displayed a trend of upregulation in response to DOX treatment compared to control donor tissues (Figure 17B). Interestingly, the smallest subpopulation, vCM5, exhibited the strongest upregulation of *GASK1B* expression (Figure 17B). Additionally, when comparing overall *GASK1B* expression in vCM between

DOX-treated and control hearts, a higher expression level was observed in the DOX-treated heart, further supporting the role of *GASK1B* in the cardiotoxic stress response (Figure 17C). Additionally, immunohistochemistry assay revealed higher GASK1B expression in DOX-damaged hearts than in the control donor (Figure 17D). Similar to the findings in mouse hearts, GASK1B was enriched in Golgi-like structures and at the plasma membrane. Collectively, our findings support *GASK1B* as a novel stress marker in humans affected by DIC.

3.6 The Dual Role of GASK1B in Doxorubicin-induced cardiotoxicity and Acute Myeloid Leukaemia Progression

While our findings establish *Gask1b* as a key marker and mediator of DIC, the impact of its targeting on cancer growth remains unknown. This is particularly relevant for DOX-sensitive tumors such as acute myeloid leukemia (AML), the most common childhood malignancy, where DOX remains a cornerstone of treatment despite its significant cardiotoxicity (Hefti et al., 2016; Poonia et al., 2024). This prompt us investigating the role of *Gask1b* in AML. Firstly, we tested whether DOX could induce GASK1B overexpression in AML cells. Western blotting analysis confirmed significant GASK1B upregulation at protein level after 24 hours of DOX treatment (Figure 18A), suggesting a conserved mechanism by which DOX induces stress-related gene expression in both cardiomyocytes and AML cells. To investigate the biological and clinical relevance of these observations, we next analysed using Kaplan-Meier Plotter publicly available datasets (GSE1159, GSE12417, GSE37642; GSE6891), revealing a striking correlation between high GASK1B expression and reduced overall survival in AML patients (Figure 18C). Notably, this adverse association was specific to patients who received chemotherapy (Figure 18D-E), indicating that GASK1B may drive a more aggressive phenotype in AML and influence tumor behavior under chemotherapeutic treatment. These findings suggest a dual role for GASK1B as both a stress marker and determinant of DIC as well as potential contributor to poor outcomes in DOX-treated AML. This raises the intriguing possibility of dual targeting GASK1B to protect against DOX-induced heart damage while potentially improving chemotherapy outcomes in AML.

4. DISCUSSION

In this work, we developed a comprehensive murine cell-by-gene heart atlas to explore both acute and chronic phases of DIC, utilizing the cutting-edge single-nucleus transcriptomics (snRNA-seq) technique. This approach allowed us to capture the nuanced transcriptional landscape of the DOX-treated heart at an unprecedented resolution. Our dataset facilitated the identification of eight major cardiac cell types, which we further dissected into 42 distinct cell states through unbiased clustering methods. Each cell state was meticulously annotated by leveraging known marker genes for established cell populations and integrating novel insights from top unbiased marker genes, which revealed previously uncharacterized or inferred functions. We observed dynamic shifts in the population of each cell type and state in response to DOX treatment, providing a temporal view of cellular adaptations and maladaptations during the progression of cardiotoxicity. These population shifts shed light on key cellular contributors to the pathology, offering a deeper understanding of how DOX perturbs the cardiac microenvironment. Furthermore, we conducted an in-depth cell-cell interaction analysis with CellChat tool, which revealed significant changes in intercellular communication under DOX treatment. By comparing signalling strength across multiple pathways, we identified a putative complex network of crosstalk among different cardiac cell types. This network delineates how DOX alters cellular communication, potentially disrupting homeostasis and exacerbating injury. Notably, the analysis highlighted specific pathways that may be crucial for maintaining cardiac function or mediating damage under stress, offering potential targets for therapeutic intervention. This comprehensive atlas not only enhances our understanding of the molecular underpinnings of DOX-induced cardiotoxicity but also provides a valuable resource for future studies aiming to unravel the complex interplay between different cardiac cell types during pathological stress. Importantly, in this study, we utilised single-nucleus transcriptomics which allowed us to profile all cardiac cell types, including cardiomyocytes. To date, the vast majority of single-cell level study on mouse hearts applied single-cell sequencing, which hampered the characterisation of cardiomyocytes due to their large size not compatible with microdroplet-based techniques. Nevertheless, those single-cell studies provided plentiful insights into the cellular and molecular signatures of various cardiac diseases in mouse models.

Using drug2cell, which integrates drug-target interaction data from the ChEMBL database, we identified fibroblasts (FB), cardiomyocytes (CM), and myeloid cells (MYE) as the primary cell types targeted by DOX. This finding underscores the importance of these cell types in mediating DOX-induced cardiotoxicity, based on high expression of known DOX targets. These results were corroborated by analysis with Milo, a differential abundance analysis tool that detects subtle shifts by clustering nuclei into neighbourhoods and comparing their distributions between control and DOX-treated groups, which identified significant enrichments and depletions in FB, MYE, and CM neighbourhoods. The close alignment of these findings from Milo with the drug2cell prediction reinforces the critical involvement of

these cell types in the later stages of DOX-induced cardiotoxicity. This concordance between the two methods highlights a consistent narrative: FB, MYE, and CM are key players in the chronic phase of DOX cardiotoxicity, likely due to their roles in stress response, inflammation, and structural remodelling. Notably, Milo did not reveal significant population shifts at the global and single-cell state level at the 3-day time point, except for perturbations observed in CM. This aligns with expectations, as a single 4 mg/kg DOX dose over three days likely initiates early stress responses without inducing substantial changes in cell composition, suggesting that this early phase may be too short to manifest marked cellular remodelling.

While this study provided valuable insights into the roles of FB, MYE, and CM, it is important to note that vascular cells (mural and EC) were not extensively explored, despite their potential involvement in DOX-induced cardiotoxicity. Although our primary findings highlighted FB, MYE, and CM as major players, the contribution of mural and endothelial cells may still be significant, particularly through their interactions with the identified key cell types. Future investigations are warranted to elucidate the specific roles of these vascular populations and their interactions within the cardiac microenvironment under DOX stress.

Among the FB populations identified in this study, the FB3_Activated population stands out as a putative critical driver of ECM remodeling and fibrotic progression upon DOX treatment, particularly in the late stage of cardiotoxicity, exhibiting notable expansion by six weeks post-DOX administration. Different from other cardiac diseases such as myocardial infarction (MI), where fibrosis can comprise up to 40% of the affected tissue, fibrosis is often considered a less prominent hallmark of DIC. Neverthless, the findings of this study underscore the significant role that FB3_Activated plays in the progression of DIC. This expanded subset acquired myofibroblast-like features, exhibited a distinct expression pattern of ECM genes, and could play a crucial role in regulating ECM organization. In these cells, of particular interest is the upregulation of Thbs1 at 6-week DOX treatment, which was further validated by Western blot analysis. Notably, Thbs1 has been identified as a potential biomarker for fibrosis (Bosman et al., 2023), reinforcing its diagnostic value. Beyond its role as a biomarker, Thbs1 also induced autophagy in CMs, resulting in lethal cardiac atrophy (Vanhoutte et al., 2021)., known to be an iconic hallmark of DIC (Willis et al., 2019, Chen et al., 2022a). In line with these previous findings, our CellChat data predict Thbs-1 as key participant in signaling pathways that facilitate crosstalk between FB3_Activated fibroblasts and other cardiac cell types, such as myeloid cells, endothelial cells, and cardiomyocytes. These interactions might play a pivotal role in orchestrating the fibrotic response, promoting tissue remodeling, inflammation, and ultimately leading to impaired CM function, thus highlighting Thbs-1 gene as an attractive target for mitigating cardiac dysfunction and remodeling associated with DIC.

Our CellChat analysis also revealed a complex immune response in DOX-treated hearts, characterized by shifts in myeloid and lymphoid cell populations. The increased abundance of MP6_Trem2Hi and

type-2 conventional dendritic cells cDC2 at 6-week DOX treatment suggests a pivotal role of these two populations in cardiac remodelling and inflammation. MP6_Trem2Hi, with enriched expression of SPP1, may contribute to pro-fibrotic processes, while the cDC2 population signals through SIRPB1, potentially driving pro-inflammatory cytokine production. In particular, MP6_Trem2Hi macrophages has been found to emerge at late phases of cardiac injury or heart failure, as shown in various models including MI (Rizzo et al., 2023, Jung et al., 2022), septic cardiomyopathy (Zhang et al., 2023), and hypertensive heart failure (Smart et al., 2023). This *Trem2*^{Hi} MP population was indicated to have a reparative population, exhibiting an anti-inflammatory phenotype (Rizzo et al., 2023, Smart et al., 2023), but its role in fibrotic remodelling is controversial. In the myocardial infarction (MI) model, this population was expanded during the late phase and played a key role in tissue repair (Jung et al., 2022), featuring an anti-inflammatory but potentially pro-fibrotic phenotype (Gong et al., 2023). Our analysis also revealed enhanced CCR2 signaling, predominantly involving both TRMs and MDMs, indicating cell recruitment and inflammatory response. Additionally, in line with previous findings (Bayer et al., 2024), we found the expansion of CD8+ T cells at 6-week, underscoring increased interactions with multiple cardiac cell populations, including CMs, highlighting a potential involvement of this lymphoid population in contributing to DOX-induced cell damage in the heart by interacting with other cell types. Among the key findings, Gal-9 – CD44 signalling emerged as a critical pathway, particularly in the DOX_6W group. CD8+ T cells predominantly sent Gal-9 signals, with CM and FB as main receivers. CD8+ T cells predominantly sent Gal-9 signals, with CM and FB as the primary recipients. This signalling was notably enriched at both the 3-day and 6-week, with a pronounced presence in the CM3_Stressed subpopulation, indicating a disease-specific role for Gal-9 and CD8+ T cells in immune modulation during DOX-induced cellular damage. The involvement of the Gal-9 – CD44 axis in this context highlights its potential contribution to cardiotoxicity progression. Further investigation could reveal targeted therapeutic strategies to mitigate cardiac injury by disrupting this specific signalling pathway

Within CMs, we identified a phenotypic trajectory that traced the progression from a basal to a stressed state and observed an increase in stressed CMs upon DOX treatment. Trajectory analysis highlighted a progressive upregulation of Gask1b as cells transitioned to the stressed state, a finding confirmed through Western blot and immunofluorescence staining. Interestingly, *Gask1b* demonstrated marked expression within CMs and localized to the plasma membrane, a previously unappreciated aspect in these cells. This localization might suggest a distinctive role in cellular stress signaling and response, though the exact molecular mechanisms by which *Gask1b* contributes to DOX-induced cardiotoxicity remain to be fully clarified. Functional validation provided compelling evidence of *Gask1b*'s protective role against DOX-induced cardiotoxicity. In zebrafish, silencing Gask1b via morpholino injection partially mitigated the decline in heart function, as evidenced by improved fractional shortening and reduced DOX-induced DNA damage, demonstrated by lower γH2A.X levels. In NMVCs, Gask1b knockdown using shRNA reduced DOX-induced DNA damage, indicated by decreased γH2A.X foci formation.

Further in vivo experiments in adult mice, utilizing AAV9-mediated Gask1b knockdown, revealed a trend toward protection against DOX-induced cardiotoxicity. Although the attenuation of GCS reduction did not reach statistical significance, it was consistent with a significant reduction in cardiomyocyte atrophy, supporting a potential cardioprotective role of Gask1b silencing. These findings highlight Gask1b's involvement in the pathogenesis of DOX-induced cardiotoxicity and suggest its targeting as a promising therapeutic strategy. However, additional studies are required to validate these observations comprehensively. Future experiments should aim to refine the knockdown approach, for instance, by employing AAV9 vectors with a cardiomyocyte-specific promoter to enhance the precision and longevity of Gask1b silencing. Such strategies will allow a more thorough evaluation of its protective effects and potential translational relevance

We have also demonstrated that Gask1b protein expression is upregulated in response to 24 hours DOX treatment in AML cells. This suggests that Gask1b may function as a conserved stress-related gene across different tissue types, responding to the cellular stress induced by chemotherapy. The clinical relevance of Gask1b upregulation in AML was further highlighted by our analysis of publicly available datasets, which revealed a significant correlation between high Gask1b expression and reduced overall survival in AML patients. Notably, this correlation was only present in patients receiving chemotherapy, further underscoring the association of Gask1b with chemotherapy-induced stress and an aggressive disease phenotype. These findings suggest a dual role for GASK1B: as a stress marker in cardiotoxicity and a potential contributor to poor outcomes in DOX-treated AML. The observation that GASK1B overexpression correlates with lower survival specifically in chemotherapy-treated AML patients highlights its potential role in chemoresistance or tumor adaptation. This raises the intriguing possibility of dual targeting GASK1B to protect against DOX-induced heart damage while potentially improving chemotherapy outcomes in AML. Given the widespread use of DOX in treating AML, such an approach could offer significant clinical benefits by mitigating cardiotoxic side effects while enhancing therapeutic efficacy in cancer.

Overall, we generated a single-nucleus dataset of DOX-treated mouse hearts and identified transcriptional changes driven by DOX in CM at early and late stages of the disease. Furthermore, we identified Gask1b gene, whose role in cardiac pathophysiology was previously unappreciated, as a new potential marker and determinant of DIC and AML progression.

ACKNOWLEDGEMENTS

We acknowledge computational resources and support provided by the Imperial College Research Computing Service (http://doi.org/10.14469/hpc/2232).

5. FIGURES

Figure 1

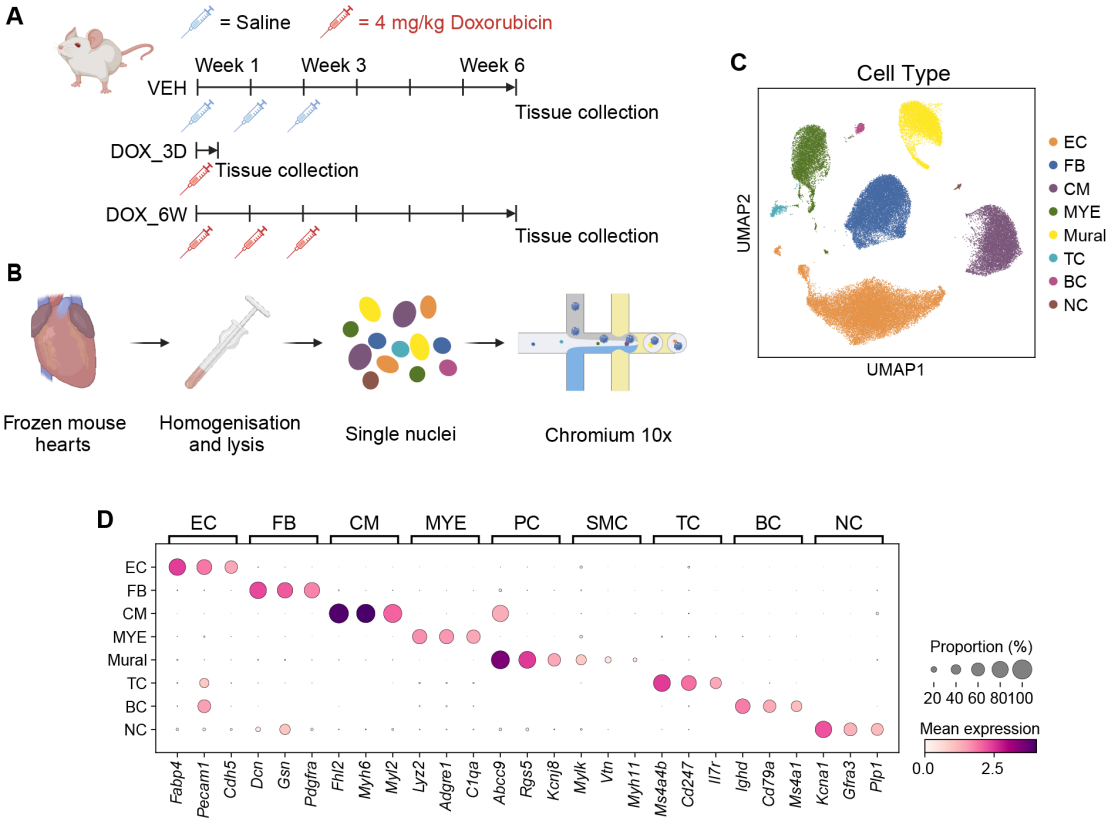

Figure 1. Generation of a murine nucleus-gene heart atlas of Doxorubicin-induced cardiotoxicity. A, Schematic of the study design. Twelve female BALB/c mice were randomised into three groups (4 mice per group) and treated with either saline or Doxorubicin (Dox) at different doses (a single injection of 4 mg/kg Dox, or three weekly Dox injections). Mouse hearts were collected either 6 weeks after the first saline (VEH) or Dox (DOX_6W) injection, or 3 days after the single Dox injection (DOX_3D). **B**, Workflow of single-nucleus transcriptomics. Mouse hearts were snap-frozen, homogenised and lysed to extract single nuclei, followed by the standard Chromium 10X transcriptomics pipeline. **C**, UMAP representation of the global object (52,926 nuclei), colour coded by 8 major cell types. Each point represents a single nucleus. EC, endothelial cells; FB, fibroblasts; CM, cardiomyocytes; MYE, myeloid cells; TC, T cells; BC, B cells; NC, neuronal cells. **D**, Dot plot showing marker genes of each cell type. Dot size represents proportion of nuclei expressing the gene in each cell type; dot colour represents the mean Log-normalised expression of each gene. PC, pericytes; SMC, smooth muscle cells.

Figure 2

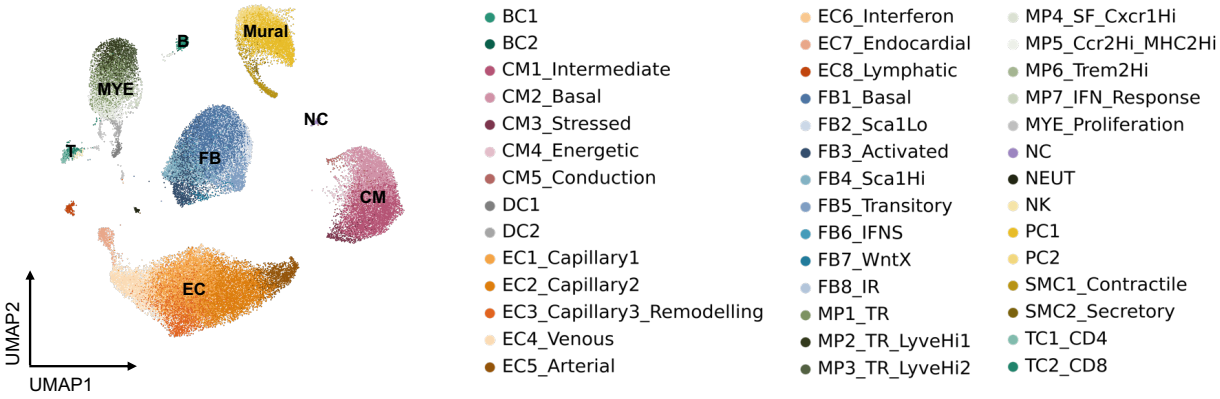

Figure 2. SnRNAseq analysis identified 8 major cel types and 42 cell states. Left, UMAP representation of the global object, colourcoded by cell types and cell states for each cell type. CM, cardiomyocytes; EC, endothelial cells; FB, fibroblasts; MYE, myeloid cells. Right, each cell state is reported and plotted on the global object UMAP.

Figure 3

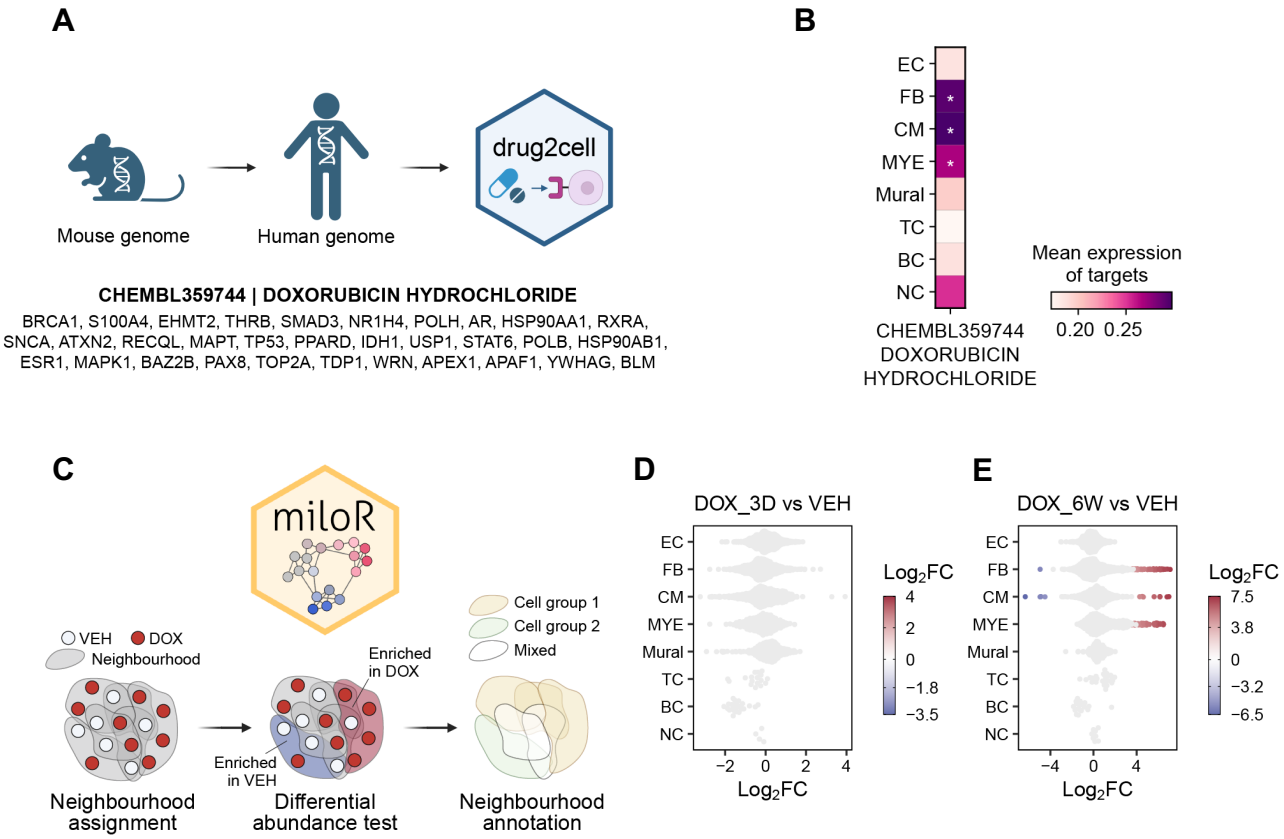

Figure 3. Doxorubicin target prediction and population shifts. A, (Top) Schematic showing the workflow of applying drug2cell. To align with the drug2cell database, mouse genes were converted to their human orthologues using the translate function of mousipy. **(**Bottom**)** Drug2cell-filtered gene targets of Doxorubicin, data retrieved from them ChEMBL database. **B**, Matrix plot showing drug2cell prediction of Doxorubicin-targeted cell types based on expression of known target genes from ChEMBL database. Colour represents the mean Log-normalised expression of the target genes. *, adjusted P value < 0.05 (Wilcoxon rank-sum test). **C,** Schematic showing the workflow of milo. Milo objects were generated for comparisons between the control group (VEH) and a Doxorubicin-treated group (DOX_3D versus VEH or DOX_6W versus VEH, respectively). Nuclei were assigned to partially-overlapping milo neighbourhoods in an unbiased manner, followed by a differential abundance test to identify neighbourhoods significantly enriched in either the VEH or DOX group. Neighbourhoods were annotated by cell groups (cell types or cell states), and those with mixed annotations were excluded from result interpretation. **D**-**E**, Beeswarm plots showing the distribution and enrichment of cell type-annotated Milo neighbourhoods, comparing DOX_3D versus VEH (**D**) and DOX_6W versus VEH (**E**). Each point represents a Milo neighbourhood. Colour represents Log_2 fold change (Log_2FC) of enrichment. Positive values indicate enrichment in Dox-treated groups, and negative values VEH group. Only the neighbourhoods with FDR < 0.1 (edgeR) were considered significant and coloured. EC, endothelial cells; FB, fibroblasts; CM, cardiomyocytes; MYE, myeloid cells; TC, T cells; BC, B cells; NC, neuronal cells.

Figure 4

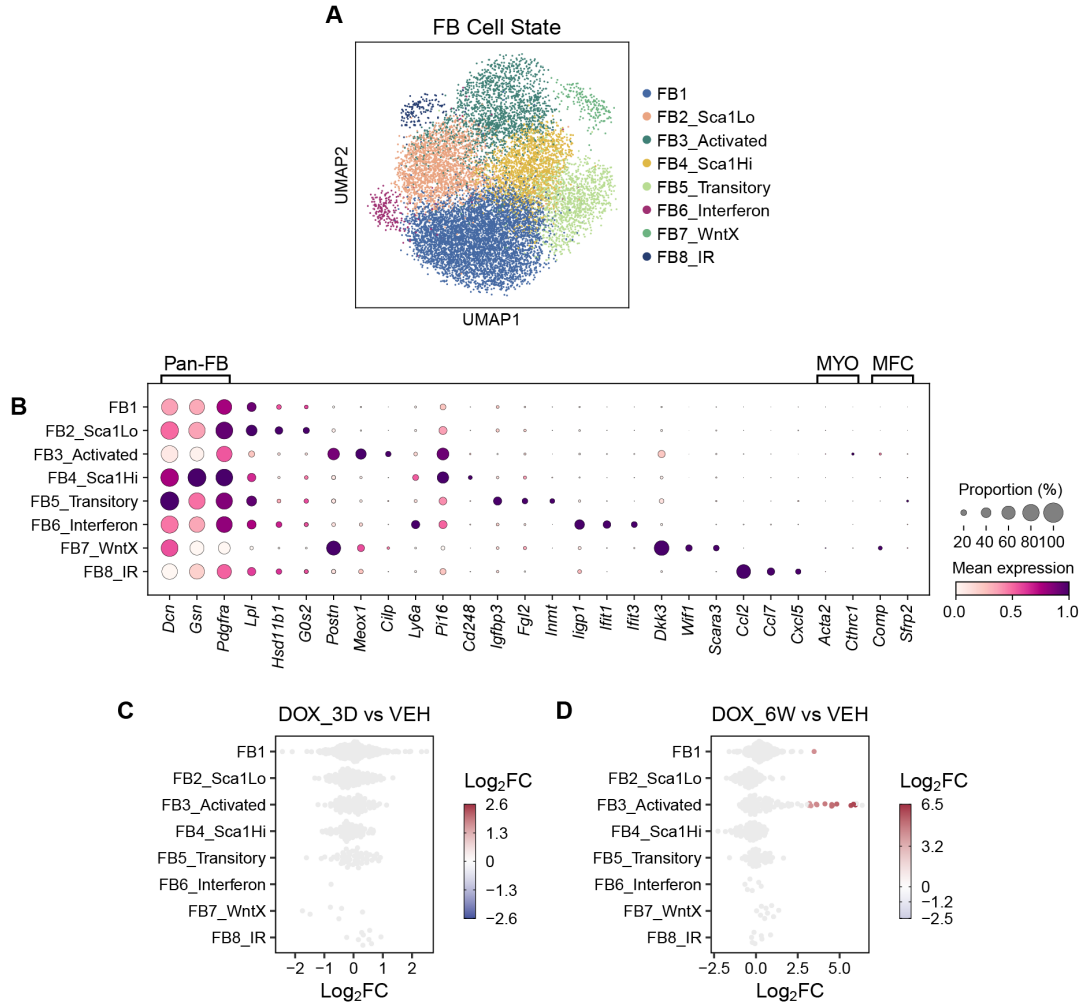

Figure 4. Doxorubicin induced expansion of an activated fibroblast subpopulation at 6-week A, UMAP representation of the fibroblast (FB) object (12,767 nuclei), colour coded by 8 FB cell states. Each point represents a single nucleus. WntX, Wnt-expressing; IR, injury response. **B**, Dot plot showing marker genes of each cell state, as well as myofibroblasts (MYO) and matrifibrocytes (MFC). Dot size represents proportion of nuclei expressing the gene in each cell state; dot colour represents scaled expression of each gene (lowest expression as 0, highest as 1). **C**-**D**, Beeswarm plots showing the distribution and enrichment of cell state-annotated Milo neighbourhoods, comparing DOX_3D versus VEH (**C**) and DOX_6W versus VEH (**D**). Each point represents a Milo neighbourhood. Colour represents Log_2 fold change (Log_2FC) of enrichment. Positive values indicate enrichment in Dox-treated groups, and negative values VEH group. Only the neighbourhoods with FDR < 0.1 (edgeR) were considered significant and coloured.

Figure 5

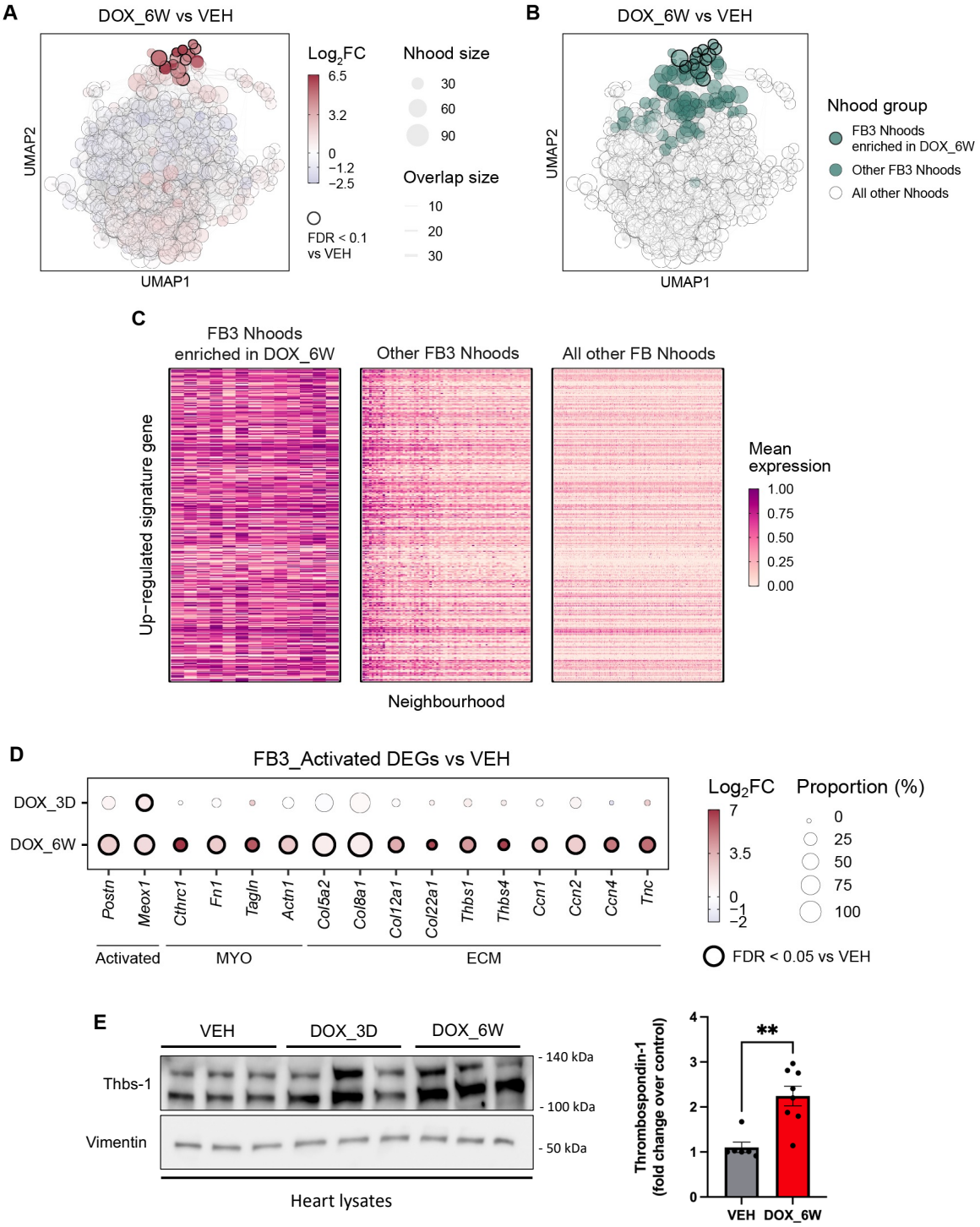
A
DOX_6W vs VEH
UMAP2
UMAP1
Log2FC
6.5
3.2
0
−1.2
−2.5
FDR < 0.1
vs VEH
Nhood size
30
60
90
Overlap size
10
20
30
B
DOX_6W vs VEH
UMAP2
UMAP1
Nhood group
FB3 Nhoods
enriched in DOX_6W
Other FB3 Nhoods
All other Nhoods
C
FB3 Nhoods
enriched in DOX_6W
Other FB3 Nhoods
All other FB Nhoods
Up−regulated signature gene
Neighbourhood
Mean
expression
1.00
0.75
0.50
0.25
0.00
D
FB3_Activated DEGs vs VEH
DOX_3D
DOX_6W
Postn
Meox1
Cthrc1
Fn1
Tagln
Actn1
Col5a2
Col8a1
Col12a1
Col22a1
Thbs1
Thbs4
Ccn1
Ccn2
Ccn4
Tnc
Activated
MYO
ECM
Log2FC
7
3.5
0
−1
−2
Proportion (%)
0
25
50
75
100
FDR < 0.05 vs VEH
E
VEH
DOX_3D
DOX_6W
Thbs-1
Vimentin
- 140 kDa
- 100 kDa
- 50 kDa
Heart lysates
Thrombospondin-1
(fold change over control)
**
VEH
DOX_6W

Figure 5. Activated fibroblast pupulation is a key player of in Doxorubicin-induced extracellular matrix remodelling A-B, UMAP representations of milo neighbourhoods (Nhoods) in the fibroblast (FB) object, comparing DOX_6W versus VEH. Each spot represents a Nhood. Spot size represents the number of nuclei in each Nhood; thickness of connection lines between Nhoods represents the number of overlapping nuclei. Those with a thick stroke are Nhoods enriched in DOX_6W (FDR < 0.1, edgeR). **A**, Spot colour represents Log_2 fold change (Log_2FC) of enrichment. Positive values indicate enrichment in the DOX_6W group, and negative values VEH group. **B**, Green-coloured spots indicate Nhoods annotated as FB3_Activated. **C**, Heatmaps showing the expression of signature genes in different groups of Nhoods. Signature genes were calculated comparing FB3 Nhoods enriched in DOX_6W to other FB3 Nhoods. Colour represents scaled expression of each gene (lowest expression as 0, highest as 1). **D**, Dot plot showing selected DEGs in FB3_Activated, separated by study groups. Dot colour represents Log_2FC of gene expression in each nucleus subset; dot size represents proportion of nuclei expressing the gene in each nucleus subset. Comparisons to the VEH group with FDR < 0.05 (edgeR) were considered significant and indicated by a thick stroke of the dot. **E**, Left, Western blotting representative image of Thbs-1 levels in whole heart lysates following DOX treatment or VEH as indicated. Vimentin was used as a loading control. Right, relative quantification of Thbs-1 levels at DOX_6W. **P<0.01 after Kolmogorov-Smirnov test comparing VEH vs DOX_6W. Thbs-1, Thrombospondin-1.

Figure 6

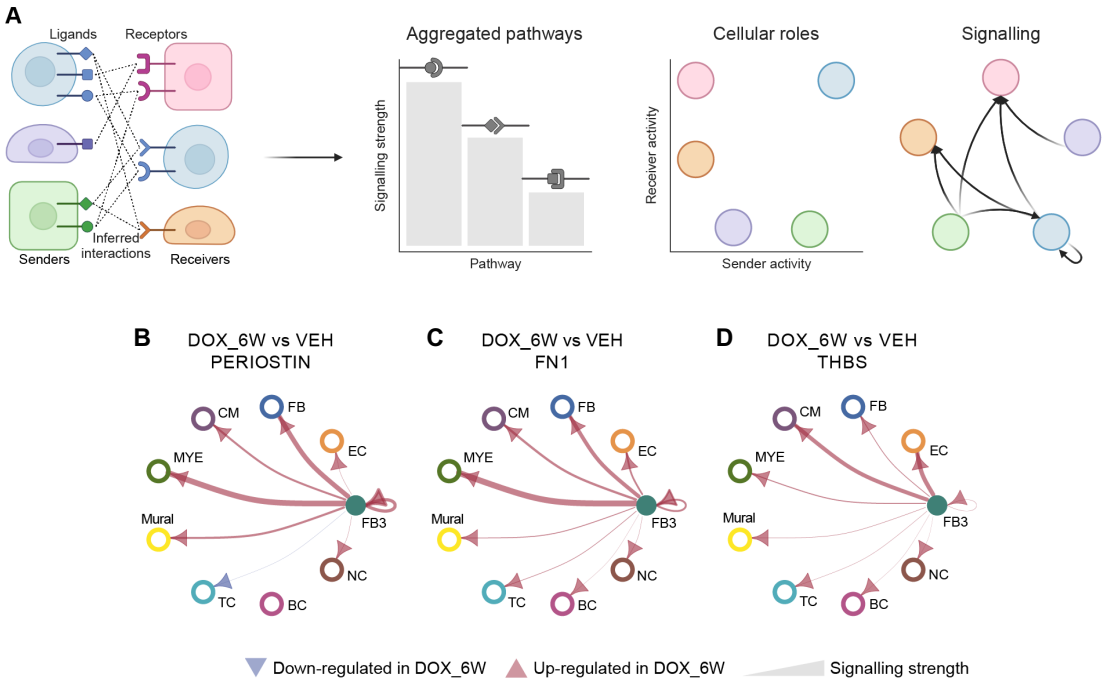

Figure 6. Activated fibroblast are mainly predicted to interact with myeloid cells and cardiomyocytes. **A,** Schematic of cell-cell interaction analysis using CellChat. Gene expression data for known ligands and receptors was obtained for each cell state to infer interactions. Ligand-receptor pairs with similar or related functions were aggregated into pathways, and signalling strength was calculated. Sender and receiver activities for each cell state were predicted based on the total expression levels of ligands and receptors, respectively. Cell-cell interactions were predicted for individual ligand-receptor pairs as well as for aggregated pathways. **B-D,** Circle plots showing differential signalling strength of the PERIOSTIN (**B**), FN1 (**C**) and THBS (**D**) pathways from FB3 to each cell type, comparing DOX_6W versus VEH. Arrow colour represents up- or down-regulation in DOX_6W; arrow thickness represents signalling strength. Solid circles represent cell state (FB3_Activated); hollow circles represent cell type.

Figure 7

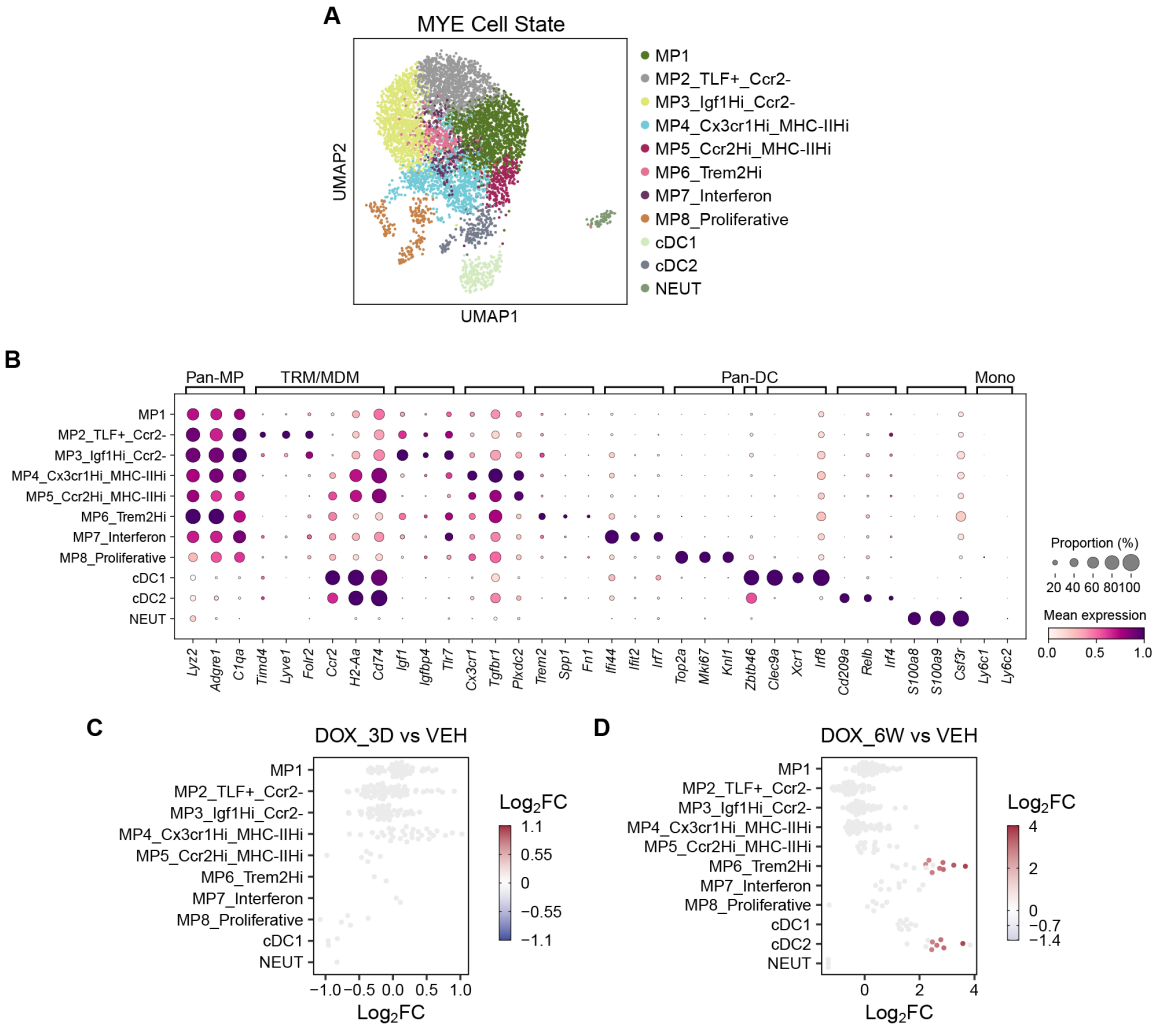

Figure 7. Doxorubicin increased the Trem2^{Hi} macrophage and type-2 conventional dendritic cell populations A, UMAP representation of the myeloid (MYE) object (5,799 nuclei), colour coded by 11 MYE cell states. Each point represents a single nucleus. MP, macrophages; TLF, *Timd4*/*Lyve1*/*Folr2*; MHC-II, major histocompatibility complex class II; cDC, conventional dendritic cells; NEUT, neutrophils. **B**, Dot plot showing marker genes of each cell state. Dot size represents proportion of nuclei expressing the gene in each cell state; dot colour represents scaled expression of each gene (lowest expression as 0, highest as 1). TRM, tissue resident macrophages; MDM, monocyte-derived macrophages; DC, dendritic cells; Mono, monocytes. **C**-**D**, Beeswarm plots showing the distribution and enrichment of cell state-annotated Milo neighbourhoods, comparing DOX_3D versus VEH (**C**) and DOX_6W versus VEH (**D**). Each point represents a Milo neighbourhood. Colour represents Log_2 fold change (Log_2FC) of enrichment. Positive values indicate enrichment in Dox-treated groups, and negative values VEH group. Only the neighbourhoods with FDR < 0.1 (edgeR) were considered significant and coloured.

Figure 8

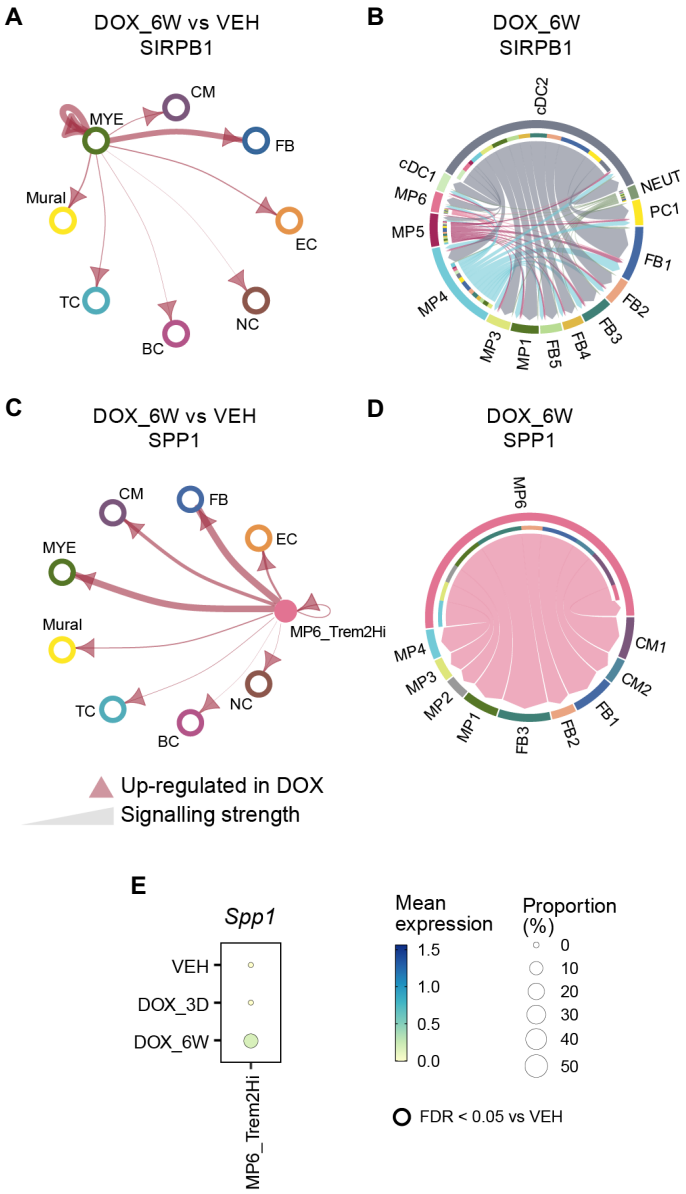

Figure 8. Trem2^{Hi} macrophage and type-2 conventional dendritic cell populations displayed activated signalling of SIRPB1 and SPP1, respectively at DOX_6W A, C Circle plots showing differential signalling strength of signal regulatory protein beta 1 (SIRPB1) (**A**) and secreted phosphoprotein 1 (SPP1, or osteopontin) (**C**) pathway across different cell groups, comparing DOX_6W versus VEH. Arrow colour (red) represents up-regulation in DOX_6W; arrow thickness represents signalling strength. Hollow circles represent cell types; solid circles represent cell state (MP6_Trem2Hi). **B**, **D**, Chord plots showing 98% of the interactions within the SIRPB1 (**B**) and SPP1 (**D**) pathway in the DOX_6W group. Arrows indicate the direction of signals; arc width corresponds to the contribution of each cell state as sender/receiver. **E**, Left Dot plots showing *Spp1* gene MP6_Trem2Hi, separated by study groups. Dot colour represents the mean Log-normalised expression of each gene; dot size represents proportion of nuclei expressing the gene in each nucleus subset. Comparisons to the VEH group with FDR < 0.05 (edgeR) were considered significant and indicated by a thick stroke of the dot.

Figure 9

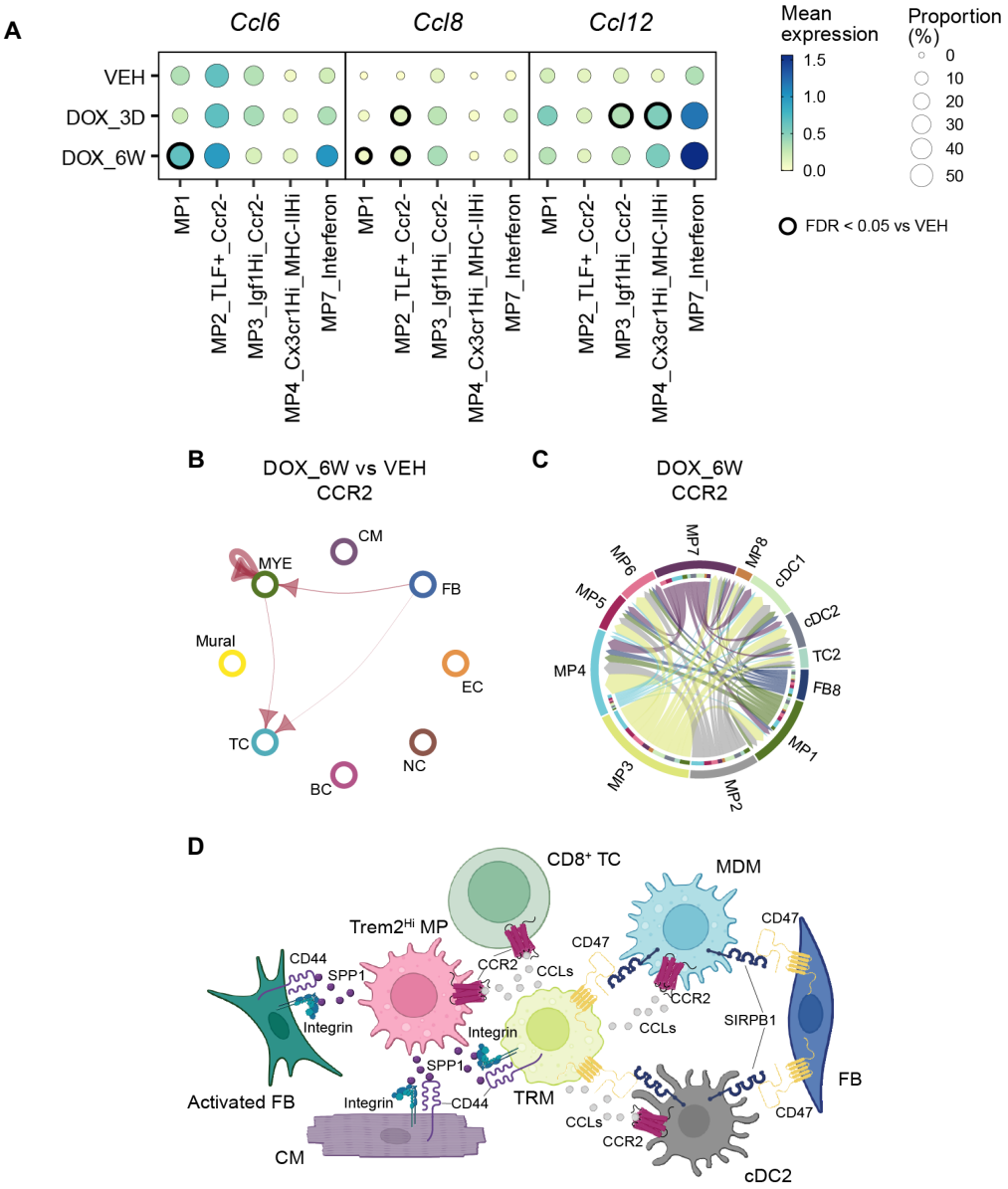

Figure 9. Doxorubicin drives complex immune response, with upregulation of pro-inflammatory signalling. A, Dot plots showing genes encoding the ligands of the CCR2 pathway in various myeloid cell states, separated by study groups. Dot colour represents the mean Log-normalised expression of each gene; dot size represents proportion of nuclei expressing the gene in each nucleus subset. Comparisons to the VEH group with FDR < 0.05 (edgeR) were considered significant and indicated by a thick stroke of the dot. **B**, Circle plots showing differential signalling strength of the C-C motif chemokine receptor 2 (CCR2) pathway across different cell groups, comparing DOX_6W versus VEH. Arrow colour (red) represents up-regulation in DOX_6W; arrow thickness represents signalling strength. Hollow circles represent cell types; solid circles represent cell state (MP6_Trem2Hi). **C,** Chord plots showing 98% of the interactions within the CCR2 pathway in the DOX_6W group. Arrows indicate the direction of signals; arc width corresponds to the contribution of each cell state as sender/receiver. **D**, Schematic of the enhanced interactions following Dox treatment within immune cells, including tissue-resident macrophages (TRM), monocyte-derived macrophages (MDM), Trem2^{Hi} macrophages (MP), conventional dendritic cells type 2 (cDC2) and CD8^{+} T cells (TC), as well as their crosstalk with other cardiac cell types, cardiomyocytes (CM), fibroblasts (FB) and activated FB. CCLs, C-C motif chemokine ligands.

Figure 10

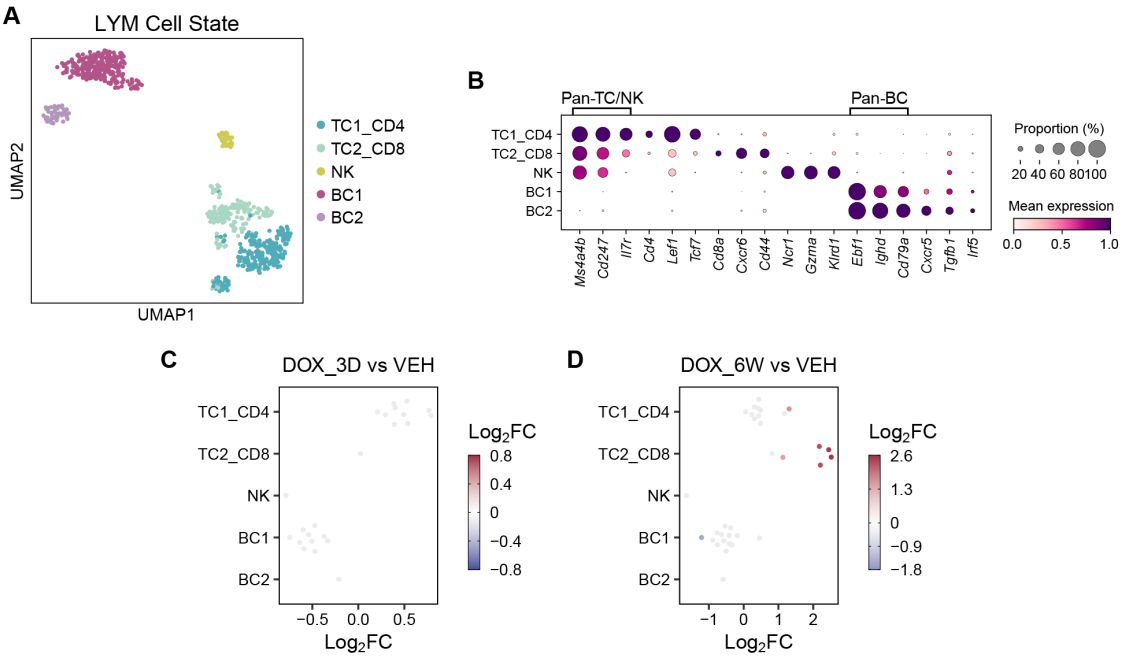

Figure 10 Doxorubicin induced the expansion of CD8⁺ T cells A, UMAP representation of the lymphoid (LYM) object (803 nuclei), colour coded by 5 LYM cell states. Each point represents a single nucleus. TC, T cells; NK, natural killer cells; BC, B cells. **B**, Dot plot showing marker genes of each cell state. Dot size represents proportion of nuclei expressing the gene in each cell state; dot colour represents scaled expression of each gene (lowest expression as 0, highest as 1). **C**-**D**, Beeswarm plots showing the distribution and enrichment of cell state-annotated Milo neighbourhoods, comparing DOX_3D versus VEH (**C**) and DOX_6W versus VEH (**D**). Each point represents a Milo neighbourhood. Colour represents Log_2 fold change (Log_2FC) of enrichment. Positive values indicate enrichment in Dox-treated groups, and negative values VEH group. Only the neighbourhoods with FDR < 0.1 (edgeR) were considered significant and coloured.

Figure 11

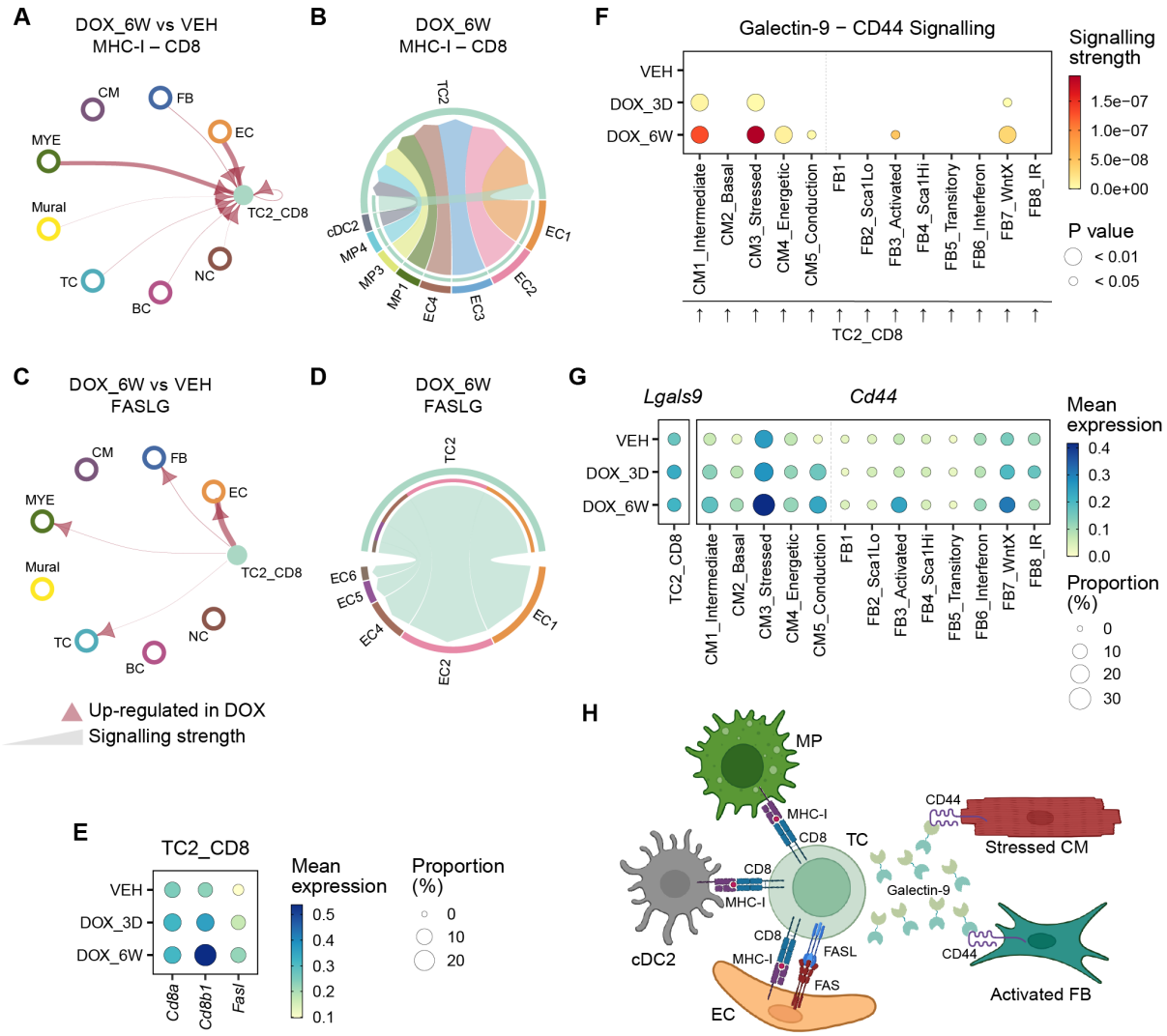

Figure 11 CD8⁺ T cells predicted to interacted with various cardiac cell types following Doxorubicin treatment A, **C**, Circle plots showing differential signalling strength of the major histocompatibility complex class I (MHC-I) – CD8 (**A**) and Fas ligand (FASLG) (**C**) pathway between TC2_CD8 and other cell types, comparing DOX_6W versus VEH. Arrow colour (red) represents up-regulation in DOX_6W; arrow thickness represents signalling strength. **B**, **D**, Chord plots showing 98% of the interactions within the MHC-I – CD8 (**B**) and FASLG (D) pathway in the DOX_6W group. Arrows indicate the direction of signals; arc width corresponds to the contribution of each cell state as sender/receiver. **E**, Dot plot showing selected genes encoding receptors or ligands in TC2_CD8, separated by study groups. Dot colour represents the mean Log-normalised expression of each gene; dot size represents proportion of nuclei expressing the gene in each nucleus subset. **F**, Dot plot showing Galectin9 – CD44 signalling from TC2_CD8 to cardiomyocytes or to fibroblasts. Dot colour represents signalling strength of each interaction; dot size represents P value. Only signals with P value < 0.05 were shown. **G**, Dot plot showing *Lgals9* expression in TC2_CD8 and *Cd44* expression in cardiomyocytes and fibroblasts, separated by study groups. Dot colour represents the mean Log-normalised expression of each gene; dot size represents proportion of nuclei expressing the gene in each nucleus subset. **H**, Schematic showing the increased interaction of CD8⁺ T cells (TC) following Dox treatment with other cardiac cell types, including macrophages (MP), conventional dendritic cells type 2 (cDC2), endothelial cells (EC), stressed cardiomyocytes (CM) and activated fibroblasts (FB).

Figure 12

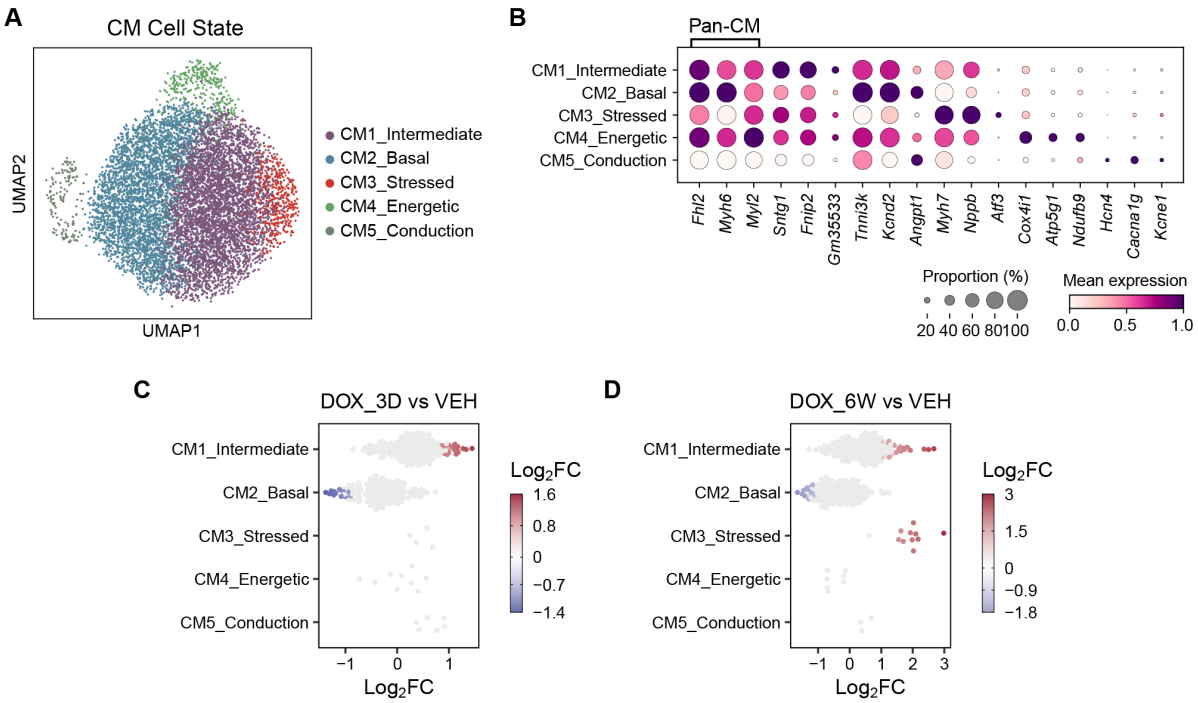

Figure 12 Doxorubicin up-regulated stressed cardiomyocyte populations A, UMAP representation of the cardiomyocyte (CM) object (8,940 nuclei), colour coded by 5 CM cell states. Each point represents a single nucleus. **B**, Dot plot showing marker genes of each cell state. Dot size represents proportion of nuclei expressing the gene in each cell state; dot colour represents scaled expression of each gene (lowest expression as 0, highest as 1). **C-D**, Beeswarm plots showing the distribution and enrichment of cell state-annotated Milo neighbourhoods, comparing DOX_3D versus VEH (**C**) and DOX_6W versus VEH (**D**). Each point represents a Milo neighbourhood. Colour represents Log_2 fold change (Log_2FC) of enrichment. Positive values indicate enrichment in Dox-treated groups, and negative values VEH group. Only the neighbourhoods with FDR < 0.1 (edgeR) were considered significant and coloured

Figure 13

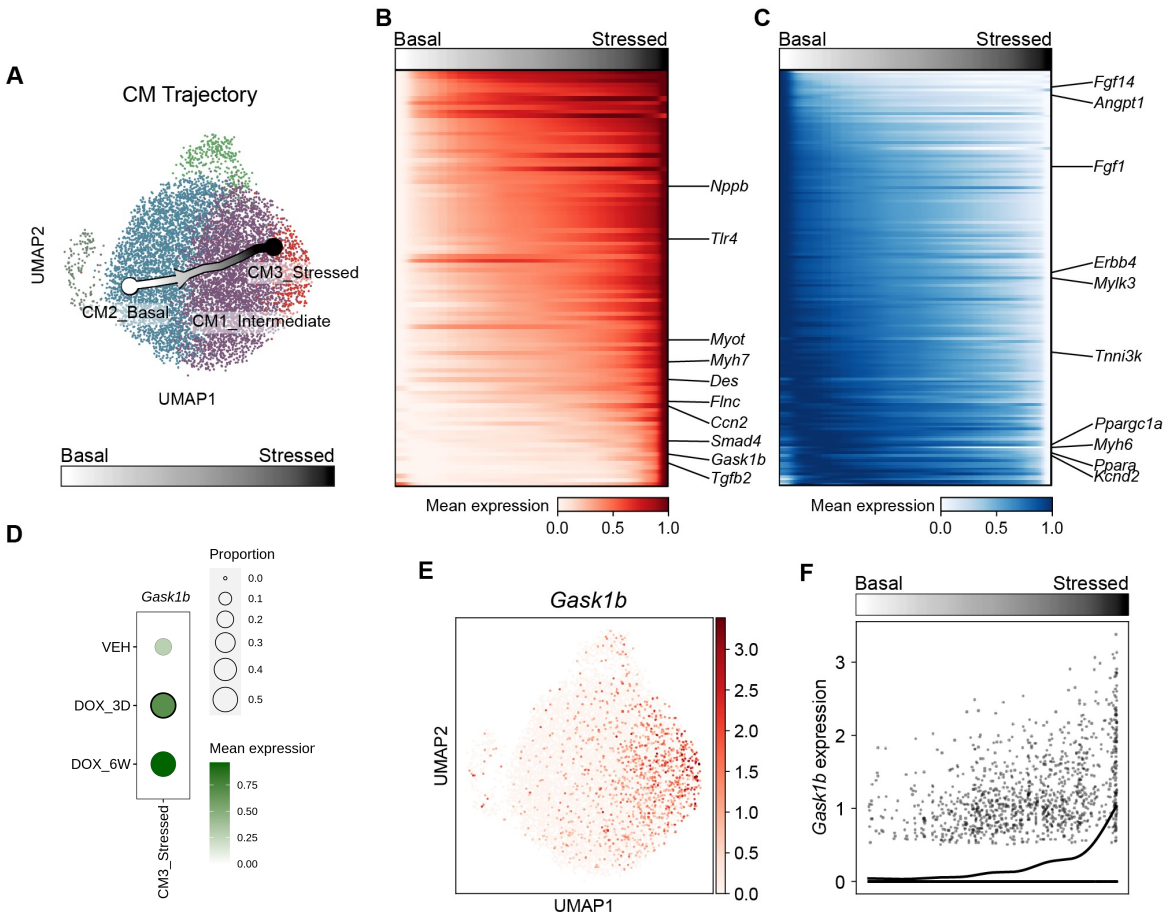

Figure 13 Trajectory analysis highlighted a Basal-to-stressed continuum within cardiomyocytes, with Gask1b upregulation within stressed cardiomyocytes **A**, UMAP representation of the cardiomyocyte (CM) object with inferred trajectory indicating Basal-to-Stressed CM continuum. **B-C**, Heatmaps showing the expression of signature genes along the Basal-to-Stressed trajectory. Colour represents scaled expression of each gene (lowest expression as 0, highest as 1). **D**, Upset plot showing number of unique and shared genes between marker genes of CM1_Intermediate, CM2_Basal and CM3_Stressed, and signature genes with increased or decreased expression along the trajectory. Bracketed numbers are number of genes in each set; dots with connection lines represent the corresponding intersection of gene sets; single dots represent sets with unique genes; bar plot and the above numbers are number of shared or unique genes. **E**, UMAP representation of *Gask1b* expression. Colour represents Log-normalised expression. **F**, Scatter plot and a fitted curve showing *Gask1b* expression along the trajectory. Each point represents a single nucleus.

Figure 14

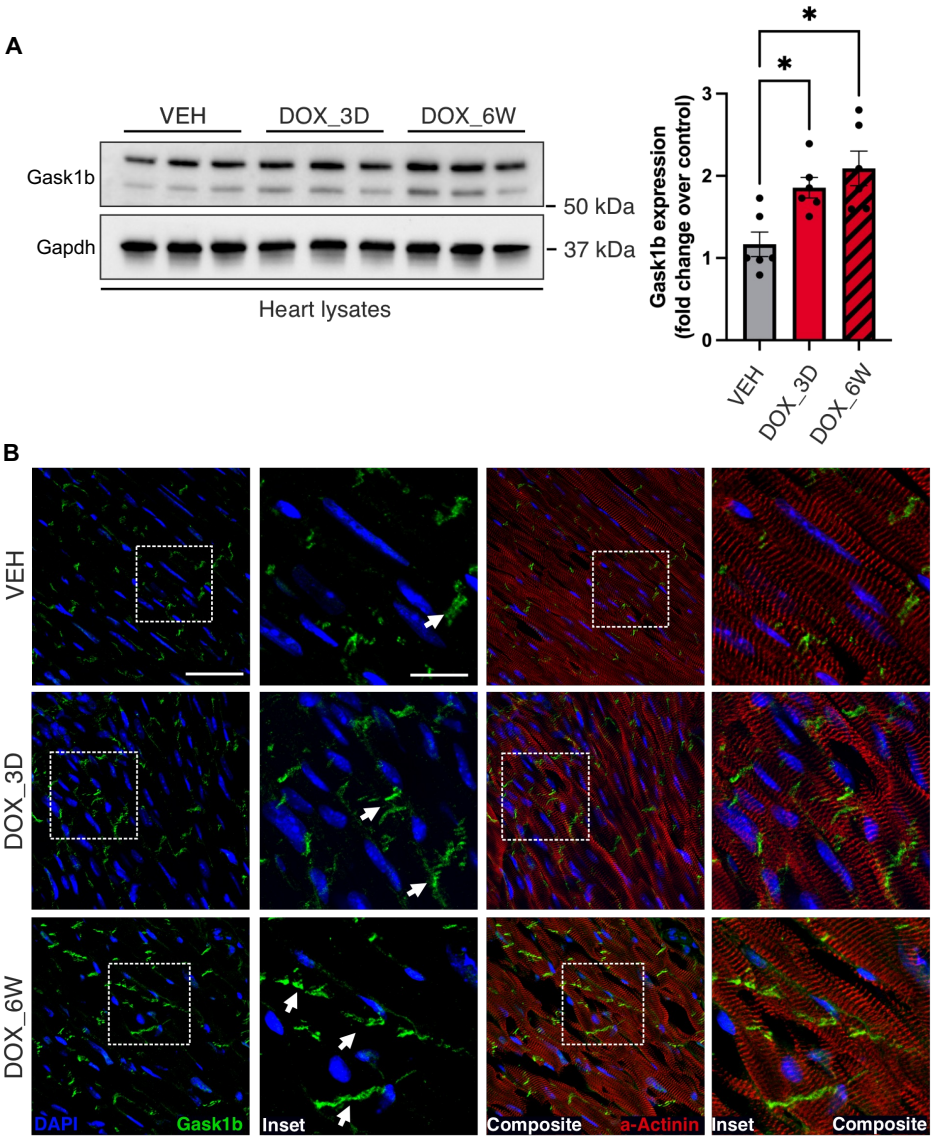

Figure 14 Gask1b is upregulated at protein level upon doxorubicin treatment A, Left, Western blotting representative image of Gask1b levels in whole heart lysates following DOX treatment or VEH as indicated. Gapdh was used as a loading control. Right, relative quantification of Gask1b levels among treatment groups. *P<0.05, Kruskal-Wallis rank test with Dunn's test for multiple comparisons. **B**, Representative immunofluorescence images of mouse heart tissue treated as indicated and stained for Gask1b and α-Actinin. Nuclei were counterstained with DAPI. Scale bar = 20 μm.

Figure 15

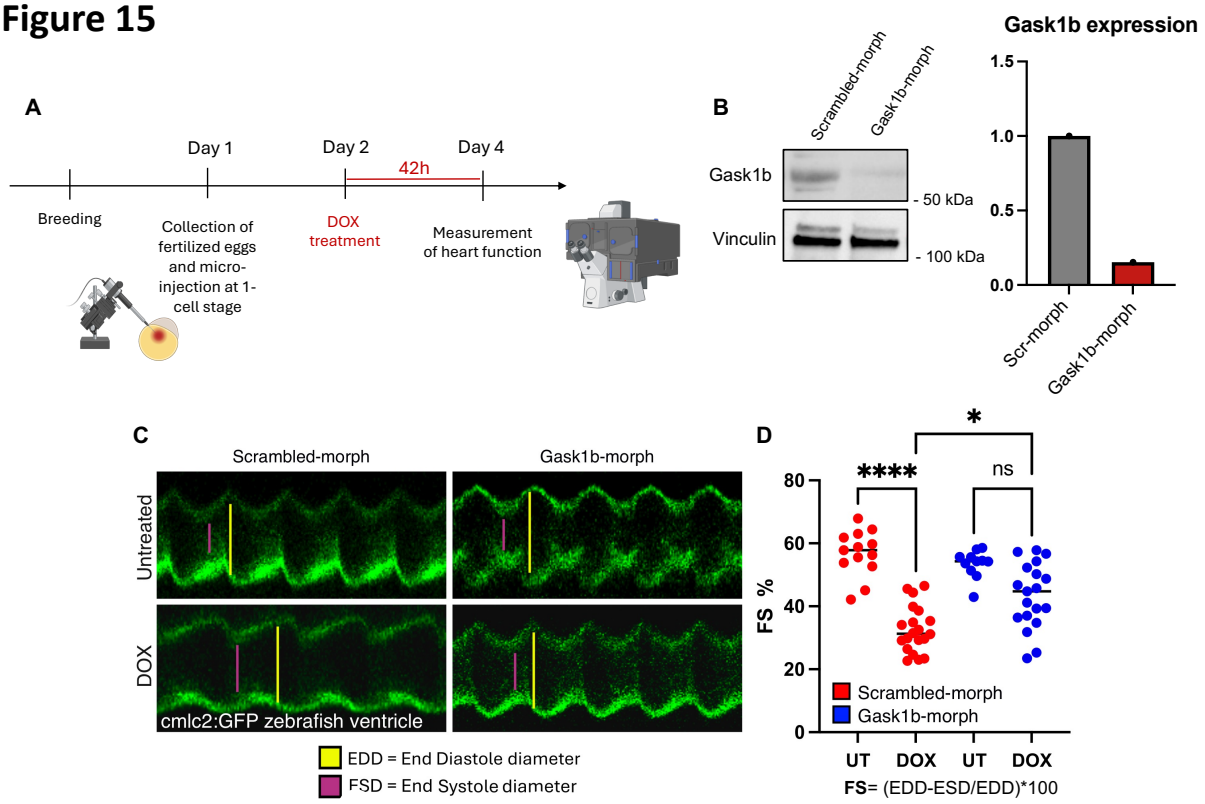

Figure 15 Gask1b silencing partially prevents DOX-induced cardiac dysfunction and DNA damage in zebrafish A, Schematic of the workflow. Briefly, Zebrafish embryos were injected at the 1-cell stage with either scrambled morpholino (Scr-morph) or anti-Gask1b morpholino (Gask1b-morph). After 24 hours, zebrafish larvae were treated with DOX 40 uM for 42 hours before acquisition of contracting hearts. **B**, Representative immunoblot of Gask1b and Vinculin from zebrafish larvae injected with either scrambled morpholino (Scr-morph) or anti-Gask1b morpholino (Gask1b-morph). **C**, Representatitve M-mode of contracting ventricular walls of cmlc2:GFP zebrafish treated as indicated. Heart function was assessed by measuring EED and ESD to calculate fractional shortening (FS). Briefly, M-mode images were constructed from sequential frames along a fixed scan line using ImageJ software. Ventricular dimensions were measured at the endocardial borders during end systole and end diastole, and FS was then calculated from these measurements. **D**, FS measurements in zebrafish larvae upon DOX exposure. Each dot corresponds to one single zebrafish larva. Data pooled from N=4 separate experiments. **E**) Representative immunoblot of γH2A.X and Gapdh from zebrafish larvae injected with either scrambled morpholino (Scr-morph) or anti-Gask1b morpholino (Gask1b-morph). **** P<0.001, *P<0.05 by one-way ANOVA followed by Bonferroni post-hoc correction.

Figure 16

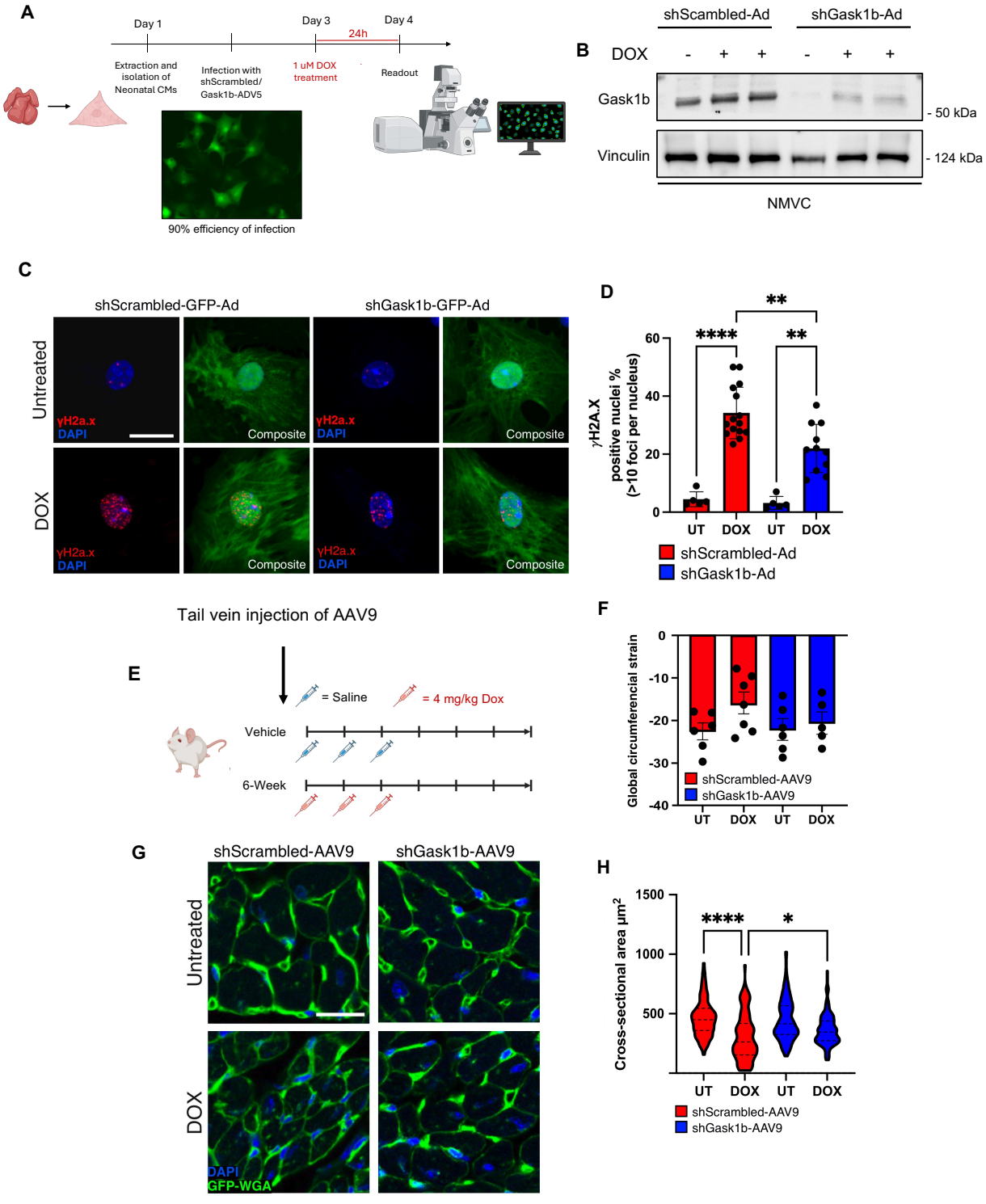
A
Day 1
Day 3
Day 4
24h
Extraction and isolation of Neonatal CMs
Infection with shScrambled/ Gask1b-ADV5
1 uM DOX treatment
Readout
90% efficiency of infection
B
shScambled-Ad
shGask1b-Ad
DOX
Gask1b
Vinculin
- 50 kDa
- 124 kDa
NMVC
C
shScrambled-GFP-Ad
shGask1b-GFP-Ad
Untreated
DOX
γH2a.x
DAPI
Composite
D
γH2A.X positive nuclei % (>10 foci per nucleus)
UT
DOX
shScrambled-Ad
shGask1b-Ad
E
Tail vein injection of AAV9
= Saline
= 4 mg/kg Dox
Vehicle
6-Week
F
Global circumferencial strain
shScrambled-AAV9
shGask1b-AAV9
G
shScrambled-AAV9
shGask1b-AAV9
Untreated
DOX
DAPI
GFP-WGA
H
Cross-sectional area µm²

Figure 16 Gask1b silencing partially prevents DOX-induced DNA damage and atrophy in mice A, Schematic of the workflow. Briefly, 24 hours after extraction, NMVCs were infected with GFP-adenovirus carrying either a control scrambled shRNA (shScrambled-Ad) or Gask1b shRNA (shGask1b-Ad) as indicated and left with infection medium for 48 hours to allow efficient gene silencing. Cells were then treated with DOX 1 uM for 24 hours, fixed and stained with anti γH2A.X. **B**, Representative immunoblot of Gask1b and Vinculin from NMVCs infected with shScrambled-Ad or shGask1b-Ad and treated as indicated **C**) Confocal Immunofluorescence staining of γH2A.X in NMVCs infected with both shScrambled-ADV5 (control) and shGask1b-ADV5 and treated as indicated. Briefly, 24 hours after extraction, NMVCs were infected with GFP-adenovirus carrying either a control scrambled shRNA or Gask1b shRNA (as indicated) and left with infection medium for 48 hours to allow efficient gene silencing. Cells were then treated with DOX 1 uM for 24 hours fixed and stained with anti γH2A.X. **D,** Relative quantification of proportion of γH2A.X positive nuclei. **E,** Schematic representation of the experimental workflow. Female Balb/c mice were injected with 5×10^{11} adeno-associated viral particles (AAV9) carrying either a control shRNA (shScrambled-AAV9) or an anti-Gask1b shRNA (shGask1b-AAV9). Following AAV9 administration, mice underwent the same doxorubicin (DOX) treatment regimen as used for transcriptomic analysis. To assess cardiac function, strain imaging echocardiography was performed prior to heart tissue collection. **F**,Global Circumferential Strain (GCS) measurement in mice injected and treated as described.**G**, Confocal immunofluorescence on heart sections from the mid-portion of the ventricles of vehicle- vs. DOX-treated shGask1b-AAV9 or control mice, stained with Alexa Fluor-488-conjugated wheat germ agglutinin (WGA). The nuclei were counterstained with 40,6-Diamidino-2-Phenylindole (DAPI). Images were used to calculate the cardiomyocyte cross-sectional areas (**H**). **** P<0.001, **P<0.01, *P<0.05 by one-way ANOVA followed by Bonferroni post-hoc correction.

Figure 17

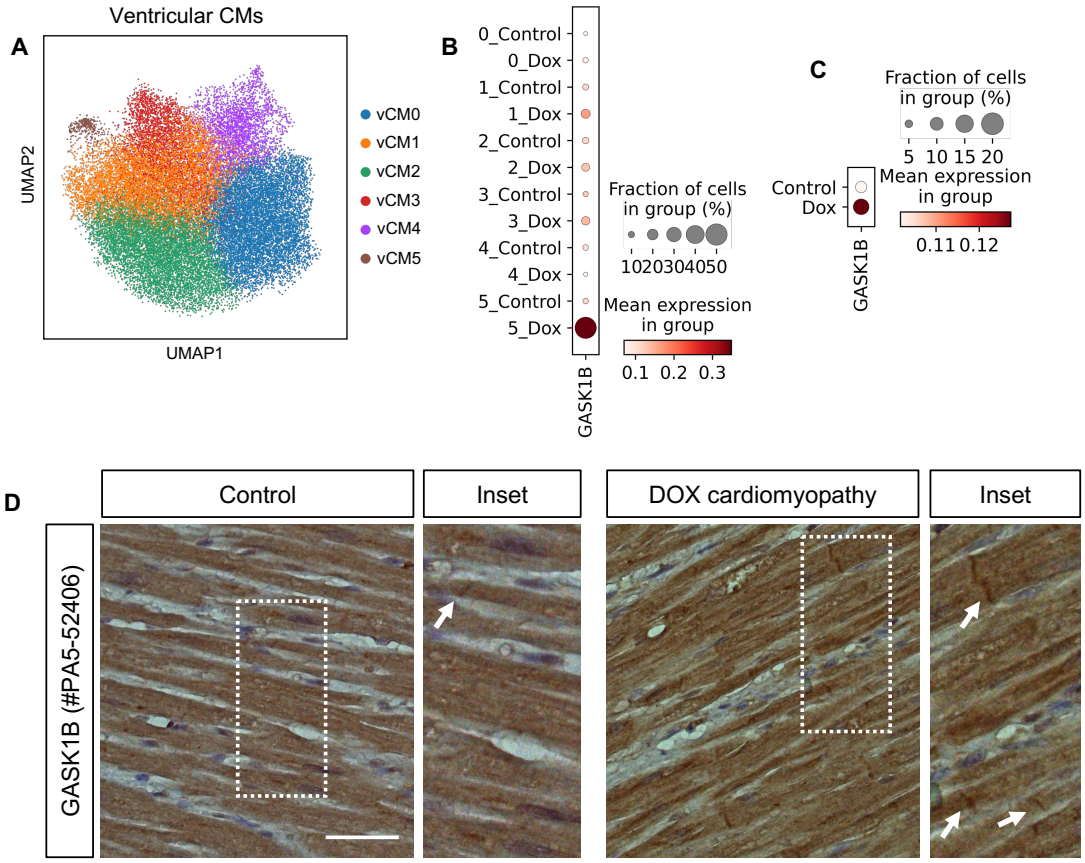

***GASK1B* is upregulated in doxorubicin-treated human hearts A,** UMAP representation of unbiased subclustering of human heart ventricular cardiomyocytes (vCM) from both control and DOX-treated hearts colour-coded by cell states. **B,** Dotplot showing the expression of Gask1b across vCM subclusters. **C,** Dotplot showing the overall expression of Gask1b in vCM between DOX and Control patients. **D,** PI3Kγ staining in human heart sections from a healthy donor (left) and a patient who developed cardiomyopathy after DOX treatment (right). Enlargements of the outlined areas (right). Scale bar, 50 µm.

Figure 18

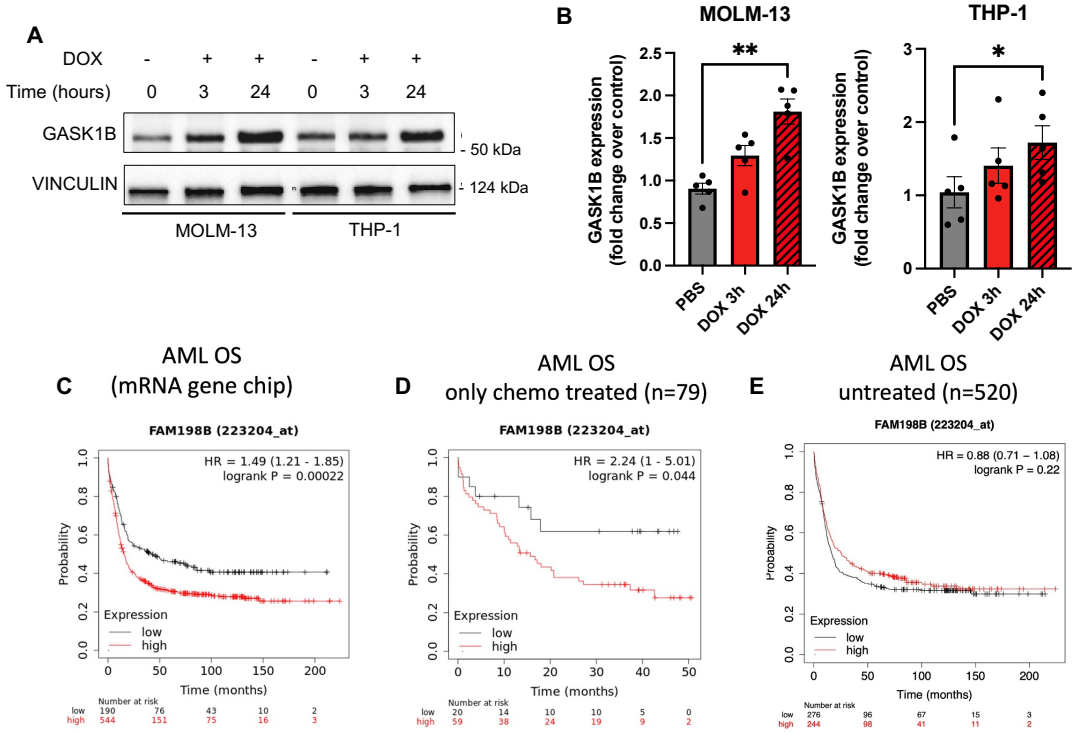

Figure 18 *GASK1B* upregulation correlates with lower survival in Acute Myeloid Leukemia (AML) A, Left, Western blotting representative image of Gask1b levels in AML cell lines (MOLM-13; THP1) following DOX treatment or VEH as indicated. Vinculin was used as a loading control. **B**, Relative quantification of Gask1b levels in AML cell lines. *P<0.05;**P<0.01, Kruskal-Wallis rank test with Dunn's test for multiple comparisons. **C-D-E,** Kaplan-Meier analysis of the overall survival (OS) of patients with AML (GSE1159, GSE12417, GSE37642; GSE6891) and their expression of GASK1B. FAM198B, alias for GASK1B.

Part II

Enhancing CFTR Modulator Therapy in Cystic Fibrosis: Stabilization of F508del-CFTR by Targeting the A-Kinase Anchoring function of PI3Kγ

ABSTRACT

Background

Cystic fibrosis (CF), characterized by airway mucus obstruction and chronic inflammation, is caused by mutations in the gene encoding the cystic fibrosis transmembrane conductance regulator (CFTR), a plasma membrane (PM) cAMP-activated Cl- channel. The most frequent mutation in CF patients (F508del-CFTR) results in trafficking defect and decreased stability of the channel, which is retained in the endoplasmic reticulum (ER) and degraded before targeting the plasma membrane (PM). ETI therapy, the standard of care for patients carrying the F508del-CFTR, combines two correctors (Tezacator [VX-661] and Elexacaftor [VX-445]) with the potentiator Ivacaftor [VX-770] to correct folding and improve gating of the mutant CFTR channel. While it improves lung function by 9.8% in F508del heterozygous patients after 6 months, ETI restores only partially the activity and stability of the CFTR channel. As a result, patients still experience mucus dysfunction, airway infection, and inflammation, emphasizing the need for improved treatment strategies.

Aims

Since boosting cAMP/PKA signaling is known to promote PM CFTR stabilization and enhance CFTR modulator activity, we hypothesized that the cAMP-elevating peptide we previously developed (PI3Kγ MP; Patent n° WO/2016/103176) could be exploited to enhance F508del-CFTR PM density and stability, thus increasing the therapeutic effect of ETI therapy.

Methods

Cell surface protein biotinylation followed by western blotting and immunogold electron microscopy were used to evaluate CFTR PM density in HEK293T, 16HBE14o- and CFBE41o- cell lines upon PI3Kγ MP treatment. Phosphoproteomics was exploited to unravel potential targets activated by PI3Kγ MP.

Results

We confirmed that combining PI3Kγ MP with ETI maximizes ETI's therapeutic efficacy in CFBE41o- cells expressing F508del-CFTR by increasing plasma membrane density compared to ETI alone. Moreover, after 6 hours of cycloheximide (CHX) treatment, 30% of ETI-rescued F508del-CFTR remained undegraded, while 67% persisted with the addition of PI3Kγ MP, indicating that PI3Kγ MP doubles the stability of corrected F508del-CFTR. To confirm the relevance of our CFBE results, we tested PI3Kγ MP with ETI in primary HBE cells, showing a 25% increase in CFTR activity compared to ETI alone, supporting its potential as an add-on therapy for F508del CF patients. To fully unravel the underlying molecular mechanism, we took advantage of an unbiased approach based on phosphoproteomics, which revealed protein kinase D1 (PKD1), a well-established orchestrator of protein trafficking, as being strongly activated by PI3Kγ MP. Interestingly, PI3Kγ MP failed to promote F508del-CFTR stabilization at the PM after PKD1 inhibition, thus revealing PKD1 as the key mediator of the effect of PI3Kγ MP. Intriguingly, we found that PKD1 activation is driven by the coordinated actions of PKA and PKC, regulated by A-kinase anchoring protein 13 (AKAP13/AKAP-Lbc). Our findings suggest that both PKD1 and AKAP13 are novel contributors to the CFTR signaling network, highlighting their roles in CFTR regulation.

Conclusions

This study identifies PI3Kγ and PKD1 as pivotal regulators of CFTR stability at the PM and suggests exploiting the ability of PI3Kγ MP to increase F508del-CFTR PM trafficking and ETI therapeutic effect.

1. INTRODUCTION

Cystic fibrosis is the most common life-threatening inherited disorder among the Caucasian population. It is caused by mutations in the cystic fibrosis transmembrane conductance regulator (*CFTR*) gene, which encodes a cyclic adenosine monophosphate (cAMP)-activated anion channel expressed on the surface of epithelial cells that regulates mucus hydration and clearance (Grasemann and Ratjen 2023, Mall et al., 2024). CFTR dysfunction leads to impaired Cl^- and water secretion across the airway epithelium, producing a viscous mucus that traps pathogens causing chronic infections and inflammation (Ong and Ramsey, 2023}. These complications are responsible for a progressive decline in airway function, ultimately leading to respiratory failure (Shteinberg et al., 2023).

In the USA, about 85% of people with CF (pwCF) carry at least one copy of the F508del allele, resulting in a mutant CFTR channel known as F508del-CFTR, which is characterized by defective folding, impaired gating, and reduced stability at the plasma membrane (Grasemann and Ratjen 2023) The standard of care for F508del patients is ETI therapy, a combination of two “correctors”, namely Tezacator (VX-661) and Elexacaftor (VX-445), and the “potentiator” Ivacaftor (VX-770), which corrects the folding and improve the gating of the mutant channel, respectively. Despite the high clinical efficacy, with an average lung function improvement of 9.8% in F508del heterozygous patients after a 6-month treatment (Nichols et al., 2022), ETI therapy only restores F508del-CFTR activity up to only 50% of that of the wild-type channel (Graeber et al., 2022). As a result, pwCF on ETI therapy continue to experience residual mucus dysfunction, airway infection, and inflammation (Casey et al 2023, Schaupp et al. 2023, Nichols et., 2022) underscoring the need for strategies to enhance treatment efficacy.

Boosting cAMP signaling has been reported to maximize the efficacy of CFTR modulators (Graeber et al., 2023). On the one hand, an increase in cAMP activates PKA, leading to the phosphorylation of the channel, which is essential for the optimal efficacy of the potentiator VX-770 (Ghigo et al., 2022). Additionally, cAMP can boost the effectiveness of correctors like Lumacaftor (VX-809) in rescuing F508del-CFTR by reducing channel endocytosis (Lobo et al., 2016). Mechanistically, this involves the exchange protein directly activated by cAMP (EPAC1) that, upon cAMP activation, translocates to the plasma membrane. Here, through NHERF1, EPAC1 interacts with ezrin (Loureiro et al., 2015), an actin filament-binding protein that finally favors the anchoring of the CFTR channel to the actin cytoskeleton (Lobo et al., 2016). Hence, agents that elevate cAMP near the CFTR channel may act as CFTR “stabilizers”. By prolonging the residence time of F508del-CFTR at the plasma membrane, these agents could ultimately enhance the efficacy of CFTR modulator therapies, like ETI (Lopes-Pacheco, 2019)

Our previous research demonstrated that a physiological and compartment-restricted increase in cAMP near the CFTR can be achieved by targeting the A-kinase-anchoring protein (AKAP) function of phosphoinositide 3-kinase γ (PI3Kγ) (Ghigo et al., 2022). We showed that a PI3Kγ mimetic peptide (PI3Kγ MP) that disrupts the interaction between PI3Kγ and PKA inhibits a pool of the cAMP-hydrolyzing enzymes PDE4 that restricts PKA-mediated phosphorylation and gating of the channel. Accordingly, PI3Kγ MP promoted the gating of wild-type (wt) CFTR and augmented the efficacy of the VX-770

potentiator in rescuing the function of F508del-CFTR. However, the role of the PI3Kγ/PKA signalosome in regulating CFTR membrane stability remained unexplored.

Herein, we demonstrate that targeting the AKAP function of PI3Kγ with PI3Kγ MP increased the abundance of pharmacologically-corrected F508del-CFTR at the plasma membrane, eventually augmenting the efficacy of ETI therapy in primary human bronchial epithealial cells (HBEs). This effect is achieved by extending the residence time of the channel at the cell surface, rather than by promoting the maturation of F508del-CFTR. This distinction indicates that PI3Kγ MP acts as a CFTR stabilizer rather than a corrector. Importantly, the stabilizing effect of PI3Kγ MP is abolished when protein kinase D1 (PKD1) is inhibited. PKD1, an enzyme involved in membrane protein trafficking and actin cytoskeleton reorganization, is phosphorylated and activated upon PI3Kγ MP treatment. This activation results from the coordinated action of PKA and protein kinase C (PKC), orchestrated by A-kinase anchoring protein 13 (AKAP13/AKAP-Lbc). AKAP13, a guanine nucleotide exchange factor (GEF) that regulates cytoskeletal dynamics, forms and coordinates a molecular complex in response to a peptide-induced rise in cAMP. This process uncovers a novel mechanism by which PI3Kγ MP enhances CFTR stability at the membrane.

2. MATERIALS AND METHODS

Antibodies, plasmids, shRNA, peptides and reagents

Antibodies: the Anti-CFTR antibody A2-570 was kindly provided by J. R. Riordan (University of North Carolina at Chapel Hill) via the CFTR Antibody Distribution Program of the Cystic Fibrosis Foundation. The anti-Phospho-Ser/Thr-PKA substrate (9621S), anti-PKD/PKCμ (90039), anti-Tubulin (2144), and anti-Vinculin (4650) antibodies were purchased from Cell Signaling Technology. The anti-Phospho-Ser910 of PKC mu (PA538388), and the anti-Ser744, Ser748 Phospho-PDK/PKC mu (PA5110148) antibodies were purchased from Invitrogen. The anti-GORASP2/GRASP55 (ab211531) antibody was purchased from Abcam. The anti-GAPDH (sc-3223) antibody was purchased from Santa Cruz Biotechnology. The anti-Flag® M2 (F1804), anti-GFP (G1544), anti-Mouse IgG (12-371), and anti-Rabbit IgG (12-370) antibodies were purchased from Sigma. The anti-HA Tag Monoclonal Antibody (26183) was purchased from Invitrogen.

Drugs: Elexacaftor (VX-445), Tezacaftor (VX-661), Ivacaftor (VX-770), Go 6983, and L Glutathione reduced were purchased from MedChemExpress. Lumacaftor (VX-809) was purchased from Selleckchem. Dimethyl sulfoxide (DMSO), CRT0066101 hydrochloride, Cycloheximide (CHX) solution (C4859), Poly-L-arginine hydrochloride (P4663), Forskolin, Amiloride, pCPT-cAMP, CFTRinh-172, UTP, and 8-Br-cAMP were purchased from Merck. Cilostamide (PDE3i) and Ro 20-1724 (PDE4i) were purchased from Bio-Techne.

Other Reagents: siGRASP55 was purchased from Dharmacon. H89 dihydrochloride, and ESI 09 were purchased from Bio-Techne. Endoglycosidase H (Endo H) was purchased from New England Biolabs.

Pierce™ High Capacity Streptavidin Agarose, and EZ-Link™ Sulfo-NHS-SS-Biotin were purchased from Thermo Scientific™. Penentratin-1 (CP: RQIKIWFQNRRMKWKK), and the PI3Kγ-mimetic peptide (PI3Kγ MP: RQIKIWFQNRRMKWKKGKATHRSPGQIHLVQRHPPSEESQAF) were synthesized by GenScript (Piscataway, NJ).

Plasmids: The pEGFP-C1 plasmids expressing wild-type (wt-CFTR-GFP) and the F508del mutant CFTR (F508del-CFTR-GFP) were kind gifts from P. Haggie (University of California San Francisco). Flag-PKD1 plasmid was purchased from VectorBuilder. The GFP-AKAP-Lbc and the GFP-AKAP-Lbc PH domain plasmids were described previously (Carnegie et al., 2004). The STX5-HA plasmid was a kind gift from Prof. Ming Goo Lee (Yonsei University College of Medicine).

Cell lines and transfection

Immortalized cystic fibrosis human bronchial epithelial (CFBE41o-) cells stably expressing the F508del-CFTR (F508del-CFBE41o-) were kindly provided by L. Fu from the UAB Research Foundation (Birmingham, AL). Cells were cultured in minimum essential medium (MEM) (#21090022; Gibco) supplemented with 10% FBS (#10270106; Gibco), 2% L-glutamine (#25030024; Gibco), 100 U/ml penicillin and 100 µg/ml streptomycin (15140122; Gibco), and 3 µg/ul puromycin (#A1113803; Gibco) on culture dishes pre-coated with 1 mg/ml human fibronectin (F0895; Sigma-Aldrich), 3 mg/ml bovine collagen I (C4243; Sigma-Aldrich) and 0.1% bovine serum albumin (A9418; Sigma-Aldrich). Human embryonic kidney 293T (HEK293T) (American Type Culture Collection; catalog number CRL-3216) cells were cultured in DMEM (#61965026; Gibco) supplemented with 10% FBS (#10270106; Gibco) and 100 U/ml penicillin and 100 µg/ml streptomycin (#15140122; Gibco). Cells were transfected with the indicated plasmids (up to 10 µg of total cDNA) with either calcium phosphate or the X-tremeGENE™ HP DNA transfection reagent (#6366244001; Roche) and used for experiments 24 hours after transfection. All cells were cultured at 37°C and under a 5% CO_2 atmosphere.

Protein extraction and immunoprecipitation

CFBE41o- and HEK293T cells were scraped in 120 mmol/L NaCl, 50 mmol/L Tris-HCl (pH 8.0), and 1% Triton X-100, supplemented with proteases (Roche), and phosphatase inhibitors (10 mM $Na_4P_2O_7$; 10 mM NaF; 2 mM Na_3VO_4), as described above. Detergent-insoluble material was precipitated by centrifugation at 13000 rpm for 10 min at 4°C. Supernatants were subjected to immunoprecipitation or used directly for Western blotting. For immunoprecipitation assays, pre-cleared extracts were incubated with 30 µl of a 2:1 slurry of protein G-Sepharose (Amersham Biosciences) and 1-2 ug of antibody/mg of protein for 2 hours at 4°C. Immunocomplexes were then extensively washed with lysis buffer and used for western blotting.

Cell surface biotinylation assay

Cells were washed twice with ice-cold PBS (pH=8.0) and incubated with 0.5 mg/ml Sulfo NHS-SS-biotin (Thermo Fisher Scientific) in PBS (pH=8.0) for 1 hour at 4°C under gentle agitation. Cells were washed once with 25 mM Tris (pH=8.0) to quench the non-reacted biotinylation reagent and twice with ice-cold PBS to remove the non-reacted biotinylation reagent. Protein extraction was performed as described

above. An aliquot of supernatants corresponding to 600 µg of proteins was incubated with high-capacity streptavidin agarose resin (Thermo Fisher Scientific) for 2 hours at 4°C with gentle mixing, following the manufacturer's recommendation. Streptavidin-bound complexes were pelleted at 1000 g and washed four times with lysis buffer. Biotinylated proteins were eluted from the resin with reducing Sample Buffer 2X and directly used for Western blotting.

Western blotting

Protein concentrations from cell extracts were measured using the Bio-Rad protein assay system. Proteins were separated on 4–20% gradient SDS-PAGE gels and transferred onto PVDF membranes. Membranes were blocked for 1 hour at room temperature with 5% bovine serum albumin (BSA) in Tris-buffered saline containing 0.31% Tween 20 (TBST). Primary antibodies, diluted in TBST at the specified ratios, were applied to the membranes and incubated overnight at 4°C. Detection of primary antibody binding was performed using horseradish peroxidase-conjugated secondary antibodies (Sigma-Aldrich) and developed with a chemiluminescence ECL assay kit (Millipore Corporation). Protein band quantification was carried out using Quantity One analysis software (Bio-Rad).

Endocytic and Recycling assay

To assess endocytosis and recycling, we followed established protocols (Swiatecka-Urban et al. 2002, Cihil et al., 2012). Initially, plasma membrane proteins were labeled with the membrane-impermeable and cleavable EZ-Link™ Sulfo-NHS-SS-Biotin (Thermo Fisher Scientific) at 4°C. For endocytosis analysis, cells were subsequently warmed to 37°C for varying durations post-biotinylation. Afterward, the remaining Sulfo-NHS-SS-biotinylated proteins at the plasma membrane were treated with L-glutathione (GSH; MedChem Express) at 4°C to reduce disulfide bonds, indicating internalization into the endosomal compartment. Following cell lysis, biotinylated proteins were captured using streptavidin–agarose beads, eluted into SDS-sample buffer, and separated via SDS-PAGE. The level of biotinylated CFTR at 4°C, without prior warming, served as the baseline (100%). The background, representing biotinylated CFTR remaining at the plasma membrane after GSH treatment at 4°C without warming, was subtracted from the levels of biotinylated CFTR after each warming time point. CFTR endocytosis was determined by subtracting the background and expressed as the percentage of biotinylated CFTR at each time point compared to the baseline.

For the recycling assay, cells were warmed to 37°C for 5 minutes post-biotinylation and then cooled to 4°C. The disulfide bonds on plasma membrane proteins were reduced with GSH. Subsequently, cells were either lysed or subjected to additional warming periods at 37°C for different durations to allow endocytosed biotinylated CFTR to recycle to the plasma membrane. Following this, cells were cooled again to 4°C, and the disulfide bonds on recycled proteins were reduced with GSH. The extent of CFTR recycling was determined by comparing the levels of biotinylated CFTR after the initial and subsequent GSH treatments.

Endoglycosidase H assay

Digestion of glycosylated CFTR by endoglycosidase H (Endo H; New England Biolabs) was performed according to the manufacturer's protocol. Briefly, surface biotinylated and avidin-bound proteins or total protein extracts were incubated with a denaturing buffer (0.5% SDS and 0.4 M DTT) in a total reaction volume of 20 µl and incubated at 37℃ for 10 min. Samples were then treated with Endo H (1000 U/reaction) in GlycoBuffer (0.05 M Sodium Citrate, pH 5.5) at 37℃ for 1 hour. Digested samples were then mixed with 2x Laemmli Sample Buffer before Western blot analysis.

Phosphoproteomics

Following treatment with 25 µM PI3Kγ MP or an equimolar amount of control peptide (CP) for 30 min, F508del-CFBE41o- cells were lysed as described above, and protein samples were frozen at -80℃ before being subjected to an antibody microarray (KAM-1325 array) and data analysis, which was performed at Kinexus (System proteomic company, Vancouver, Canada). The array, which monitors changes in the expression levels and phosphorylation states of signaling proteins, includes 875 phosphosite-specific antibodies (for phosphorylation) and 451 pan-specific antibodies (for expression levels of these phosphoproteins). The resultant changes were expressed as percentages of change with respect to the control (% CFC). Only targets with % CFC above 60 or below -60 were considered as real significant changes.

Immunogold electron microscopy

Cells were plated on alcian blue-coated glass coverslips and fixed for 10 min with 0.05% glutaraldehyde in 4% paraformaldehyde (PFA) electron microscopy (EM) grade and 0.2 M HEPES buffer, and 50 min in 4% PFA EM grade in 0.2 M HEPES buffer. After three washes in PBS, cells were incubated for 10 min with 50 mM glycine and blocked for 1 hour in blocking buffer (0.2% bovine serum albumin, 5% goat serum, 50 mM NH_4Cl, 0.1% saponin, 20 mM PO_4 buffer, 150 mM NaCl). Staining with primary antibodies and nanogold-labeled secondary antibodies (Nanoprobes) was performed in blocking buffer at room temperature. Cells were fixed for 30 min in 1% glutaraldehyde and the nanogold was enlarged with gold enhancement solution (Nanoprobes) according to the manufacturer's instructions. Cells were post-fixed with osmium tetroxide, embedded in epon, and processed into ultrathin slices. After contrasting with uranyl acetate and lead citrate, the sections were analyzed with Zeiss LEO 512 electron microscope. Images were acquired by a 2k × 2k bottom-mounted slow-scan Proscan camera controlled by the EsivisionPro 3.2 software.

Proximity ligation assay

The Duolink® In Situ Red Starter Kit Mouse/Rabbit (Sigma-Aldrich) was used according to the manufacturer's protocol for proximity ligation assay. Briefly, F508del-CFBE41o- cells were seeded (30,000 cells/well) in a 24-well plate containing 12 mm sterile and coated coverslips. After 24 hours, cells were treated for 24 h with 3 µM Elexacaftor (VX-445) and 10 µM Tezacaftor (VX-661), alone or together with PI3Kγ MP (25 µM). Cells were then washed once with PBS 1X and fixed in 4% paraformaldehyde for 20 min at room temperature (RT). Next, cells were washed 3 times with PBS 1X and permeabilized with 0.1% Triton X-100 in 1% BSA-PBS for 20 min at RT. Blocking was performed with the Duolink® Blocking Solution for 1 h at 37°C. Primary antibodies were diluted in the Antibody

Diluent, added and incubated overnight at 4°C. The following day, cells were washed twice with Wash Buffer A 1X at RT for 5 min each, and subsequently incubated with the Duolink® PLUS and MINUS probes (1:5 diluted in Antibody Diluents) for 1 h at 37 ºC. After two additional washes with Wash Buffer A 1X, ligation of the probes was conducted by incubating the cells with a ligase for 30 min at 37°C. Before the amplification step, cells were washed twice with Wash Buffer A 1X and then incubated with a polymerase for 100 min at 37 °C. After two final washes with Wash Buffer B 1X and one wash with Wash Buffer B 0.01X, coverslips were mounted onto slides with Duolink® In Situ Mounting Media with DAPI for 15 min at RT, and then stored at -20°C before acquisition. Images were acquired using Leica TCS SP5 Confocal laser scanning microscope with a 40X objective.

Primary bronchial epithelial cell culture

Experiments with primary human bronchial epithelial (HBE) cells were conducted at the Istituto Giannina Gaslini in collaboration with Dr. Nicoletta Pedemonte, following a previously established protocol (Ghigo et al., 2022). In brief, epithelial cells were isolated from the mainstem bronchi of pwCF undergoing lung transplantation. Cells were derived from two donors homozygous for the F508del mutation and two with the F508del/G542X genotype. Bronchial tissues were incubated overnight at 4°C in a protease XIV-containing solution to isolate epithelial cells. Cells were cultured in a serum-free medium (a 1:1 mix of LHC9 and RPMI 1640) enriched with hormones and supplements to promote cell proliferation. Of note, the culture medium initially included a combination of antibiotics (typically colistin, piperacillin, and tazobactam) to eliminate bacterial contamination. To induce epithelial differentiation, cells were seeded at a high density (500,000 cells per 1 cm²) on porous Snapwell inserts (Corning). After 24 hours, the serum-free medium was replaced with Dulbecco's modified Eagle's medium/Ham's F12 supplemented with 2% fetal bovine serum (FBS) and additional growth factors. Differentiation into a polarized, tight epithelium was assessed by measuring transepithelial electrical resistance (TEER) and potential difference (PD) using an epithelial voltohmmeter (EVOM1; World Precision Instruments). The culture medium was refreshed daily on both sides of the membrane for 8 to 10 days (liquid-liquid interface). Subsequently, the apical medium was removed, transitioning the cells to an air-liquid interface (ALI) to enhance epithelial maturation. Cells were maintained under ALI conditions for 2 to 3 weeks before experimental use.

Short-circuit current measurements

Short-circuit current (I_{SC}) measurements in primary human bronchial epithelial cells were performed at the Istituto Giannina Gaslini in collaboration with Dr. Nicoletta Pedemonte, following a previously established protocol (Ghigo et al., 2022). Differentiated bronchial epithelia cultured on Snapwell inserts were mounted in vertical diffusion chambers resembling Ussing chambers with internal fluid circulation. Both the apical and basolateral hemichambers were filled with 5 mL of a solution containing 126 mM NaCl, 0.38 mM KH_2PO_4, 2.13 mM K_2HPO_4, 1 mM $MgSO_4$, 1 mM $CaCl_2$, 24 mM $NaHCO_3$, and 10 mM glucose. The chambers were continuously bubbled with a 5% CO_2/95% air gas mixture, and the temperature was maintained at 37°C. A voltage clamp (DVC-1000; World Precision Instruments) was

used to short-circuit the transepithelial voltage, with connections to the apical and basolateral chambers via Ag/AgCl electrodes and agar bridges (1 M KCl in 1% agar). Voltage offsets and fluid electrical resistance were compensated before each experiment. The I_{SC} signals were recorded using a PowerLab 4/25 analog-to-digital converter (ADInstruments, Dunedin, New Zealand) connected to a computer.

Statistical Analysis

Raw data were first analyzed to confirm their normal distribution via the Shapiro-Wilk test and then analyzed by unpaired Student's t-test, one-way analysis of variance (ANOVA), or two-way ANOVA. Bonferroni correction (one-way and two-way ANOVA) was applied to correct for multiple comparisons. In the absence of a normal distribution, nonparametric Kruskal-Wallis or Mann-Whitney tests were used, followed by Dunn's correction for multiple comparisons if appropriate. $P < 0.05$ was considered significant.

3. RESULTS

The PI3Kγ mimetic peptide increases the plasma membrane density of pharmacologically-corrected F508del-CFTR

First, we examined whether the PI3Kγ mimetic peptide (PI3Kγ MP) could affect the half-life of the mutant F508del-CFTR upon pharmacological correction with ETI. Six hours after inhibition of the *de novo* protein synthesis by cycloheximide (CHX), the amount of mature F508del-CFTR in F508del-CFBE41o- cells exposed to ETI dropped by 70% (Fig. 1a, b). Conversely, only 23% of the channel was degraded when PI3Kγ MP was added on top of the triple combination, indicating that PI3Kγ MP doubles the stability of ETI-corrected F508del-CFTR. Next, we sought to investigate whether the increased half-life of F508del-CFTR observed with PI3Kγ MP correlated with an increased residency of the channel at the plasma membrane. Immunogold staining in human embryonic kidney 293T (HEK293T) cells expressing a GFP-tagged F508del channel revealed that ETI significantly increased the amount of F508del-CFTR at the cell surface of 2-fold, and this effect was almost doubled by the addition of PI3Kγ MP (Fig. 1c, d). These findings were corroborated by experiments of cell surface protein biotinylation followed by streptavidin pulldown in immortalized CF human bronchial epithelial cells (F508del-CFBE41o-), showing a 3-fold higher amount of mature F508del-CFTR (C band) at the cell surface in cells treated with PI3Kγ MP plus ETI than in those exposed to ETI alone (Fig. 1e, f).

Given that localized elevation of cAMP has been shown to enhance CFTR stability at the plasma membrane by limiting its retrieval from the cell surface (Lobo et al., 2016), and considering that PI3Kγ MP acts as a cAMP-elevating agent, we hypothesized that its effect on CFTR levels could be due to a reduction in endocytosis. To determine whether the PI3Kγ MP-mediated increase in CFTR stability at the plasma membrane was linked to reduced endocytosis, we performed biotinylation-based endocytic assay in wt-CFBE41o- to assess CFTR internalization. Consistently, PI3Kγ MP significantly decreased the internalization of wt-CFTR, suggesting that its action in stabilizing the channel at the cell surface is mediated by inhibition of the endocytic trafficking (Fig. 1g).

Next, we assessed the functional impact of the PI3Kγ MP-mediated increase in F508del-CFTR plasma membrane density by measuring CFTR-dependent Cl^- secretion in primary bronchial epithelial (HBE) cells exposed to ETI alone or in combination with PI3Kγ MP. The membrane-permeable cAMP analog was used to induce the maximal CFTR activation, which is directly proportional to the channel density at the plasma membrane. In F508del/F508del HBE cells from two independent donors, the maximal CFTR activity elicited by cAMP-CPT and the relative current drop induced by the specific CFTR inhibitor $CFTR_{inh}$-172 at the end of the experiment were 25-30% higher in cells co-treated with PI3Kγ MP than in those exposed to ETI alone (Fig. 2a, b, c and Fig. 3a,b). Similar results were obtained in HBE cells derived from two patients with a more severe genotype, carrying the F508del mutation and the nonsense mutation G542X (Fig. 2d, e, f, and 3 c, d).

Overall, these results demonstrate that PI3Kγ MP maximizes the efficacy of the triple combination ETI by increasing the plasma membrane density of pharmacologically-corrected channels.

The PI3Kγ mimetic peptide promotes cell surface localization of the immature core-glycosylated F508del-CFTR

Next, we explored the mechanisms whereby the PI3Kγ MP improves the efficacy of ETI. First, we sought to determine whether the PI3Kγ MP could itself act as a CFTR corrector. Immunogold staining in non-corrected HEK293T cells expressing GFP-F508del-CFTR revealed a twofold increase in CFTR membrane density in cells exposed to PI3Kγ MP compared to those treated with a control peptide CP (Fig 4a, b). Notably, PI3Kγ MP heightened F508del-CFTR plasma membrane density to only 20% of the level observed in CFBE cells expressing the wild-type CFTR (Fig 4a, b). Cell surface biotinylation experiments in F508del-CFBE41o- cells confirmed a significant increase in CFTR levels at the cell membrane at 15 and 30 minutes after treatment with PI3Kγ MP compared to CP (Fig. 4c). Notably, PI3Kγ MP increased the abundance of the core-glycosylated (B band) but not the complex-glycosylated (C band) CFTR (Fig 4c). To corroborate the ability of PI3Kγ MP to increase the plasma membrane density of the immature core-glycosylated CFTR, biotinylated cell lysates were treated with Endoglycosidase H (Endo H), a glycosidase that does not cleave complex glycans. Endo H treatment induced a shift in the molecular weight of F508del-CFTR which was observed on the plasma membrane of CFBE cells treated with the peptide (Fig. 4d). This shift indicates that the channel was sensitive to Endo H and thus corresponded to the core-glycosylated form. Because the core-glycosylated CFTR can traffick to the plasma membrane *via* a GRASP-dependent unconventional secretory route (Gee et al., 2011) we next assessed to which extent PI3Kγ MP could affect this pathway. First, unconventional protein secretion was activated by blocking the conventional ER-to-Golgi traffic through syntaxin 5 (STX5) overexpression in HEK293T cells expressing F508del-CFTR (F508del-CFTR-HEK293T). STX5 overexpression alone promoted a significant increase in the surface expression of the immature, core-glycosylated form of the channel, which was further enhanced by PI3Kγ MP (Fig. 4e). Next, the unconventional secretory pathway was inhibited in F508del-CFTR-HEK293T cells by silencing a key component of the machinery, GRASP55 (Gee et al., 2011). PI3Kγ MP failed to increase the amount of core-glycosylated F508del-CFTR at the plasma membrane in GRASP55 knocked-down cells (Fig. 4f), indicating that the ability of PI3Kγ MP to promote the plasma membrane localization of immature F508del-CFTR relies on the GRASP-dependent unhfoìconventional secretory pathway. Notably, global cAMP elevation via either cell-permeable cAMP analogs or the adenylyl cyclase activator forskolin did not phenocopy PI3Kγ MP in enhancing the plasma membrane density of core-glycosylated F508del-CFTR (Fig. 5a, b), despite similarly activating PKA signaling. Similarly, the cAMP increase elicited by inhibitors of the main phosphodiesterase (PDE) isoforms expressed in F508del-CFBE41- cells (Turner et al., 2016), PDE3 and 4, failed to affect the cell surface localization of immature F508del-CFTR (Fig 5c, d), suggesting that the effect of the PI3Kγ MP depends on localized cAMP modulation.

Finally, we assessed the extent to which the core-glycosylated F508del-CFTR localized at the plasma membrane by PI3Kγ MP contributed to Cl^- secretion. Neither the cAMP analog CPT-cAMP nor the CFTR potentiator VX-770 stimulated I_{SC} in non-corrected F508del/F508del HBE cells chronically exposed to PI3Kγ MP, demonstrating the absence of functional CFTR channels at the cell surface (Fig.

6a, b). In contrast, F508del/F508del HBE cells treated with the CFTR corrector VX-809 exhibited cAMP-CPT/VX-770-stimulated currents (Fig. 6a, b). These findings demonstrate that, in the absence of pharmacological correction, the PI3Kγ MP promotes cell surface exposure of immature and non-functional F508del-CFTR.

The PI3Kγ mimetic peptide activates a AKAP-Lbc-anchored pool of protein kinase D1

Next, we next aimed to uncover the molecular mechanism through which PI3Kγ MP increases the plasma membrane abundance of F508del-CFTR channels. A targeted phosphoproteomics approach was used to assess the phosphorylation state of several hundred kinases and regulatory proteins of F508del-CFBE41o- cells upon treatment with PI3Kγ MP (Fig. 7a). The peptide triggered phosphorylation changes in a subset of proteins known to play roles in membrane remodeling (Fig. 7b-c) and trafficking (Fig. 7d), like small GTPases of the Rho/Rac/Cdc42 families (Olayoye et al. 2019, Diggins et al. 2018, Zhang et al. 2024, Megalhaes et al. 2021). Among these, protein kinase D1 (PKD1), a well-known regulator of membrane trafficking, endocytosis, and recycling of membrane proteins (Rozengurt et al. 2011, di Blasio et al., 2011) exhibited the most significant relative increase in phosphorylation in cells treated with PI3Kγ MP compared to those exposed to the control peptide CP (Fig. 7e). Phosphoproteomic results were corroborated by Western blot assays showing that PI3Kγ MP but not CP triggered PKD1 phosphorylation on activating serines 744 and 748 in HEK293T cells overexpressing the kinase (Fig. 8a).

To elucidate the molecular mechanism by which PI3Kγ MP promotes PKD1 activation, we examined the upstream signaling events. PKD1 activation requires coordinated PKC and PKA action, facilitated by AKAP-Lbc, a scaffold protein linked to vesicle secretion and exocytosis (Subramanian et al., 2019). In the AKAP-Lbc complex, PKC phosphorylates PKD1 on serines 744/748, while PKA-mediated phosphorylation of the AKAP promotes the release of the activated kinase (Carnegie et al., 2004). Pharmacological PKC inhibition with GO6983 nullified the effect of PI3Kγ MP on phosphorylation of serines 744 and 748 of PKD1 in HEK293T cells (Fig. 8b), indicating that the ability of the peptide to trigger PKD1 depends on PKC. Furthermore, PI3Kγ MP increased by 4 folds the phosphorylation of AKAP-Lbc on PKA phosphosites (Fig. 8c) and reduced by 50% the binding between the scaffold and PKD1 in HEK293T cells overexpressing both GFP-AKAP-Lbc and PKD1 (Fig 8d). To further prove that PI3Kγ MP specifically activates a AKAP-Lbc-anchored pool of PKD1, HEK293T cells were transfected with a plasmid encoding for a soluble version of the PH domain of AKAP-Lbc, which has been shown to antagonize PKD1 activation (Carnegie et al., 2024). In these cells, PI3Kγ MP failed to significantly raise PKD1 phosphorylation over basal values (Fig. 8e), demonstrating that the peptide controls a pool of PKD1 anchored by AKAP-Lbc.

Collectively, these data demonstrate that PI3Kγ MP orchestrates PKC- and PKA-mediated activation of an AKAP-Lbc-anchored pool of PKD1.

The PI3Kγ mimetic peptide promotes cell surface expression of pharmacologically-corrected F508del-CFTR via PKD1

Since AKAP-Lbc is associated with the export of cargo proteins from the endoplasmic reticulum (ER) (Subramanian et al., 2019), we next explored whether PKD1, released from the AKAP-signalosome by PI3Kγ MP, could localize in the vicinity of this compartment. Immunofluorescence analysis in HeLa cells revealed increased colocalization of PKD1 with the ER-resident protein disulfide isomerase (PDI) following PI3Kγ MP treatment (Fig. 9a-b), suggesting that PKD1 may transiently associate with the ER and potentially influence cargo trafficking. Next, we assessed to which extent PKD1 could localize in the vicinity of CFTR. Co-immunoprecipitation experiments in HEK293T cells overexpressing either wt-CFTR-GFP or F508del-CFTR-GFP revealed that PKD1 associated with both the normal and the mutant channel (Fig. 9c-d). Promixity ligation assays in CFBE cells confirmed that PKD1 localized in the proximity of both wt- and F508del-CFTR (Fig. 10a-b). Notably, in F508del-CFBE41o- cells the number of PLA dots was significantly increased by the treatment with ETI, and their abundance was further augmented by addition of PI3Kγ MP (Fig. 10b-d). In agreement, pharmacological PKD1 inhibition with CRT0066101 prevented PI3Kγ MP to increase F508del-CFTR plasma membrane density in CFBE-F508del-CFTR cells exposed to ETI (Fig. 11a-b). Overall, these results demonstrate that PI3Kγ MP maximizes F508del-CFTR plasma membrane localization in synergy with CFTR correctors via PKD1.

4. DISCUSSION

Our findings reveal a previously uncharacterized regulatory mechanism of CFTR membrane localization involving the PKA-anchoring function of PI3Kγ, supporting the pharmacological targeting of this pathway using PI3Kγ MP as a valuable strategy to overcome the limitations of existing modulator therapies. The ETI combination therapy is currently the standard of care for most pwCF, but it only partially restores F508del-CFTR function, reaching a maximum of approximately 50% of wild-type activity (Graeber et al., 2022), likely due to the inability of correctors to fully rescue CFTR stability defects and restore trafficking to the plasma membrane (Capurro et al., 2021). The observed stabilization of F508del-CFTR by PI3Kγ MP is strongly supported by our CHX chase experiments, which revealed that in the absence of PI3Kγ MP, the majority of ETI-corrected CFTR is rapidly degraded within six hours. In contrast, PI3Kγ MP significantly slowed this degradation, doubling the half-life of mature CFTR when added on top of ETI. This enhanced stability translates into a higher expression of the channel at the PM, as indicated by immunogold staining and surface biotinylation assays. Moreover, our data show that PI3Kγ MP reduces CFTR endocytosis, further supporting its role in stabilizing the channel at PM. These findings align with previous studies implicating cAMP-mediated pathways and cytoskeletal anchoring in CFTR stabilization (Lobo et al., 2016), reinforcing the potential of PI3Kγ MP as a complementary approach to ETI in prolonging CFTR surface residency and function. Consistently, we demonstrate that PI3Kγ MP significantly enhances ETI-mediated CFTR-dependent ion transport by approximately 20% in primary bronchial epithelial cells from F508del homozygous and heterozygous patients and continues to exert its effect even in F508del compound heterozygous cells carrying non-ETI-responsive alleles, such as the G542X stop mutation, suggesting that PI3Kγ MP could further improve ETI efficacy in pwCF carrying at least one responsive F508del allele. This increased total current is likely due to an increase in CFTR channels at the plasma membrane, as CPT-cAMP, which fully activates CFTR, boosts the current to its maximum; therefore, a higher current suggests more functional CFTR at the cell surface. Notably, the peptide enhances ETI effectiveness in cells derived from multiple patients sharing the same CF genotype, reinforcing the robustness of its effect despite the well-documented variability in clinical responses among patients with identical genotypes. Given the recent FDA expansion of ETI approval to include 271 additional mutations beyond F508del (https://www.cff.org/managing-cf/cftr-modulator-therapies), our approach could potentially benefit a broader range of patients, particularly those carrying class II and class IV mutations, although further studies are required.

Biochemical analyses and Ussing chamber experiments demonstrate that PI3Kγ MP does not promote CFTR full maturation when used alone, indicating that it acts on stabilization rather than correction. Interestingly, cell surface biotinylation and Western blotting experiments show that the peptide increases the surface density of non-corrected core-glycosilated F508del-CFTR (B band) in the absence of modulators, suggesting that its effect extends beyond mature CFTR stabilization. Here, we also demonstrate that the accumulation of core-glycosylated CFTR at the plasma membrane upon peptide treatment underlies the involvement of the GRASP-55-mediated unconventional secretion

pathway (Gee et al., 2011). However, since immature CFTR lacks the proper Golgi-dependent complex glycosylation necessary for full functionality, the physiological significance of its presence at the PM remains unclear. A plausible explanation is that PI3Kγ MP influences CFTR trafficking by promoting vesicle budding from the ER or enhancing an alternative cAMP-dependent pathway that facilitates delivery or redirection of misprocessed CFTR to the PM. Additionally, the increase in B band detected at the PM in F508del-CFBE41o- cells may suggest a protective effect against premature degradation, possibly by modulating intracellular quality control mechanisms that regulate CFTR turnover. While the functional consequences of this unconventional trafficking remain unclear, these findings raise the intriguing possibility that PI3Kγ MP influences multiple aspects of CFTR handling, including both surface stabilization and altered trafficking dynamics of F508del-CFTR.

The regulation of CFTR dynamics likely involves multiple downstream effectors of compartmentalized cAMP signaling, which orchestrates distinct trafficking and stabilization mechanism. Supporting this hypothesis, our phosphoproteomic analysis identified changes in a subset of proteins known to play roles in membrane remodeling and trafficking, like small GTPases of the Rho/Rac/Cdc42 families families (Olayoye et al. 2019, Diggins et al. 2018, Zhang et al. 2024, Megalhaes et al. 2021). Among these, PKD1, a well-known regulator of membrane trafficking, endocytosis, and recycling of membrane proteins scored the highest %CFC. A role of PKD1 in protein secretion was supported by published evidence showing that PKD1 activation is needed for PM localization of integrins, primarily by reducing endocytosis and promoting recycling (di Blasio et al., 2011). Remarkably, PKD1 has never been linked to regulation of CFTR biogenesis and trafficking hitherto. In this work, we demonstrate that PKD1 is the key player in the peptide's stabilizing effect on F508del-CFTR, as pharmacological inhibition of PKD1 with CRT0066101 completely blunts the effect of PI3Kγ MP on ETI-corrected F508del-CFTR. PKD1 full activation requires the integration of cAMP/PKA and PKC signaling pathways within a molecular complex orchestrated by AKAP-Lbc, a scaffold protein previously linked to ER export and exocytosis of cargo proteins "Subramanian et al., 2019). Consistent with this, our findings reveal that PI3Kγ MP promotes PKD1 activation by modulating an AKAP-Lbc-dependent signalling, reinforcing the idea that its effect on CFTR dynamics is mediated through a finely tuned cAMP signalling compartmentalization. In support of this, our findings indicate that PI3Kγ MP-mediated activation of PKD1 is accompanied by its increased colocalization with the ER-resident protein PDI, suggesting a potential role for PKD1 in regulating early secretory trafficking. Given the established function of PKD1 in membrane remodeling and vesicular transport, its presence at the ER raises the intriguing possibility that it contributes to the export of specific cargo, including CFTR. While preliminary, this observation supports a model in which PI3Kγ MP facilitates CFTR trafficking not only by stabilizing mature channels at the plasma membrane (di Blasio et al., 2011) but also by modulating upstream processes that govern CFTR exit from the ER. However, additional studies are required to determine whether PKD1 directly regulates CFTR export and to delineate the signaling events linking its recruitment to ER compartments with CFTR stabilization at the cell surface. Interestingly, PKD1 contains a PDZ-binding domain (Zhang et al., 2021) that may facilitate interaction with Na+/H+ exchanger regulatory factor (NHERF) family proteins, such as NHERF1 and NHERF2. These scaffold proteins link CFTR to the cytoskeleton and other stabilizing

complexes, thereby promoting its localization at PM and preventing premature internalization and degradation of channel. These observations are further supported by our co-IP and PLA experiments identifying PKD1 as a novel CFTR interactor and supporting a direct or complex-mediated interaction. In particular, PLA experiments in CFBE41o- cells demonstrate that PKD1 localizes in close proximity to both wt- and F508del-CFTR. Interestingly, in F508del-CFBE41o- cells, the number of PLA interaction signals significantly increased upon ETI treatment, and this effect was further enhanced by PI3Kγ MP, reinforcing the notion that PI3Kγ MP promotes CFTR stabilization through a PKD1-dependent mechanism. While the potential role of PKD1 in modulating the activity of NHERF scaffolding proteins and their interaction with CFTR is intriguing, further validation is needed to clarify their precise contribution to the observed stabilization effect. Although our data strongly support this mechanism, additional studies, including AKAP-Lbc silencing or inhibition in CFBE41o-, are still required to definitively confirm the involvement of AKAP-Lbc signalling in CFTR trafficking and stabilization.

Importantly, prolonged PKD1 hyperactivation raises concerns regarding potential side effects. Given PKD1's dual role in cell proliferation and inflammation, excessive activation could have implications in cardiovascular diseases and cancer (Nikonova et al., 2023), where PKD1 either suppresses tumor growth by inhibiting proliferation or, conversely, promotes tumor progression in certain cancers through pathways like Wnt signaling (Durand et al., 2016). To mitigate these potential risks, a targeted delivery approach, such as aerosol administration of PI3Kγ MP directly into the airways, could minimize systemic exposure and reduce off-target effects in other tissues. Furthermore, considering the peptide's ability to enhance cAMP signaling, it may also contribute to reducing CF-related chronic inflammation and improving airway function through bronchodilation, effects previously demonstrated (Ghigo et al., 2022).

Taken together, our results establish PI3Kγ MP as a promising multifunctional therapeutic strategy capable of enhancing CFTR modulation, improving stability and trafficking, and potentially addressing broader aspects of CF pathophysiology. We show that PI3Kγ MP maximizes the effects of ETI in rescuing F508del-CFTR function by promoting PKD1 activation and speculate that PKD1 may exert a dual effect on both trafficking and membrane stability of the channel. Since comprehensive preclinical safety studies have already been conducted on PI3Kγ MP, this approach is now approaching clinical validation, marking a significant step forward in the development of innovative therapies for cystic fibrosis.

5. FIGURES

Figure 1

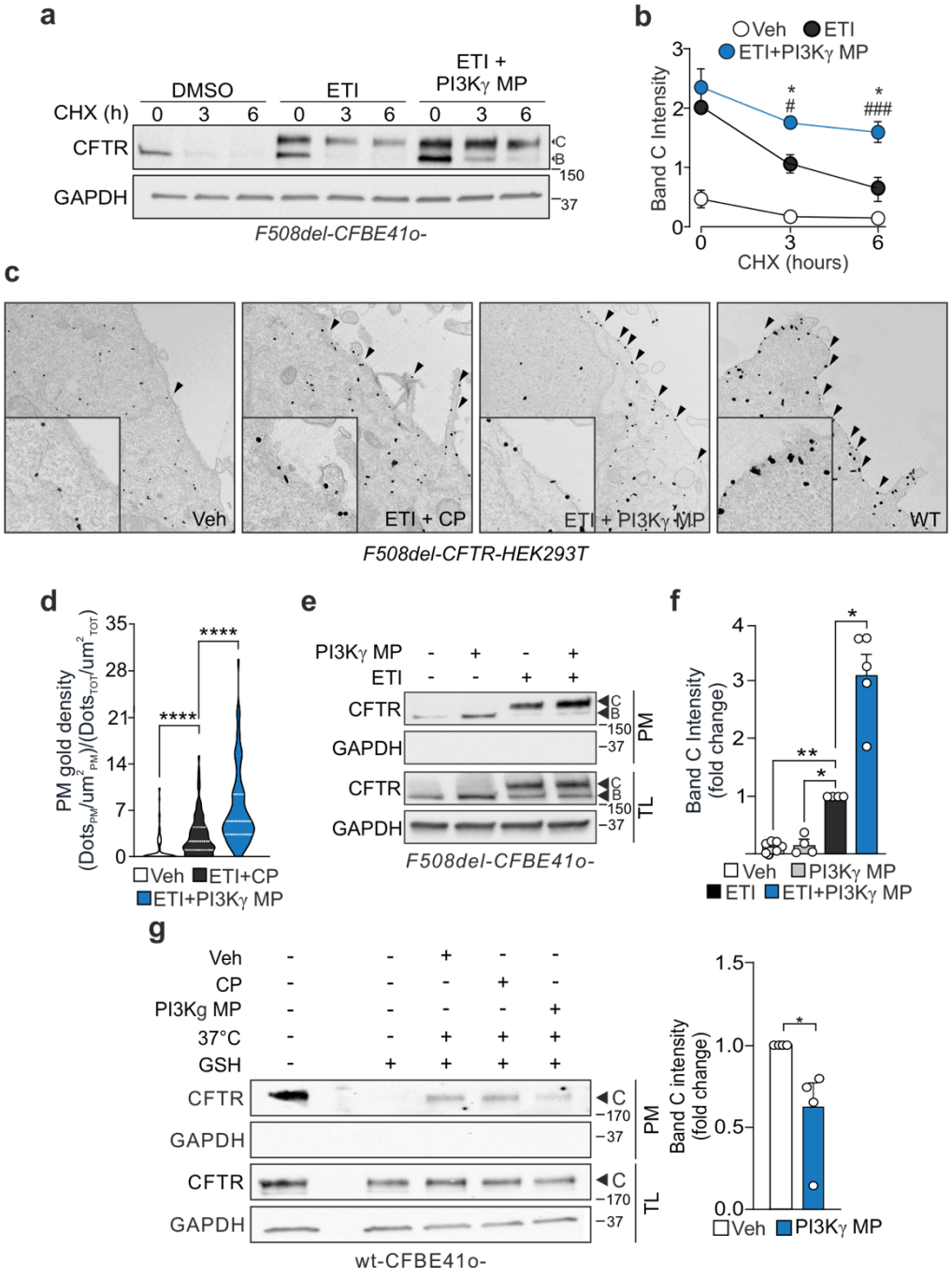

Figure 1. The PI3Kγ mimetic peptide increases plasma membrane density of pharmacologically-corrected F508del-CFTR. a) Representative western blot images showing CFTR and GAPDH levels in F508del-CFBE41o- cells treated for 24 h with ETI (3 μM VX-445, 10 μM VX-661, and 1 μM VX-770), either alone or together with PI3Kγ MP (25 μM, 24 h), before exposure to the inhibitor of the de novo protein synthesis, cycloheximide (CHX). Cells were lysed at the indicated time points after CHX treatment. **b)** Quantification of CFTR band C intensity in cells treated as described in (a), presented as fold change relative to t = 0. #P < 0.05 versus t = 0; *P < 0.05, and ***P

< 0.001 ETI versus ETI + PI3Kγ MP by one-way ANOVA followed by Bonferroni's post-hoc test. **c)** Representative pictures showing the distribution of F508del-CFTR-GFP overexpressed in HEK293T and detected by immunogold electron microscopy. Cells were treated for 24 h with either DMSO (Veh), ETI (3 μM VX-445, 10 μM VX-661, and 1 μM VX-770) plus a control peptide (ETI + CP), or ETI plus the PI3Kγ MP (ETI + PI3Kγ MP). HEK293T cells expressing wt-CFTR-GFP were used as a positive control. Insets provide higher magnification of selected regions, and arrows indicate CFTR channels located at the plasma membrane. **d**) Quantification of plasma membrane gold density in cells treated as in **c**. ****P < 0.0001 by Kruskal-Wallis test, followed by Dunn's multiple comparison test. **e**) Representative western blot images of CFTR and GAPDH plasma membrane levels in F508del-CFBE41o- cells treated chronically (24 h) with ETI (3 μM VX-445, 10 μM VX-661, and 1 μM VX-770) alone or with PI3Kγ MP (25 μM). GAPDH was not detected in the plasma membrane (PM) fraction, while CFTR and GAPDH were detected in the total lysate (TL) as loading controls. f) Quantification of plasma membrane CFTR band C intensity in cells treated as in (**e**), presented as fold change relative to ETI alone. *P < 0.05 and **P < 0.01 by Mann-Whitney test. **g**) Representative Western Blot (left) and relative quantification (right) of the amount of internalized (endocytosed) CFTR in wt-CFBE41o- cells upon treatment with vehicle (DMSO) or PI3Kγ MP (25 uM 30 min). Briefly, following treatment, cells were biotinylated, followed by incubation at 37°C (for 15). After that, cells were treated with a glutathione (GSH) solution and, after cell lysis and streptavidin pull down, CFTR was detected by western blotting (samples not treated with GSH – positive control; samples not incubated at 37°C – negative control). Throughout, data are mean ± SEM.

Figure 2

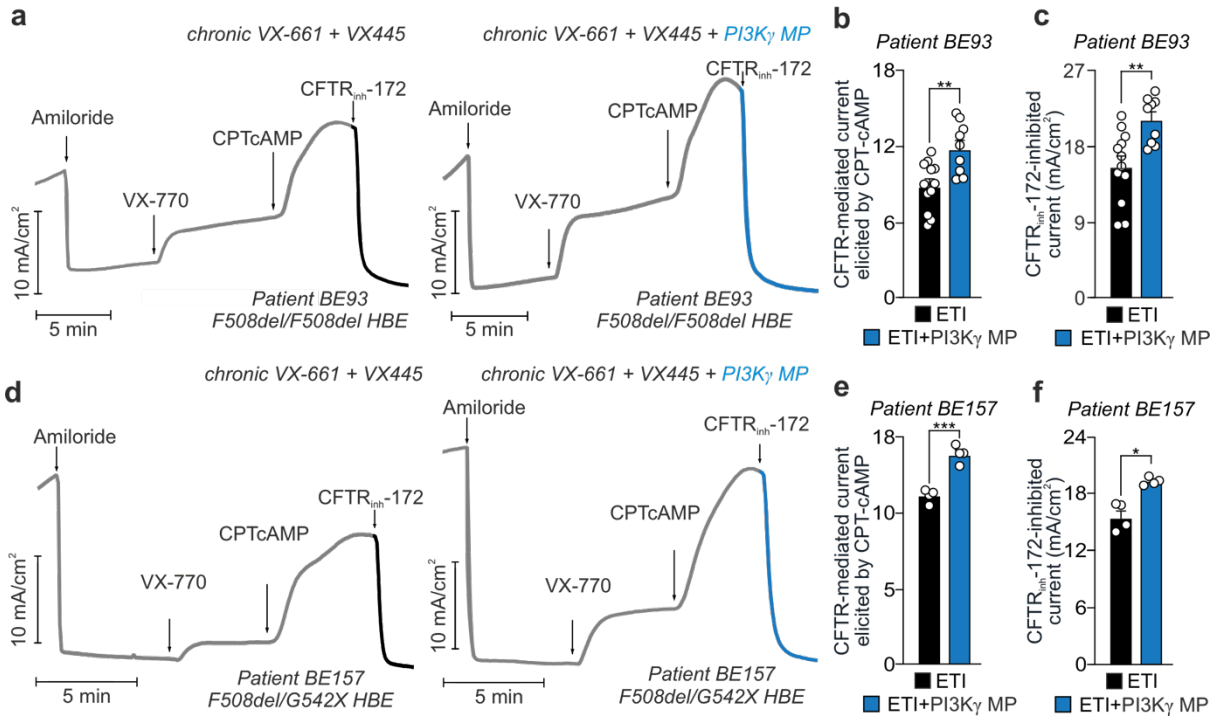

Figure 2. The PI3Kγ mimetic peptide enhances the effects of CFTR modulators in human bronchial epithelial cells from F508del/F508del and F508del/G542X CF donors. a) Representative traces of short-circuit current (I_{SC}) in primary human bronchial epithelial cells from a donor with CF (patient BE93) homozygous for the F508del mutation (F508del/F508del HBE) grown at the air-liquid interface (ALI). Cells were corrected for 24 h with 10 μM VX-661 and 3 μM VX-445, alone or with PI3Kγ MP (10 μM), and then exposed acutely to the following drugs: epithelial sodium channel inhibitor amiloride (100 μM), VX-770 (1 μM), CPTcAMP (100 μM), and CFTR inhibitor 172 (CFTRinh-172; 10 μM). **b)** Average total current variation in response to CPT-cAMP (100 μM) from n = 9-12 technical replicates of donor BE93. **P < 0.01 by Student's t-test. **c)** Average total current variations in response to CFTRinh-172 (10 μM) from n = 9-12 technical replicates of donor BE93. **P < 0.01 by Student's t-test. **d**) Representative traces of I_{SC} in primary human bronchial epithelial cells from a donor with CF (patient 157) heterozygous for the F508del mutation (F508del/G542X HBE) grown at the ALI. Cells were corrected for 24 h with 10 μM VX-661 and 3 μM VX-445, alone or with PI3Kγ MP (10 μM), followed by acute exposure to amiloride (100 μM), VX-770 (1 μM), CPTcAMP (100 μM), and CFTRinh-172 (10 μM) at the indicated times. **e)** Average total current variations in response to CFTRinh-172 (10 μM) from n = 4 technical replicates of donor BE157. ***P < 0.001 by Student's t-test. **f)** Average total current variations in response to CFTRinh-172 (10 μM) from n = 4 technical replicates of donor BE157. *P < 0.05 by Mann-Whitney test. Throughout, data are mean ± SEM.

Figure 3

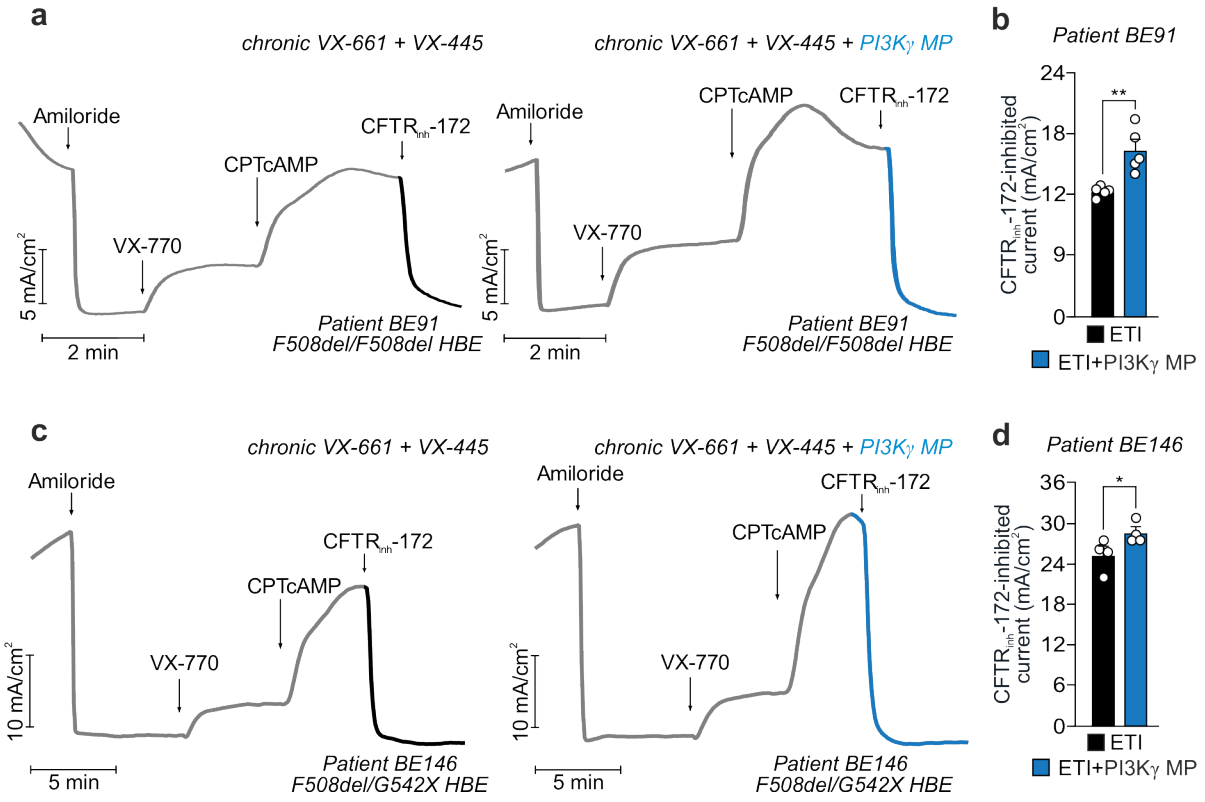

Figure 3. The PI3Kγ mimetic peptide enhances the effects of CFTR modulators in human bronchial epithelial cells from F508del/F508del and F508del/G542X CF donors. a) Representative traces of short-circuit current (I_{SC}) in primary human bronchial epithelial cells from a donor with CF (patient BE91) homozygous for the F508del mutation (F508del/F508del HBE) grown at the air-liquid interface (ALI). Cells were corrected for 24 h with 10 μM VX-661 and 3 μM VX-445, alone or with PI3Kγ MP (10 μM), and then exposed acutely to the following drugs: epithelial sodium channel inhibitor amiloride (100 μM), VX-770 (1 μM), CPTcAMP (100 μM), and CFTR inhibitor 172 (CFTRinh-172; 10 μM). **b)** Average total current variations in response to CFTRinh-172 (10 μM) from n = 5 technical replicates of donor BE93. **P < 0.01 by Student's t-test. **c**) Representative traces of I_{SC} in primary human bronchial epithelial cells from a donor with CF (patient 146) heterozygous for the F508del mutation (F508del/G542X HBE) grown at the ALI. Cells were corrected for 24 h with 10 μM VX-661 and 3 μM VX-445, alone or with PI3Kγ MP (10 μM), followed by acute exposure to amiloride (100 μM), VX-770 (1 μM), CPTcAMP (100 μM), and CFTRinh-172 (10 μM) at the indicated times. **d)** Average total current variations in response to CFTRinh-172 (10 μM) from n = 4 technical replicates of donor BE157. *P < 0.05 by Mann-Whitney test. Throughout, data are mean ± SEM.

Figure 4

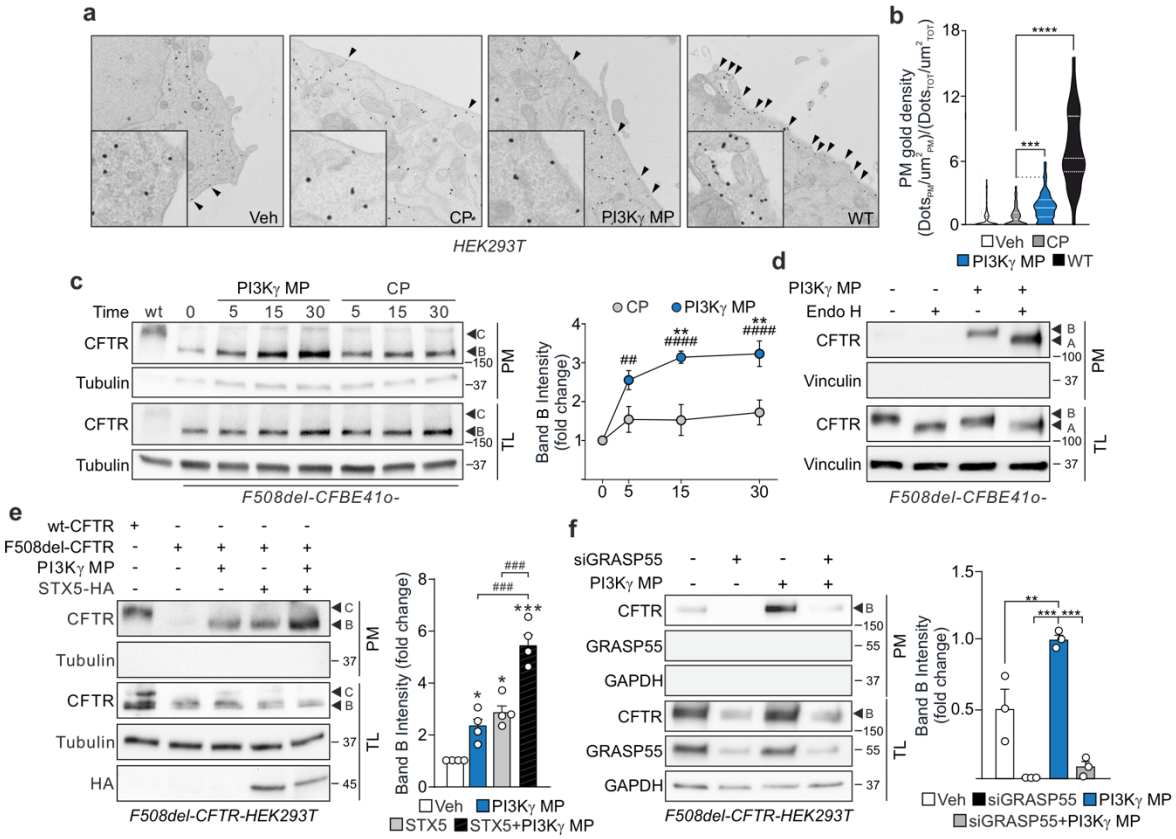

Figure 4. The PI3Kγ mimetic peptide does not affect F508del-CFTR maturation. a) Distribution of gold-labeled GFP by immunogold electron microscopy (IEM) in HEK293T cells transfected with F508del-CFTR-GFP and treated for 15 minutes with either DMSO (Veh), a control peptide (CP), or with the PI3Kγ MP. HEK293T cells expressing wt-CFTR-GFP were used as a positive control. **b)** Quantification of plasma membrane gold density of cells treated as in a. ****P < 0.0001 by Kruskal-Wallis test, followed by Dunn's multiple comparison test. **c)** Left, western blot representative images of CFTR and GAPDH levels in F508del-CFBE41o- cells treated with either CP or PI3Kγ MP for the indicated time points (5, 15, 30 min) and subjected to cell surface biotinylation. After streptavidin pull down, CFTR was detected by western blotting. Untreated cells (t = 0) served as negative controls. wt-CFTR was used as a control for band C CFTR molecular weight. The cytosolic marker GAPDH was absent in the biotinylated fraction, confirming plasma membrane (PM) specificity. CFTR and GAPDH were detected in total lysate (TL) as loading controls. Right, quantification of CFTR levels at the plasma membrane. ##P < 0.01 ####P < 0,0001 versus untreated (t = 0), and **P <0.01 versus CP by one-way ANOVA followed by Bonferroni's post-hoc test. **d)** Representative western blot images of CFTR and GAPDH levels in F508del-CFBE41o- cells exposed to the PI3Kγ MP (25 μM) for 15 minutes and subjected to cell surface biotinylation. After cell lysis and protein purification, plasma membrane proteins were pulled down with streptavidin-based beads and then incubated with Endoglycosidase H (Endo H, 1000 U/reaction) for 1 hour. The cytosolic marker GADPH was not detected in the biotinylated fraction, showing PM specificity. CFTR and GAPDH were detected in TL as loading controls. **e)** Left: representative western blot images of CFTR, GAPDH, and HA levels in HEK293T cells transfected with ΔF508-CFTR alone or with a plasmid expressing STX5-HA to block conventional trafficking. Cells were treated with PI3Kγ MP for 30 minutes, 24 hours post-transfection, and then subjected to cell surface biotinylation. After streptavidin pull down, CFTR was detected by western blotting. wt-CFTR was used as a control for band C CFTR molecular weight. GAPDH was

absent in the biotinylated fraction, confirming PM specificity, while CFTR and GAPDH were detected in the TL as loading controls. Right: quantification of CFTR levels at the plasma membrane. ###P < 0.001 by one-way ANOVA followed by Bonferroni's post-hoc test. *P < 0.05, and ***P < 0.001 versus Veh by one-way ANOVA followed by Bonferroni's post-hoc test. **f)** Left: representative western blot images showing CFTR, GRASP55, and GAPDH levels in HEK293T cells transfected with ΔF508-CFTR alone or with a siRNA targeting GRASP55, to inhibit the unconventional CFTR trafficking. Cells were treated with PI3Kγ MP for 30 minutes, 72 hours post-siRNA transfection, and then subjected to cell surface biotinylation. After streptavidin pull down, CFTR was detected by western blotting. GAPDH was absent in the biotinylated fraction, confirming PM specificity, while CFTR and GAPDH were detected in the TL as loading controls. Right, quantification of CFTR levels at the plasma membrane. **P < 0.01, and ***P < 0.001 by one-way ANOVA followed by Bonferroni's post-hoc test. Throughout, data are mean ± SEM.

Figure 5

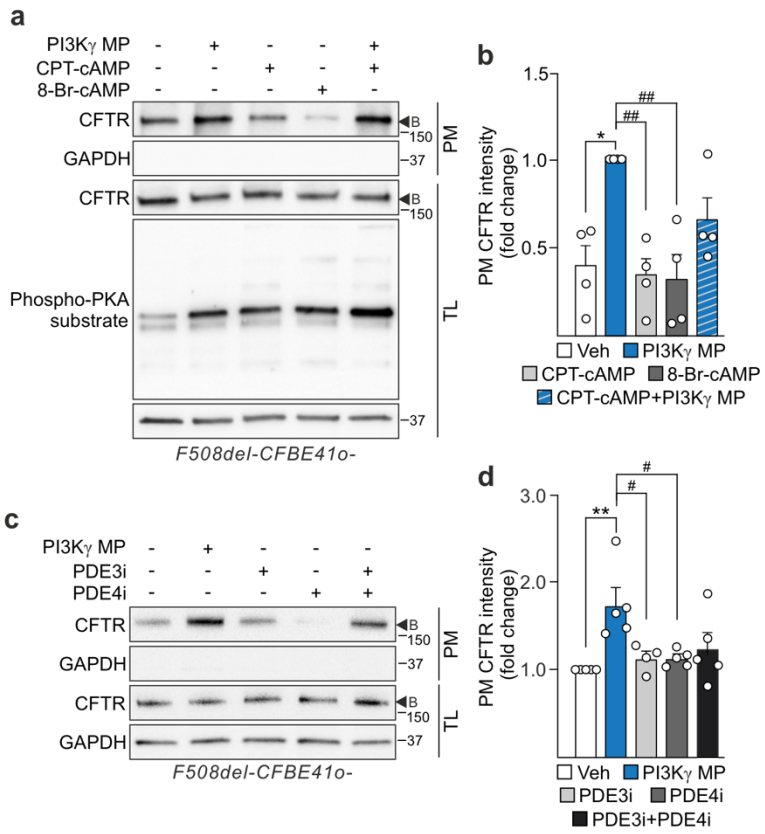

Figure 5. The effect of the PI3Kγ MP depends on localized cAMP modulation. a) Western blot representative images of CFTR and GAPDH levels in F508del-CFBE41o- cells treated with either PI3Kγ MP or cAMP analogs CPT-cAMP and 8-Br-cAMP for the indicated time points (30 min) and subjected to cell surface biotinylation. After streptavidin pull down, CFTR was detected by western blotting. Untreated cells (t = 0) served as negative controls. wt-CFTR was used as a control for band C CFTR molecular weight. PKA-mediated phosphorylation levels were also evaluated in these cell lysates. The cytosolic marker GAPDH was absent in the biotinylated fraction, confirming plasma membrane (PM) specificity. CFTR and GAPDH were detected in total lysate (TL) as loading controls. **b**) Quantification of CFTR levels at the plasma membrane in (**a**). ##P < 0.01 versus PI3Kγ, and *P <0.05 versus vehicle by one-way ANOVA followed by Bonferroni's post-hoc test. **c)** Representative western blot images of CFTR and GAPDH levels in F508del-CFBE41o- cells exposed to either PI3Kγ MP (25 μM) or PDE3 and PDE4 inhibitors for 30 minutes and subjected to cell surface biotinylation. After cell lysis and protein purification, plasma membrane proteins were pulled down with streptavidin-based beads. The cytosolic marker GADPH was not detected in the biotinylated fraction, showing PM specificity. CFTR and GAPDH were detected in TL as loading controls. **d**) quantification of CFTR levels at the plasma membrane. **P < 0.01, and #P < 0.05 versus PI3Kγ, and *P <0.05 versus vehicle by one-way ANOVA followed by Bonferroni's post-hoc test. Throughout, data are mean ± SEM.

Figure 6

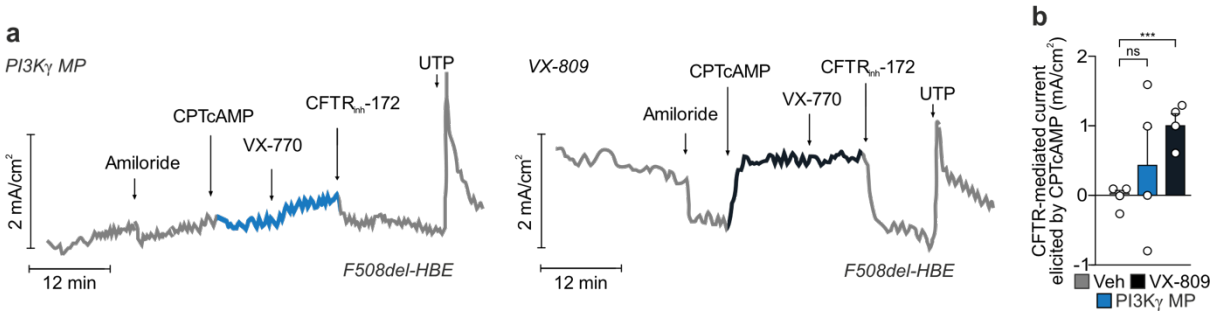

Figure 6. The PI3Kγ MP promotes cell surface exposure of immature and nonfunctional F508del-CFTR. a) Representative traces of short-circuit current (I_{SC}) in primary human bronchial epithelial cells from a donor with CF homozygous for the F508del mutation grown at the air-liquid interface (ALI). Cells were exposed for 24 h to either PI3Kγ MP (25 μM) or VX-809 10 μM and then exposed acutely to the following drugs: epithelial sodium channel inhibitor amiloride (100 μM), CPTcAMP (100 μM), VX-770 (1 μM), CFTR inhibitor 172 (CFTRinh-172; 10 μM) and UTP. **b)** Average total current variations in response to CFTRinh-172 (10 μM) from n = 5 technical replicates of donor BE93. **P < 0.01 by Student's t-test.

Figure 7

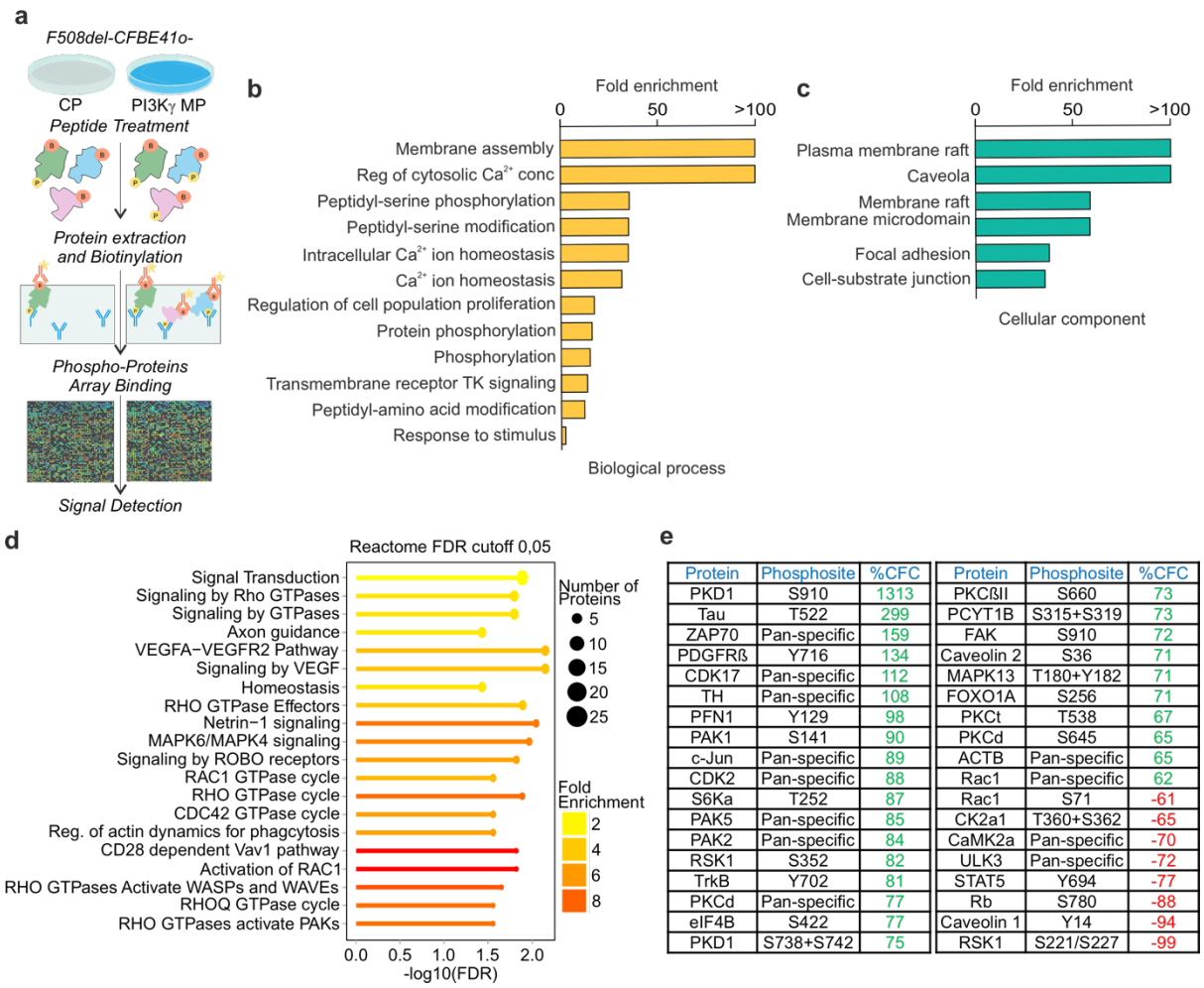

e

Protein	Phosphosite	%CFC
PKD1	S910	1313
Tau	T522	299
ZAP70	Pan-specific	159
PDGFRß	Y716	134
CDK17	Pan-specific	112
TH	Pan-specific	108
PFN1	Y129	98
PAK1	S141	90
c-Jun	Pan-specific	89
CDK2	Pan-specific	88
S6Ka	T252	87
PAK5	Pan-specific	85
PAK2	Pan-specific	84
RSK1	S352	82
TrkB	Y702	81
PKCd	Pan-specific	77
eIF4B	S422	77
PKD1	S738+S742	75

Protein	Phosphosite	%CFC
PKCßII	S660	73
PCYT1B	S315+S319	73
FAK	S910	72
Caveolin 2	S36	71
MAPK13	T180+Y182	71
FOXO1A	S256	71
PKCt	T538	67
PKCd	S645	65
ACTB	Pan-specific	65
Rac1	Pan-specific	62
Rac1	S71	-61
CK2a1	T360+S362	-65
CaMK2a	Pan-specific	-70
ULK3	Pan-specific	-72
STAT5	Y694	-77
Rb	S780	-88
Caveolin 1	Y14	-94
RSK1	S221/S227	-99

Figure 7. Phosphoproteomic analysis reveals PI3Kγ MP-induced modulation of membrane organization and GTPase-mediated signaling pathways. a) Schematic representation of the experimental workflow applied to analyze differences in F508del-CFBE41o- cells in protein phosphorylation upon either a control peptide (CP) or the PI3Kγ MP by using a microarray including 875 phosphosite-specific antibodies and 451 pan-specific antibodies. **b**-**c**) Panther Gene Ontology (GO) slim-term enrichment analysis of the genes encoding the proteins with altered phosphorylation after PI3Kγ MP treatment compared to CP. Significantly enriched GO terms (FDR < 0.05) are categorized into Biological Processes (**b**), and Cellular Components (**c**). **d**) Reactome pathway enrichment analysis of the proteins with altered phosphorylation upon PI3Kγ MP treatment compared to CP. Each line represents one of the top 20 Reactome pathways. The x-axis shows the -log10 of the false discovery rate (FDR), with colors ranging from yellow to red indicating increasing fold enrichment. Circle sizes represent the number of proteins. The entire phospho-array protein list was used as a background reference. **e**) Phospho-proteomic analysis in F508del-CFBE41o- cells comparing PI3Kγ MP treatment to CP. Data are expressed as a change from control (%CFC), where 100% corresponds to a 2-fold increase in signal intensity following PI3Kγ MP treatment relative to CP. Negative values indicate a decrease in signal intensity. Only targets with %CFC above 60 or below -60 were included (n = 36).

Figure 8

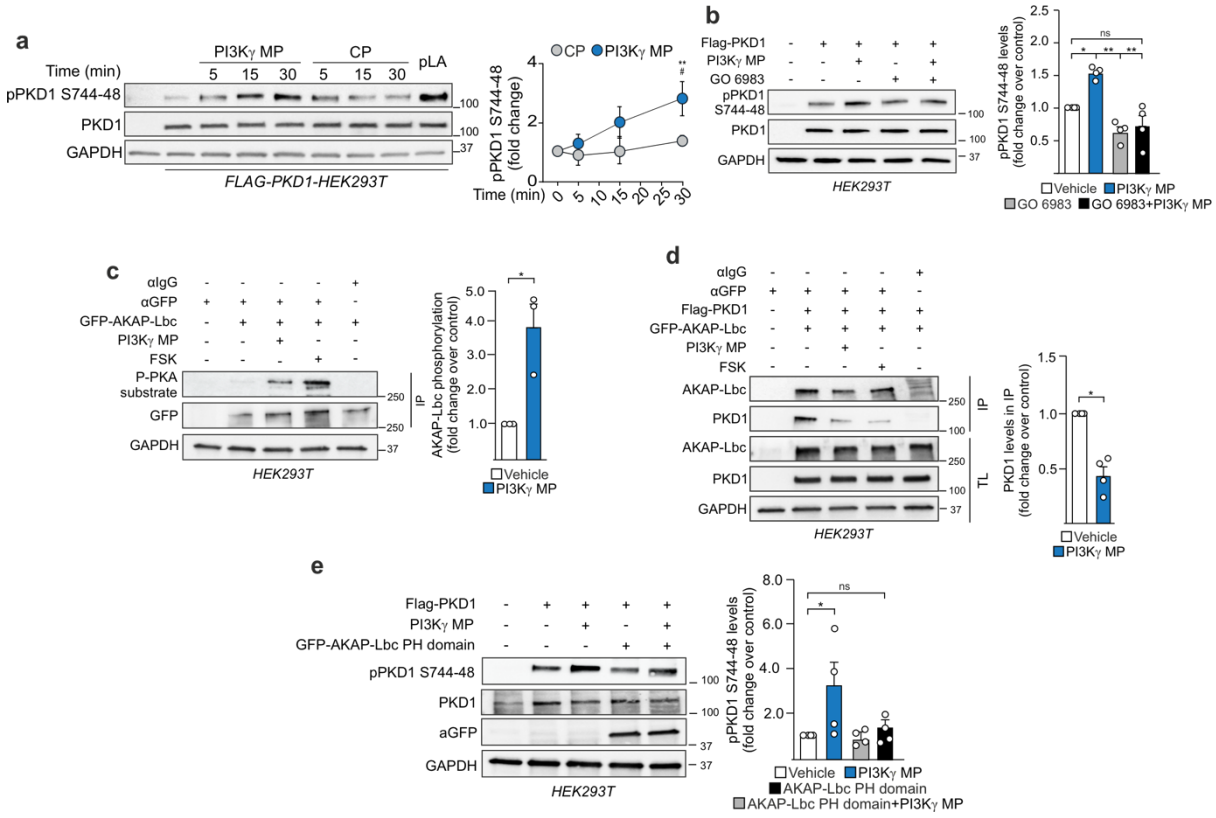

Figure 8. The PI3Kγ mimetic peptide activates a AKAP-Lbc-anchored pool of protein kinase D1. a) Representative immunoblot images showing pPKD1 S744-748, PKD1, and GAPDH levels in PKD1-overexpressing HEK293T cells treated with either CP (25 μM) or PI3Kγ MP (25 μM) for the indicated time points. Lysate from cells treated for 10 minutes with poly-L arginine (pLA) was used as a positive control. First two lanes correspond to non-transfected cells and transfected and untreated cells, respectively. **P<0.01 vs vehicle, #P<0.05 vs CP 30 min by Student t test **b**) Left: representative immunoblot images of pPKD1 S744-S784, PKD1, and GAPDH content in HEK293T cells overexpressing Flag-PKD1. Cells were treated with PI3Kγ MP (30 min, 25 μM) alone or with a 30 min long pre-incubation with the PKC inhibitor GO6983 (0.5 μM). Right: quantification of the pPKD1 S744-748/total PKD1 of data shown on the left panel. Values are displayed as fold change over DMSO (Veh). **c**) Left: representative immunoblot images of PKA-mediated phosphorylation of GFP-precipitated AKAP-Lbc in HEK293T cells exposed to DMSO (Veh), PI3Kγ MP (25 μM, 30 min), or Fsk (1.5 μM, 10 min). IP: immunoprecipitation. Right: quantification of the PKA-mediated AKAP-Lbc phosphorylation/total AKAP-Lbc of data shown on the left panel. Values are displayed as fold change over DMSO (Veh). **d**) Left: representative immunoblot images of Flag-PKD1 co-immunoprecipitated with GFP-precipitated AKAP-Lbc in HEK293T cells exposed to DMSO (Veh), PI3Kγ MP (25 μM, 30 min), or Fsk (1.5 μM, 10 min). IP: immunoprecipitation. Right: quantification of the PKA-mediated AKAP-Lbc phosphorylation/total AKAP-Lbc of data shown on the left panel. Values are displayed as fold change over DMSO (Veh). **e**) Left: representative immunoblot images of pPKD1 S744-S784, PKD1, GFP, and GAPDH content in HEK293T cells treated with either Veh or PI3Kγ MP (25 μM, 30 min) overexpressing Flag-PKD1 alone or with the PH domain of AKAP-Lbc mediating the interaction with PKD1. Right: quantification of the pPKD1 S744-748/total PKD1 of data shown on the left panel. Values are displayed as fold change over DMSO (Veh). ** P<0.01, *P<0.05

by Student t test or one-way ANOVA followed by Bonferroni post-hoc correction. Throughout, data are mean ± SEM.

Figure 9

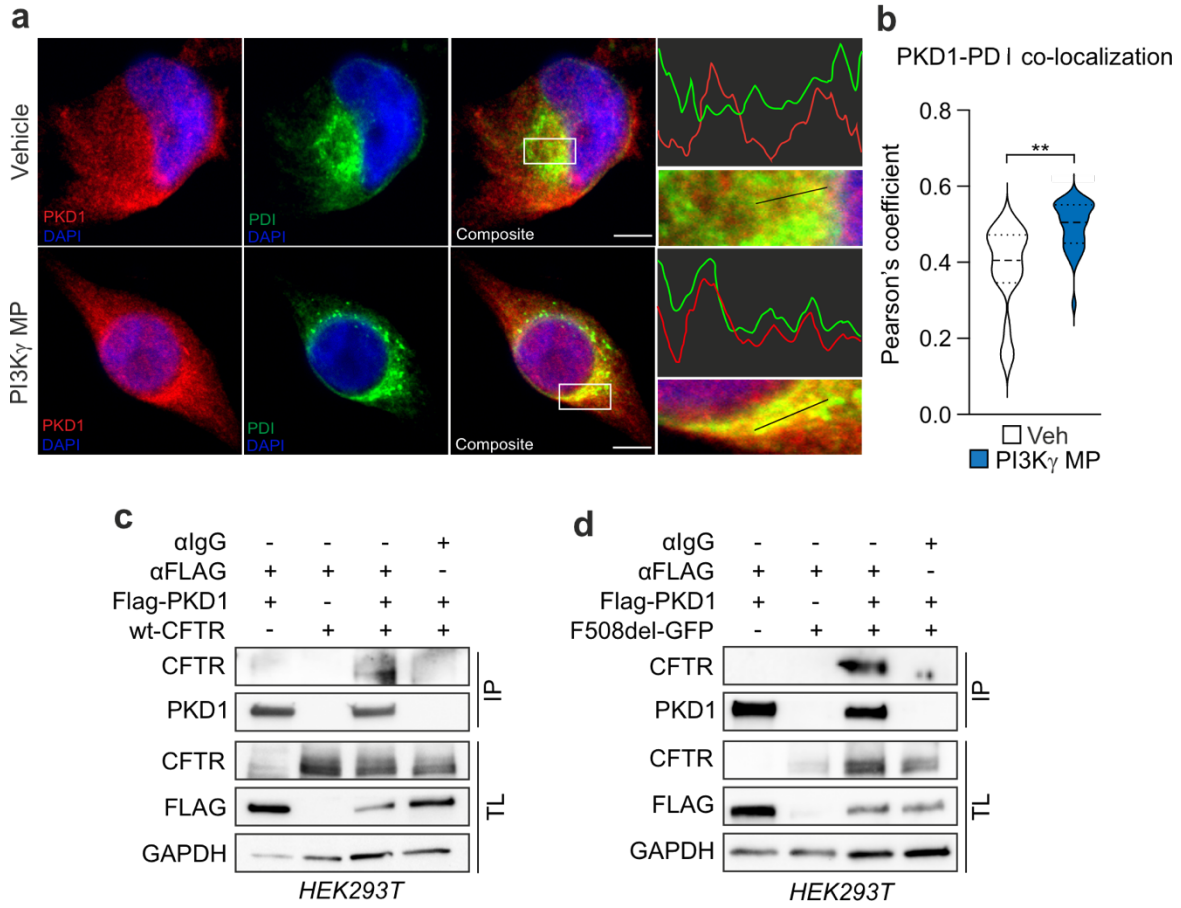

Figure 9. PKD1 interacts with both wt-CFTR and F508del-CFTR. a) Double immunofluorescence staining of PKD1 and ER-resident protein disulfide isomerase (PDI) in HeLa cells treated with either DMSO (top; Vehicle) or PI3Kγ MP (25 μM) bottom). Right, Enlargements of the outlined areas and fluorescence intensity profiles in the green and red channels of the regions underneath the black lines. Scale bar, 5 μm. Representative pictures from n=3 experiments are shown. **b**) Violin plots showing quantification of PKD1 and PDI co-localization expressed as Pearson's coefficient. **P < 0.01 by Student's t-test. **c**-**d**) Representative co-immunoprecipitation images of wt-CFTR (**c**) and F508del-CFTR (**d**) with PKD1 in HEK293T cells transfected with F508del-GFP and Flag-PKD1. IP: immunoprecipitation; TL: total lysate.

Figure 10

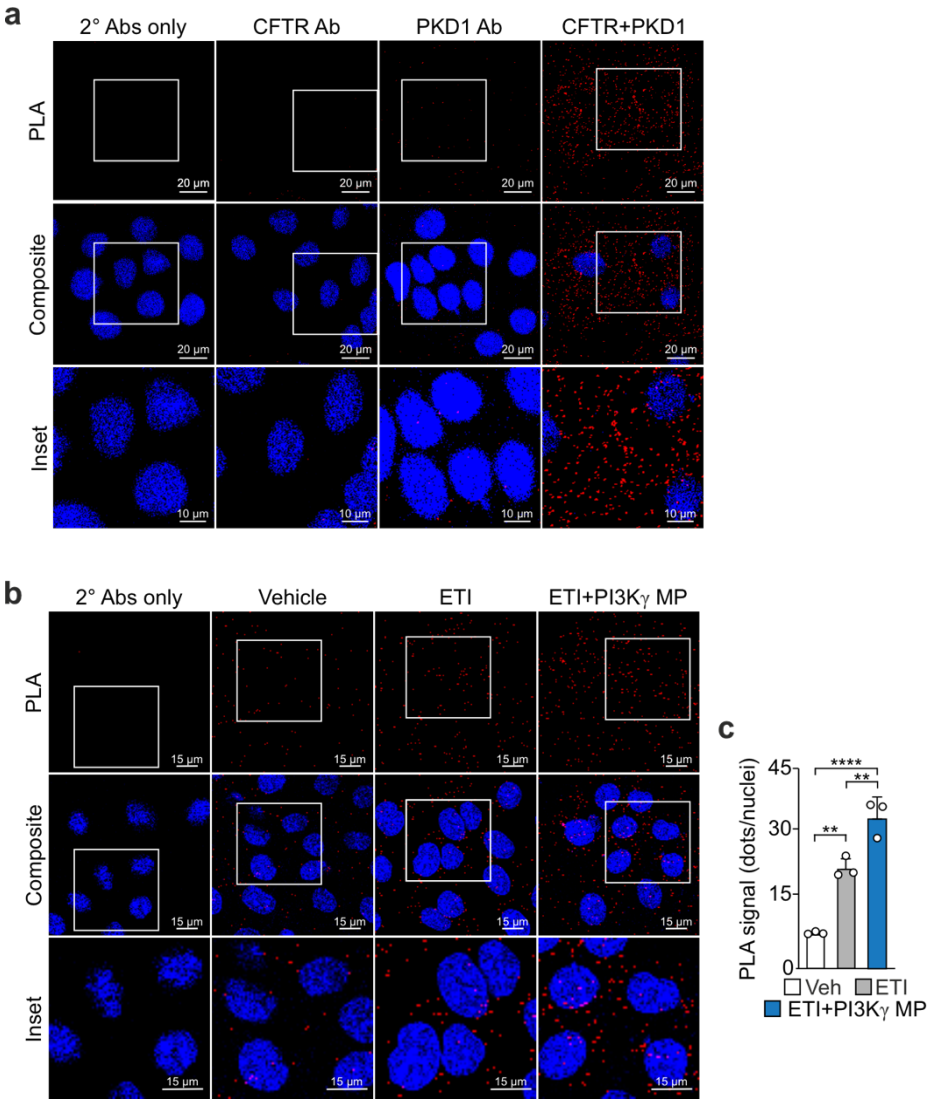

Figure 10. The PI3Kγ mimetic peptide promotes the interaction between f508del-CFTR and PKD1. a) Representative pictures showing the interaction between wt-CFTR and PKD1 as dots generated through proximity ligation assay (PLA) in wt-CFBE41o- cells. **b**) Representative pictures showing the interaction between F508del-CFTR and PKD1 as dots generated through proximity ligation assay (PLA) in F508del-CFBE41o- cells. **c**) Quantification of the number of dots per cell generated via PLA using primary antibodies against CFTR and PKD1 in F508del-CFBE41o- cells treated with ETI (3 µM VX-445, 10 µM VX-661 and 1 µM VX-770) alone or with PI3Kγ MP (25 µM) for 24h. **** P<0.0001, **P<0.01 by one-way ANOVA followed by Bonferroni post-hoc correction. Throughout, data are mean ± SEM

Figure 11

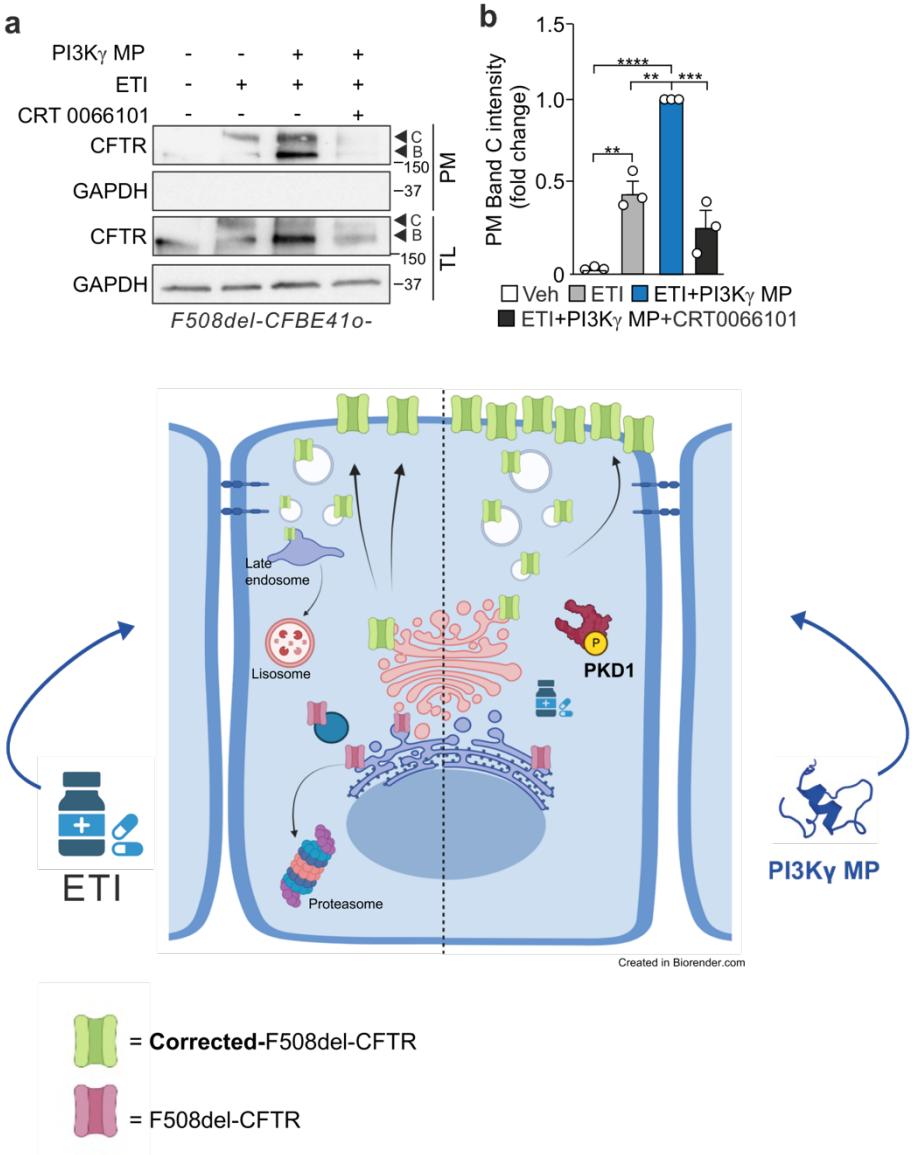

Figure 11. The PI3Kγ mimetic peptide modulates CFTR localization at the cell surface through protein kinase D1 (PKD1). a) Representative immunoblot images showing CFTR and GAPDH levels in HEK293T cells treated for 24h with ETI (3 μM VX-445, 10 μM VX-661, and 1 μM VX-770), PI3Kγ MP (25 μM), and the PKD inhibitor CRT0066101 (10 μM). GAPDH was absent in the biotinylated fraction, confirming plasma membrane (PM) specificity, while CFTR and GAPDH were detected in the total lysate (TL) as loading controls. **b**) Quantification of CFTR levels at the plasma membrane of data shown in (**a**). Values are displayed as fold change over ETI+ PI3Kγ MP. **P < 0.01, ***P < 0.001, and ****P < 0.0001 by one-way ANOVA followed by Bonferroni's post-hoc test. **c**) Left, ETI only achieves suboptimal rescue of F508del-CFTR trafficking and stability at plasma membrane. Right, PI3Kγ MP increases the therapeutic efficacy of ETI in stabilizing F508del-CFTR, through the activation of PKD1, a novel F508del-CFTR interactor. Throughout, data are means ± SEM.

Bibliography

Alam, N., A. K. Wright, D. M. Ashcroft and A. G. Renehan (2020). "Cancer and cardiovascular disease." Lancet **395**(10241): 1903-1904.

Amgalan, D., T. P. Garner, R. Pekson, X. T. F. Jia, M. Yanamandala, V. Paulino, F. G. Liang, J. J. Corbalan, J. Lee, Y. Chen, G. S. Karagiannis, L. R. Sanchez, H. Z. Liang, S. R. Narayanagari, K. Mitchell, A. Lopez, V. Margulets, M. Scarlata, G. Santulli, A. Asnani, R. T. Peterson, R. B. Hazan, J. S. Condeelis, M. H. Oktay, U. Steidl, L. A. Kirshenbaum, E. Gavathiotis and R. N. Kitsis (2020). "A small-molecule allosteric inhibitor of BAX protects against doxorubicin-induced cardiomyopathy." Nature Cancer **1**(3): 315-+.

Asnani, A. (2021). "Activating Autophagy to Prevent Doxorubicin Cardiomyopathy The Timing Matters." Circulation Research **129**(8): 801-803.

Avila, M. S., S. M. Ayub-Ferreira, M. R. D. Wanderley, F. D. Cruz, S. M. G. Brandao, V. O. C. Rigaud, M. H. Higuchi-dos-Santos, L. A. Hajjar, R. Kalil, P. M. Hoff, M. Sahade, M. S. M. Ferrari, R. L. D. Costa, M. S. Mano, C. Cruz, M. C. Abduch, M. S. L. Alves, G. V. Guimaraes, V. S. Issa, M. S. Bittencourt and E. A. Bocchi (2018). "Carvedilol for Prevention of Chemotherapy-Related Cardiotoxicity." Journal of the American College of Cardiology **71**(20): 2281-2290.

Ayub-Ferreira, S. M., M. Avila, S. Brandao, F. D. Cruz, M. Wanderley, V. O. C. Rigaud, L. Hajjar, R. Kalil, C. B. V. Cruz, M. S. Alves, G. V. Guimaraes, M. Abduch, V. S. Issa, M. Santos, M. Bittencourt and E. A. Bocchi (2020). "CARVEDILOL FOR PREVENTION OF CHEMOTHERAPY-INDUCED CARDIOTOXICITY: FINAL RESULTS OF THE PROSPECTIVE, RANDOMIZED, DOUBLE-BLIND, PLACEBO CONTROLLED CECCY TRIAL." Journal of the American College of Cardiology **75**(11): 658-658.

Bergsbaken, T., S. L. Fink and B. T. Cookson (2009). "Pyroptosis: host cell death and inflammation." Nature Reviews Microbiology **7**(2): 99-109.

Brown, S. A., T. M. Okwuosa, A. Barac and A. S. Volgman (2020). "The Role of Angiotensin-Converting Enzyme Inhibitors and β-Blockers in Primary Prevention of Cardiac Dysfunction in Breast Cancer Patients." Journal of the American Heart Association **9**(2).

Chang, W. H., M. Katsoulis, Y. Y. Tan, S. H. Mueller, K. Green and A. G. Lai (2022). "Late effects of cancer in children, teenagers and young adults: Population-based study on the burden of 183 conditions, in-patient and critical care admissions and years of life lost." Lancet Regional Health-Europe **12**.

Chrischilles, E. A., S. Friedman, D. P. Ritzwoller and J. V. Selby (2017). "Patients, data, and progress in cancer care." Lancet Oncology **18**(11): E624-E625.

Christidi, E. and L. R. Brunham (2021). "Regulated cell death pathways in doxorubicin-induced cardiotoxicity." Cell Death & Disease **12**(4).

Daniele, A. J., V. Gregorietti, D. Costa and T. López-Fernández (2024). "Use of EMPAgliflozin in the prevention of CARDiotoxicity: the EMPACARD - PILOT trial." Cardio-Oncology **10**(1).

Dann, E., N. C. Henderson, S. A. Teichmann, M. D. Morgan and J. C. Marioni (2022). "Differential abundance testing on single-cell data using k-nearest neighbor graphs." Nature Biotechnology **40**(2): 245-+.

Dargani, Z. T. and D. K. Singla (2019). "Embryonic stem cell-derived exosomes inhibit doxorubicin-induced TLR4-NLRP3-mediated cell death-pyroptosis." American Journal of Physiology-Heart and Circulatory Physiology **317**(2): H460-H471.

DeBoer, M. D. (2019). "Assessing and Managing the Metabolic Syndrome in Children and Adolescents." Nutrients **11**(8).

Dhingra, R., V. Margulets, S. R. Chowdhurya, J. Thliveris, D. Jassal, P. Fernyhough, G. W. Dorn and L. A. Kirshenbaum (2014). "Bnip3 mediates doxorubicin-induced cardiac myocyte necrosis and mortality through changes in mitochondrial signaling." Proceedings of the National Academy of Sciences of the United States of America **111**(51): E5537-E5544.

Dhingra, R., I. Rabinovich-Nikitin, S. Rothman, M. Guberman, H. Y. Gang, V. Margulets, D. S. Jassal, K. N. Alagarsamy, S. Dhingra, C. V. Ripoll, F. Billia, A. Diwan, A. Javaheri and L. A. Kirshenbaum (2022). "Proteasomal Degradation of TRAF2 Mediates Mitochondrial Dysfunction in Doxorubicin-Cardiomyopathy." Circulation **146**(12): 934-954.

Ding, M. G., R. Shi, S. L. Cheng, M. Li, D. M. De, C. Y. Liu, X. M. Gu, J. Li, S. M. Zhang, M. Jia, R. Fan, J. M. Pei and F. Fu (2022). "Mfn2-mediated mitochondrial fusion alleviates doxorubicin-induced cardiotoxicity with enhancing its anticancer activity through metabolic switch." Redox Biology **52**.

Dixon, S. J., K. M. Lemberg, M. R. Lamprecht, R. Skouta, E. M. Zaitsev, C. E. Gleason, D. N. Patel, A. J. Bauer, A. M. Cantley, W. S. Yang, B. Morrison and B. R. Stockwell (2012). "Ferroptosis: An Iron-Dependent Form of Nonapoptotic Cell Death." Cell **149**(5): 1060-1072.

Doroshow, J. H. and K. J. A. Davies (1986). "REDOX CYCLING OF ANTHRACYCLINES BY CARDIAC MITOCHONDRIA .2. FORMATION OF SUPEROXIDE ANION, HYDROGEN-PEROXIDE, AND HYDROXYL RADICAL." Journal of Biological Chemistry **261**(7): 3068-3074.

Ewer, M. S. and S. M. Ewer (2015). "Cardiotoxicity of anticancer treatments." Nature Reviews Cardiology **12**(9): 547-558.

Faure, L., R. Soldatov, P. Kharchenko and I. Adameyko (2023). "scFates: a scalable python package for advanced pseudotime and bifurcation analysis from single-cell data." Bioinformatics **39**(1).

Galán-Arriola, C., R. Villena-Gutiérrez, M. I. Higuero-Verdejo, I. A. Díaz-Rengifo, G. Pizarro, G. J. López, A. de Molina-Iracheta, C. Pérez-Martínez, R. D. García, D. González-Calle, M. Lobo, P. L. Sánchez, E. Oliver, R. Córdoba, V. Fuster, J. Sánchez-González and B. Ibanez (2021). "Remote ischaemic preconditioning ameliorates anthracycline-induced cardiotoxicity and preserves mitochondrial integrity." Cardiovascular Research **117**(4): 1132-1143.

Golforoush, P. and M. D. Schneider (2020). "Intensive care for human hearts in pluripotent stem cell models." Npj Regenerative Medicine **5**(1).

Skelly, D. A., Squiers, G. T., McLellan, M. A., Bolisetty, M. T., Robson, P., Rosenthal, N. A. & Pinto, A. R. 2018. Single-Cell Transcriptional Profiling Reveals Cellular Diversity and Intercommunication in the Mouse Heart. *Cell Rep,* 22**,** 600-610.

Wolfien, M., Galow, A. M., Muller, P., Bartsch, M., Brunner, R. M., Goldammer, T., Wolkenhauer, O., Hoeflich, A. & David, R. 2020. Single-Nucleus Sequencing of an Entire Mammalian Heart: Cell Type Composition and Velocity. *Cells,* 9.

Hesse, J., Owenier, C., Lautwein, T., Zalfen, R., Weber, J. F., Ding, Z., Alter, C., Lang, A., Grandoch, M., Gerdes, N., Fischer, J. W., Klau, G. W., Dieterich, C., Kohrer, K. & Schrader, J. 2021. Single-cell transcriptomics defines heterogeneity of epicardial cells and fibroblasts within the infarcted murine heart. *Elife,* 10.

Graeber, S. Y., C. Vitzthum, S. T. Pallenberg, L. Naehrlich, M. Stahl, A. Rohrbach, M. Drescher, R. Minso, F. C. Ringshausen, C. Rueckes-Nilges, J. Klajda, J. Berges, Y. Yu, H. Scheuermann, S. Hirtz, O. Sommerburg, A. M. Dittrich, B. Tümmler and M. A. Mall (2022). "Effects of Elexacaftor/Tezacaftor/Ivacaftor Therapy on CFTR Function in Patients with Cystic Fibrosis and One or Two F508del Alleles." American Journal of Respiratory and Critical Care Medicine **205**(5): 540-549.

Gyöngyösi, M., D. Lukovic, K. Zlabinger, A. Spannbauer, A. Gugerell, N. Pavo, D. Traxler, D. Pik, G. Maurer, A. Jakab, M. Riesenhuber, A. Pircher, J. Winkler and J. Bergler-Klein (2020). "Liposomal doxorubicin attenuates cardiotoxicity via induction of interferon-related DNA damage resistance." Cardiovascular Research **116**(5): 970-982.

Hanna, A. D., A. Lam, S. Tham, A. F. Dulhunty and N. A. Beard (2014). "Adverse Effects of Doxorubicin and Its Metabolic Product on Cardiac RyR2 and SERCA2A." Molecular Pharmacology **86**(4): 438-449.

Hao, Y. H., T. Stuart, M. H. Kowalski, S. Choudhary, P. Hoffman, A. Hartman, A. Srivastava, G. Molla, S. Madad, C. Fernandez-Granda and R. Satija (2024). "Dictionary learning for integrative, multimodal and scalable single-cell analysis." Nature Biotechnology **42**(2).

Hemminki, K., F. Zitricky, A. Försti, T. Tapaninen, A. Hemminki, G. Juliusson and C. U. Niemann (2024). "Complex Relationships between Diagnostics and Survival in Chronic Lymphocytic Leukemia in Denmark, Finland, Norway, and Sweden." Cancers **16**(18).

Henriksen, P. A. (2018). "Anthracycline cardiotoxicity: an update on mechanisms, monitoring and prevention." Heart **104**(12): 971-977.

Hensley, M. L., L. M. Schuchter, C. Lindley, N. J. Meropol, G. I. Cohen, G. Broder, W. J. Gradishar, D. M. Green, R. J. Langdon, B. Mitchell, R. Negrin, T. P. Szatrowski, J. T. Thigpen, D. Von Hoff, T. H. Wasserman, E. P. Winer, D. G. Pfister and O. Amer Soc Clinical (1999). "American Society of Clinical Oncology clinical practice guidelines for the use of chemotherapy and radiotherapy protectants." Journal of Clinical Oncology **17**(10): 3333-3355.

Hiona, A., A. S. Lee, J. Nagendran, X. Y. Xie, A. J. Connolly, R. C. Robbins and J. C. Wu (2011). "Pretreatment with angiotensin-converting enzyme inhibitor improves doxorubicin-induced cardiomyopathy via preservation of mitochondrial function." Journal of Thoracic and Cardiovascular Surgery **142**(2): 396-U529.

Ichikawa, Y., M. Ghanefar, M. Bayeva, R. X. Wu, A. Khechaduri, S. V. N. Prasad, R. K. Mutharasan, T. J. Naik and H. Ardehali (2014). "Cardiotoxicity of doxorubicin is mediated through mitochondrial iron accumulation." Journal of Clinical Investigation **124**(2): 617-630.

Jin, S. Q., C. F. Guerrero-Juarez, L. H. Zhang, I. Chang, R. Ramos, C. H. Kuan, P. Myung, M. V. Plikus and Q. Nie (2021). "Inference and analysis of cell-cell communication using CellChat." Nature Communications **12**(1).

Junttila, S., J. Smolander and L. L. Elo (2022). "Benchmarking methods for detecting differential states between conditions from multi-subject single-cell RNA-seq data." Briefings in Bioinformatics **23**(5).

K M Tewey, T. C. R., L Yang, B D Halligan, L F Liu (1984). "Adriamycin-induced DNA damage mediated by mammalian DNA topoisomerase II." Science.

Kalivendi, S. V., E. A. Konorev, S. Cunningham, S. K. Vanamala, E. H. Kaji, J. Joseph and B. Kalyanaraman (2005). "Doxorubicin activates nuclear factor of activated T-lymphocytes and Fas ligand transcription: role of mitochondrial reactive oxygen species and calcium." Biochemical Journal **389**: 527-539.

Kanemaru, K., J. Cranley, D. Muraro, A. M. A. Miranda, S. Y. Ho, A. Wilbrey-Clark, J. P. Pett, K. Polanski, L. Richardson, M. Litvinukova, N. Kumasaka, Y. Qin, Z. Jablonska, C. I. Semprich, L. Mach, M. Dabrowska, N. Richoz, L. Bolt, L. Mamanova, R. Kapuge, S. N. Barnett, S. Perera, C. Talavera-Lopez, I. Mulas, K. T. Mahbubani, L. Tuck, L. Wang, M. M. Huang, M. Prete, S. Pritchard, J. Dark, K. Saeb-Parsy, M. Patel, M. R. Clatworthy, N. Hübner, R. A. Chowdhury, M. Noseda and S. A. Teichmann (2023). "Spatially resolved multiomics of human cardiac niches." Nature **619**(7971): 801-+.

Kciuk, M., A. Gielecinska, S. Mujwar, D. Kolat, Z. Kaluzinska-Kolat, I. Celik and R. Kontek (2023). "Doxorubicin-An Agent with Multiple Mechanisms of Anticancer Activity." Cells **12**(4).

Keizer, H. G., H. M. Pinedo, G. J. Schuurhuis and H. Joenje (1990). "DOXORUBICIN (ADRIAMYCIN) - A CRITICAL-REVIEW OF FREE RADICAL-DEPENDENT MECHANISMS OF CYTOTOXICITY." Pharmacology & Therapeutics **47**(2): 219-231.

Korsunsky, I., N. Millard, J. Fan, K. Slowikowski, F. Zhang, K. Wei, Y. Baglaenko, M. Brenner, P. R. Loh and S. Raychaudhuri (2019). "Fast, sensitive and accurate integration of single-cell data with Harmony." Nature Methods **16**(12): 1289-+.

Li, M. C., V. Sala, M. C. De Santis, J. Cimino, P. Cappello, N. Pianca, A. Di Bona, J. P. Margaria, M. Martini, E. Lazzarini, F. Pirozzi, L. Rossi, I. Franco, J. Bornbaum, J. Heger, S. Rohrbach, A. Perino, C. G. Tocchetti, B. H. F. Lima, M. M. Teixeira, P. E. Porporato, R. Schulz, A. Angelini, M. Sandri, P. Ameri, S. Sciarretta, R. C. P. Lima, M. Mongillo, T. Zaglia, F. Morello, F. Novelli, E. Hirsch and A. Ghigo (2018). "Phosphoinositide 3-Kinase Gamma Inhibition Protects From Anthracycline Cardiotoxicity and Reduces Tumor Growth." Circulation **138**(7): 696-711.

Lim, C. C., C. Zuppinger, X. X. Guo, G. M. Kuster, M. Helmes, H. M. Eppenberger, T. M. Suter, R. L. Liao and D. B. Sawyer (2004). "Anthracyclines induce calpain-dependent titin proteolysis and necrosis in cardiomyocytes." Journal of Biological Chemistry **279**(9): 8290-8299.

Litvinukova, M., C. Talavera-López, H. Maatz, D. Reichart, C. L. Worth, E. L. Lindberg, M. Kanda, K. Polanski, M. Heinig, M. Lee, E. R. Nadelmann, K. Roberts, L. Tuck, E. S. Fasouli, D. M. DeLaughter, B. McDonough, H. Wakimoto, J. M. Gorham, S. Samari, K. T. Mahbubani, K. Saeb-Parsy, G. Patone, J. J. Boyle, H. B. Zhang, H. Zhang, A. Viveiros, G. Y. Oudit, O. A. Bayraktar, J. G. Seidman, C. E. Seidman, M. Noseda, N. Hubner and S. A. Teichmann (2020). "Cells of the adult human heart." Nature **588**(7838): 466-+.

López-Sendón, J., C. Alvarez-Ortega, P. Z. Auñon, A. B. Soto, A. R. Lyon, D. Farmakis, D. Cardinale, M. C. Albendea, J. F. Batlle, I. R. Rodríguez, O. R. Fraga, A. Albaladejo, G. Mediavilla, J. R. González-Juanatey, A. M. Monzonis, P. G. Prieto, J. González-Costello, J. M. S. Antolín, R. C. Chamorro, T. L. Fernández and C. R. Investigators (2020). "Classification, prevalence, and outcomes of anticancer therapy-induced cardiotoxicity: the CARDIOTOX registry." European Heart Journal **41**(18): 1720-+.

Lyon, A. R., T. López-Fernández, L. S. Couch, R. Asteggiano, M. C. Aznar, J. Bergler-Klein, G. Boriani, D. Cardinale, R. Cordoba, B. Cosyns, D. J. Cutter, E. De Azambuja, R. A. De Boer, S. F. Dent, D. Farmakis, S. A. Gevaert, D. A. Gorog, J. Herrmann, D. Lenihan, J. Moslehi, B. Moura, S. S. Salinger, R. Stephens, T. M. Suter, S. Szmit, J. Tamargo, P. Thavendiranathan, C. G. Tocchetti, P. Van der Meer, H. J. H. Van der Pal and E. S. C. S. D. Grp (2022). "2022 ESC Guidelines on cardio-oncology developed in collaboration with the European Hematology Association (EHA), the European Society for Therapeutic Radiology and Oncology (ESTRO) and the International Cardio-Oncology Society (IC-OS) Developed by the task force on cardio-oncology of the European Society of Cardiology (ESC)." European Heart Journal-Cardiovascular Imaging **23**(10): E333-E465.

Lyu, Y. L., J. E. Kerrigan, C. P. Lin, A. M. Azarova, Y. C. Tsai, Y. Ban and L. F. Liu (2007). "Topoisomerase IIβ-Mediated DNA double-strand breaks:: Implications in doxorubicin cardiotoxicity and prevention by dexrazoxane." Cancer Research **67**(18): 8839-8846.

Makwana, V., J. Karanjia, T. Haselhorst, S. Anoopkumar-Dukie and S. Rudrawar (2021). "Liposomal doxorubicin as targeted delivery platform: Current trends in surface functionalization." International Journal of Pharmaceutics **593**.

Martin, E., A. V. Thougaard, M. Grauslund, P. B. Jensen, F. Bjorkling, B. B. Hasinoff, J. Tjornelund, M. Sehested and L. H. Jensen (2009). "Evaluation of the topoisomerase II-inactive bisdioxopiperazine ICRF-161 as a protectant against doxorubicin-induced cardiomyopathy." Toxicology **255**(1-2): 72-79.

Meng, L. P., H. Lin, J. Zhang, N. Lin, Z. Z. Sun, F. D. Gao, H. Q. Luo, T. J. Ni, W. Q. Luo, J. F. Chi and H. Y. Guo (2019). "Doxorubicin induces cardiomyocyte pyroptosis via the TINCR-mediated posttranscriptional stabilization of NLR family pyrin domain containing 3." Journal of Molecular and Cellular Cardiology **136**: 15-26.

Moreno-Arciniegas, A., A. García, M. Kelm, F. D'Amore, M. G. da Silva, J. Sánchez-González, P. L. Sánchez, T. López-Fernández, R. Córdoba, R. Asteggiano, V. Camus, J. Smink, A. Ferreira, M. J. Kersten, N. Bolaños, N. Escalera, E. Pacella, S. Gómez-Talavera, A. Quesada, X. Rosselló, B. Ibanez and R. T. Investigators (2024). "Rationale and design of RESILIENCE: A prospective randomized clinical trial evaluating remote ischaemic conditioning for the prevention of anthracycline cardiotoxicity." European Journal of Heart Failure **26**(10): 2213-2222.

Moslehi, J. J. (2016). "Cardiovascular Toxic Effects of Targeted Cancer Therapies." New England Journal of Medicine **375**(15): 1457-1467.

Nakamura, T., Y. Ueda, Y. Juan, S. Katsuda, H. Takahashi and E. Koh (2000). "Fas-mediated apoptosis in Adriamycin-induced cardiomyopathy in rats - In vivo study." Circulation **102**(5): 572-578.

Paik, D. T., L. Tian, I. M. Williams, S. Rhee, H. Zhang, C. Liu, R. Mishra, S. M. Wu, K. Red-Horse and J. C. Wu (2020). "Single-Cell RNA Sequencing Unveils Unique Transcriptomic Signatures of Organ-Specific Endothelial Cells." Circulation **142**(19): 1848-1862.

Quagliariello, V., M. De Laurentiis, D. Rea, A. Barbieri, M. G. Monti, A. Carbone, A. Paccone, L. Altucci, M. Conte, M. L. Canale, G. Botti and N. Maurea (2021). "The SGLT-2 inhibitor empagliflozin improves myocardial strain, reduces cardiac fibrosis and pro-inflammatory cytokines in non-diabetic mice treated with doxorubicin." Cardiovascular Diabetology **20**(1).

Ramin, C., M. L. Schaeffer, Z. H. Zheng, A. E. Connor, J. Hoffman-Bolton, B. Lau and K. Visvanathan (2021). "All-Cause and Cardiovascular Disease Mortality Among Breast Cancer Survivors in CLUE II, a Long-Standing Community-Based Cohort." Jnci-Journal of the National Cancer Institute **113**(2): 137-145.

Rawat, P. S., A. Jaiswal, A. Khurana, J. S. Bhatti and U. Navik (2021). "Doxorubicin-induced cardiotoxicity: An update on the molecular mechanism and novel therapeutic strategies for effective management." Biomedicine & Pharmacotherapy **139**.

Regev, A., S. A. Teichmann, E. S. Lander, I. Amt, C. Benoist, E. Birney, B. Bodenmiller, P. Campbell, P. Carninci, M. Clatworthy, H. Clevers, B. Deplancke, I. Dunham, J. Eberwine, R. Elis, W. Enard, A. Farmer, L. Fugger, B. Göttgens, N. Hacohen, M. Haniffa, M. Hemberg, S. Kim, P. Klenerman, A. Kriegstein, E. D. Lein, S. Linnarsson, E. Lundberg, J. Lundeberg, P. Majumder, J. C. Marioni, M. Merad, M. Mhlanga, M. Nawijin, M. Netea, G. Nolan, D. Pe'er, A. Phillipakis, C. P. Ponting, S. Quake, W. Reik, O. Rozenblatt-Rosen, J. Sanes, R. Satija, T. N. Schumacher, A. Shalek, E. Shapiro, P. Sharma, J. W. Shin, O. Stegle, M. Stratton, M. J. T. Stubbington, F. J. Theis, M. Uhlen, A. Van Oudenaarden, A. Wagner, F. Watt, J. Weissman, B. Wold, R. Xavier, N. Yosef and M. Human Cell Atlas (2017). "The Human Cell Atlas." Elife **6**.

Reichart, D., E. L. Lindberg, H. Maatz, A. M. A. Miranda, A. Viveiros, N. Shvetsov, A. Gärtner, E. R. Nadelmann, M. Lee, K. Kanemaru, J. Ruiz-Orera, V. Strohmenger, D. M. DeLaughter, G. Patone, H. Zhang, A. Woehler, C. Lippert, Y. Kim, E. Adami, J. M. Gorham, S. N. Barnett, K. Brown, R. J. Buchan, R. A. Chowdhury, C. Constantinou, J. Cranley, L. E. Felkin, H. Fox, A. Ghauri, J. Gummert, M. Kanda, R. Y. Li, L. Mach, B. McDonough, S. Samari, F. Shahriaran, C. Yapp, C. Stanasiuk, P. Theotokis, F. J. Theis, A. van den Bogaerdt, H. Wakimoto, J. S. Ware, C. L. Worth, P. J. R. Barton, Y. A. Lee, S. A. Teichmann, H. Milting, M. Noseda, G. Y. Oudit, M. Heinig, J. G. Seidman, N. Hubner and C. E. Seidman (2022). "Pathogenic variants damage cell composition and single-cell transcription in cardiomyopathies." Science **377**(6606): 619-+.

Wang, L., P. Yu, B. Y. Zhou, J. P. Song, Z. Li, M. Z. Zhang, G. R. Guo, Y. Wang, X. Chen, L. Han and S. S. Hu (2020). "Single-cell reconstruction of the adult human heart during heart failure and recovery reveals the cellular landscape underlying cardiac function." Nature Cell Biology 22(1): 108-+.

Saeki, K., I. Obi, N. Ogiku, M. Shigekawa, T. Imagawa and T. Matsumoto (2002). "Doxorubicin directly binds to the cardiac-type ryanodine receptor." Life Sciences **70**(20): 2377-2389.

Sawicki, K. T., V. Sala, L. Prever, E. Hirsch, H. Ardehali and A. Ghigo (2021). Preventing and Treating Anthracycline Cardiotoxicity: New Insights. Annual Review of Pharmacology and Toxicology, Vol 61, 2021. P. A. Insel. **61:** 309-332.

Shahid, I., N. Yamani, A. Ali, P. Kumar, V. Figueredo, S. Unzek and F. Mookadam (2021). "Meta-analysis Evaluating the Use of Statins to attenuate Cardiotoxicity in Cancer Patients receiving Anthracyclines and Trastuzumab-based Chemotherapy." American Journal of Cardiology **156**: 142-145.

Siegel, R. L., K. D. Miller, N. S. Wagle and A. Jemal (2023). "Cancer statistics, 2023." Ca-a Cancer Journal for Clinicians **73**(1): 17-48.

Spallarossa, P., S. Garibaldi, P. Altieri, P. Fabbi, V. Manca, S. Nasti, P. Rossettin, G. Ghigliotti, A. Ballestrero, F. Patrone, A. Barsotti and C. Brunelli (2004). "Carvedilol prevents doxorubicin-induced free radical release and apoptosis in cardiomyocytes in vitro." Journal of Molecular and Cellular Cardiology **37**(4): 837-846.

Tadokoro, T., M. Ikeda, T. Ide, H. Deguchi, S. Ikeda, K. Okabe, A. Ishikita, S. Matsushima, T. Koumura, K. Yamada, H. Imai and H. Tsutsui (2020). "Mitochondria-dependent ferroptosis plays a pivotal role in doxorubicin cardiotoxicity." Jci Insight **5**(9).

Tan, K. B., T. E. Dorman, K. M. Falls, T. D. Y. Chung, C. K. Mirabelli, S. T. Crooke and J. Mao (1992). "TOPOISOMERASE-II-ALPHA AND TOPOISOMERASE-II-BETA GENES - CHARACTERIZATION AND MAPPING TO HUMAN CHROMOSOME-17 AND CHROMOSOME-3, RESPECTIVELY." Cancer Research **52**(1): 231-234.

Tarantino, P. and S. Tolaney (2024). "Progress in breast cancer management." Lancet **404**(10461): 1376-1378.

Tonorezos, E. S. and V. Marcil (2023). "Childhood cancer survivors: healthy behaviours and late mortality." Lancet **401**(10386): 1403-1405.

Tucker, N. R., M. Chaffin, S. J. Fleming, A. W. Hall, V. A. Parsons, K. C. Bedi, A. D. Akkad, C. N. Herndon, A. Arduini, I. Papangeli, C. Roselli, F. Aguet, S. H. Choi, K. G. Ardlie, M. Babadi, K. B. Margulies, C. M. Stegmann and P. T. Ellinor (2020). "Transcriptional and Cellular Diversity of the Human Heart." Circulation **142**(5): 466-482.

Van Ravenstein, S. X., K. P. Mehta, T. Kavlashvili, J. A. W. Byl, R. X. Zhao, N. Osheroff, D. Cortez and J. M. Dewar (2022). "Topoisomerase II poisons inhibit vertebrate DNA replication through distinct mechanisms." Embo Journal **41**(12).

Vejpongsa, P. and E. T. H. Yeh (2014). "Prevention of Anthracycline-Induced Cardiotoxicity." Journal of the American College of Cardiology **64**(9): 938-945.

Wallace, K. B., V. A. Sardao and P. J. Oliveira (2020). "Mitochondrial Determinants of Doxorubicin-Induced Cardiomyopathy." Circulation Research **126**(7): 926-941.

Wilcox, N. S., U. Amit, J. B. Reibel, E. Berlin, K. Howell and B. Ky (2024). "Cardiovascular disease and cancer: shared risk factors and mechanisms." Nature Reviews Cardiology **21**(9): 617-631.

Wolf, F. A., P. Angerer and F. J. Theis (2018). "SCANPY: large-scale single-cell gene expression data analysis." Genome Biology **19**.

Wolock, S. L., R. Lopez and A. M. Klein (2019). "Scrublet: Computational Identification of Cell Doublets in Single-Cell Transcriptomic Data." Cell Systems **8**(4): 281-+.

Wu, L., L. T. Wang, Y. X. Du, Y. M. Zhang and J. Ren (2023). "Mitochondrial quality control mechanisms as therapeutic targets in doxorubicin-induced cardiotoxicity." Trends in Pharmacological Sciences **44**(1): 34-49.

Xu, X. X., H. L. Persson and D. R. Richardson (2005). "Molecular pharmacology of the interaction of anthracyclines with iron." Molecular Pharmacology **68**(2): 261-271.

Yu, X. X., Y. Ruan, X. Q. Huang, L. Dou, M. Lan, J. Cui, B. D. Chen, H. Gong, Q. Wang, M. J. Yan, S. H. Sun, Q. Qiu, X. Y. Zhang, Y. Man, W. Q. Tang, J. Li and T. Shen (2020). "Dexrazoxane ameliorates doxorubicin-induced cardiotoxicity by inhibiting both apoptosis and necroptosis in cardiomyocytes." Biochemical and Biophysical Research Communications **523**(1): 140-146.

Zhang, S., X. B. Liu, T. Bawa-Khalfe, L. S. Lu, Y. L. Lyu, L. F. Liu and E. T. H. Yeh (2012). "Identification of the molecular basis of doxorubicin-induced cardiotoxicity." Nature Medicine **18**(11): 1639-+.

Zhang, T., Y. Zhang, M. Y. Cui, L. Jin, Y. M. Wang, F. X. Lv, Y. L. Liu, W. Zheng, H. B. Shang, J. Zhang, M. Zhang, H. K. Wu, J. J. Guo, X. Q. Zhang, X. L. Hu, C. M. Cao and R. P. Xiao (2016). "CaMKII is a RIP3 substrate mediating ischemia- and oxidative stress-induced myocardial necroptosis." Nature Medicine **22**(2): 175-182.

Zhang, X. P., F. Liu and W. Wang (2012). "Regulation of the DNA Damage Response by p53 Cofactors." Biophysical Journal **102**(10): 2251-2260.

Zheng, G. X. Y., J. M. Terry, P. Belgrader, P. Ryvkin, Z. W. Bent, R. Wilson, S. B. Ziraldo, T. D. Wheeler, G. P. McDermott, J. J. Zhu, M. T. Gregory, J. Shuga, L. Montesclaros, J. G. Underwood, D. A. Masquelier, S. Y. Nishimura, M. Schnall-Levin, P. W. Wyatt, C. M. Hindson, R. Bharadwaj, A. Wong, K. D. Ness, L. W. Beppu, H. J. Deeg, C. McFarland, K. R. Loeb, W. J. Valente, N. G. Ericson, E. A. Stevens, J. P. Radich, T. S. Mikkelsen, B. J. Hindson and J. H. Bielas (2017). "Massively parallel digital transcriptional profiling of single cells." Nature Communications **8**.

Zheng, M. and T. D. Kanneganti (2020). "The regulation of the ZBP1-NLRP3 inflammasome and its implications in pyroptosis, apoptosis, and necroptosis (PANoptosis)." Immunological Reviews **297**(1): 26-38.

Zhu, Y. J., J. Hu, Y. D. Hu and W. G. Liu (2009). "Targeting DNA repair pathways: A novel approach to reduce cancer therapeutic resistance." Cancer Treatment Reviews **35**(7): 590-596.

Marelli-Berg, F. M., Clement, M., Mauro, C. & Caligiuri, G. 2013. An immunologist's guide to CD31 function in T-cells. *J Cell Sci,* 126**,** 2343-52.

Farbehi, N., Patrick, R., Dorison, A., Xaymardan, M., Janbandhu, V., Wystub-Lis, K., Ho, J. W., Nordon, R. E. & Harvey, R. P. 2019. Single-cell expression profiling reveals dynamic flux of cardiac stromal, vascular and immune cells in health and injury. *Elife,* 8.

Forte, E., Skelly, D. A., Chen, M., Daigle, S., Morelli, K. A., Hon, O., Philip, V. M., Costa, M. W., Rosenthal, N. A. & Furtado, M. B. 2020. Dynamic Interstitial Cell Response during Myocardial Infarction Predicts Resilience to Rupture in Genetically Diverse Mice. *Cell Rep,* 30**,** 3149-3163 e6.

McLellan, M. A., Skelly, D. A., Dona, M. S. I., Squiers, G. T., Farrugia, G. E., Gaynor, T. L., Cohen, C. D., Pandey, R., Diep, H., Vinh, A., Rosenthal, N. A. & Pinto, A. R. 2020. High-Resolution Transcriptomic Profiling of the Heart During Chronic Stress Reveals Cellular Drivers of Cardiac Fibrosis and Hypertrophy. *Circulation,* 142**,** 1448-1463.

Patrick, R., Janbandhu, V., Tallapragada, V., Tan, S. S. M., McKinna, E. E., Contreras, O., Ghazanfar, S., Humphreys, D. T., Murray, N. J., Tran, Y. T. H., Hume, R. D., Chong, J. J. H. & Harvey, R. P. 2024. Integration mapping of cardiac fibroblast single-cell transcriptomes elucidates cellular principles of fibrosis in diverse pathologies. *Sci Adv,* 10**,** eadk8501.

Noseda, M., Harada, M., McSweeney, S., Leja, T., Belian, E., Stuckey, D. J., Abreu Paiva, M. S., Habib, J., Macaulay, I., de Smith, A. J., al-Beidh, F., Sampson, R., Lumbers, R. T., Rao, P., Harding, S. E., Blakemore, A. I., Jacobsen, S. E., Barahona, M. & Schneider, M. D. 2015. PDGFRalpha demarcates the cardiogenic clonogenic Sca1+ stem/progenitor cell in adult murine myocardium. *Nat Commun,* 6**,** 6930.

Regn, M., Laggerbauer, B., Jentzsch, C., Ramanujam, D., Ahles, A., Sichler, S., Calzada-Wack, J., Koenen, R. R., Braun, A., Nieswandt, B. & Engelhardt, S. 2016. Peptidase inhibitor 16 is a membrane-tethered regulator of chemerin processing in the myocardium. *J Mol Cell Cardiol,* 99**,** 57-64.

Surmann-Schmitt, C., Sasaki, T., Hattori, T., Eitzinger, N., Schett, G., von der Mark, K. & Stock, M. 2012. The Wnt antagonist Wif-1 interacts with CTGF and inhibits CTGF activity. *J Cell Physiol,* 227**,** 2207-16.

Tani, H., Sadahiro, T., Yamada, Y., Isomi, M., Yamakawa, H., Fujita, R., Abe, Y., Akiyama, T., Nakano, K., Kuze, Y., Seki, M., Suzuki, Y., Fujisawa, M., Sakata-Yanagimoto, M., Chiba, S., Fukuda, K. & Ieda, M. 2023. Direct Reprogramming Improves Cardiac Function and Reverses Fibrosis in Chronic Myocardial Infarction. *Circulation,* 147**,** 223-238.

Alexanian, M., Przytycki, P. F., Micheletti, R., Padmanabhan, A., Ye, L., Travers, J. G., Gonzalez-Teran, B., Silva, A. C., Duan, Q., Ranade, S. S., Felix, F., Linares-Saldana, R., Li, L., Lee, C. Y., Sadagopan, N., Pelonero, A., Huang, Y., Andreoletti, G., Jain, R., McKinsey, T. A., Rosenfeld, M. G., Gifford, C. A., Pollard, K. S., Haldar, S. M. & Srivastava, D. 2021. A transcriptional switch governs fibroblast activation in heart disease. *Nature,* 595**,** 438-443.

Zhang, Q. J., He, Y., Li, Y., Shen, H., Lin, L., Zhu, M., Wang, Z., Luo, X., Hill, J. A., Cao, D., Luo, R. L., Zou, R., McAnally, J., Liao, J., Bajona, P., Zang, Q. S., Yu, Y. & Liu, Z. P. 2021. Matricellular Protein Cilp1 Promotes Myocardial Fibrosis in Response to Myocardial Infarction. *Circ Res,* 129**,** 1021-1035.

Younesi, F. S., Son, D. O., Firmino, J. & Hinz, B. 2021. Myofibroblast Markers and Microscopy Detection Methods in Cell Culture and Histology. *Methods Mol Biol,* 2299**,** 17-47.

Ruiz-Villalba, A., Romero, J. P., Hernandez, S. C., Vilas-Zornoza, A., Fortelny, N., Castro-Labrador, L., San Martin-Uriz, P., Lorenzo-Vivas, E., Garcia-Olloqui, P., Palacio, M., Gavira, J. J., Bastarrika, G., Janssens, S., Wu, M., Iglesias, E., Abizanda, G., de Morentin, X. M., Lasaga, M., Planell, N., Bock, C., Alignani, D., Medal, G., Prudovsky, I., Jin, Y. R., Ryzhov, S., Yin, H., Pelacho, B., Gomez-Cabrero, D., Lindner, V., Lara-Astiaso, D. & Prosper, F. 2020. Single-Cell RNA Sequencing Analysis Reveals a Crucial Role for CTHRC1 (Collagen Triple Helix Repeat Containing 1) Cardiac Fibroblasts After Myocardial Infarction. *Circulation,* 142**,** 1831-1847.

Aldeiri, B., Roostalu, U., Albertini, A., Wong, J., Morabito, A. & Cossu, G. 2017. Transgelin-expressing myofibroblasts orchestrate ventral midline closure through TGFbeta signalling. *Development,* 144**,** 3336-3348.

Sun, C., Zhang, K., Ni, C., Wan, J., Duan, X., Lou, X., Yao, X., Li, X., Wang, M., Gu, Z., Yang, P., Li, Z. & Qin, Z. 2023. Transgelin promotes lung cancer progression via activation of cancer-associated fibroblasts with enhanced IL-6 release. *Oncogenesis,* 12**,** 18.

Sandbo, N. & Dulin, N. 2011. Actin cytoskeleton in myofibroblast differentiation: ultrastructure defining form and driving function. *Transl Res,* 158**,** 181-96.

Li, Q., Tintut, Y., Demer, L. L., Vazquez-Padron, R. I., Bendeck, M. P. & Hsu, J. J. 2024. Collagen VIII in Vascular Diseases. *Matrix Biol*.

Jin, C., Chen, Y., Wang, Y., Li, J., Liang, J., Zheng, S., Zhang, L., Li, Q., Wang, Y., Ling, F., Li, Y., Zheng, Y., Nie, Q., Feng, Q., Wang, J. & Yang, H. 2024. Single-cell RNA sequencing reveals special basal cells and fibroblasts in idiopathic pulmonary fibrosis. *Sci Rep,* 14**,** 15778.

Zhao, H., Wang, L., Yan, Y., Zhao, Q. H., He, J., Jiang, R., Luo, C. J., Qiu, H. L., Miao, Y. Q., Gong, S. G., Yuan, P. & Wu, W. H. 2023. Identification of the shared gene signatures between pulmonary fibrosis and pulmonary hypertension using bioinformatics analysis. *Front Immunol,* 14**,** 1197752.

Watanabe, T., Baker Frost, D. A., Mlakar, L., Heywood, J., da Silveira, W. A., Hardiman, G. & Feghali-Bostwick, C. 2019. A Human Skin Model Recapitulates Systemic Sclerosis Dermal Fibrosis and Identifies COL22A1 as a TGFbeta Early Response Gene that Mediates Fibroblast to Myofibroblast Transition. *Genes (Basel),* 10.

Bhattacharyya, S., Midwood, K. S. & Varga, J. 2022. Tenascin-C in fibrosis in multiple organs: Translational implications. *Semin Cell Dev Biol,* 128**,** 130-136.

Belmadani, S., Bernal, J., Wei, C. C., Pallero, M. A., Dell'italia, L., Murphy-Ullrich, J. E. & Berecek, K. H. 2007. A thrombospondin-1 antagonist of transforming growth factor-beta activation blocks cardiomyopathy in rats with diabetes and elevated angiotensin II. *Am J Pathol,* 171**,** 777-89.

Jin, S., Guerrero-Juarez, C. F., Zhang, L., Chang, I., Ramos, R., Kuan, C. H., Myung, P., Plikus, M. V. & Nie, Q. 2021. Inference and analysis of cell-cell communication using CellChat. *Nat Commun,* 12**,** 1088.

Frieler, R. A. & Mortensen, R. M. 2015. Immune cell and other noncardiomyocyte regulation of cardiac hypertrophy and remodeling. *Circulation,* 131**,** 1019-30.

Kaur, H., Takefuji, M., Ngai, C. Y., Carvalho, J., Bayer, J., Wietelmann, A., Poetsch, A., Hoelper, S., Conway, S. J., Mollmann, H., Looso, M., Troidl, C., Offermanns, S. & Wettschureck, N. 2016. Targeted Ablation of Periostin-Expressing Activated Fibroblasts Prevents Adverse Cardiac Remodeling in Mice. *Circ Res,* 118**,** 1906-17.

Hoelper, S., Conway, S. J., Mollmann, H., Looso, M., Troidl, C., Offermanns, S. & Wettschureck, N. 2016. Targeted Ablation of Periostin-Expressing Activated Fibroblasts Prevents Adverse Cardiac Remodeling in Mice. *Circ Res,* 118**,** 1906-17.

Hakuno, D., Kimura, N., Yoshioka, M., Mukai, M., Kimura, T., Okada, Y., Yozu, R., Shukunami, C., Hiraki, Y., Kudo, A., Ogawa, S. & Fukuda, K. 2010. Periostin advances atherosclerotic and rheumatic cardiac valve degeneration by inducing angiogenesis and MMP production in humans and rodents. *J Clin Invest,* 120**,** 2292-306.

Frieler, R. A. & Mortensen, R. M. 2015. Immune cell and other noncardiomyocyte regulation of cardiac hypertrophy and remodeling. *Circulation,* 131**,** 1019-30.

Roy, S., Spinali, K., Schmuck, E. G., Kink, J. A., Hematti, P. & Raval, A. N. 2020. Cardiac fibroblast derived matrix-educated macrophages express VEGF and IL-6, and recruit mesenchymal stromal cells. *J Immunol Regen Med,* 10.

Rogers, N. M., Sharifi-Sanjani, M., Yao, M., Ghimire, K., Bienes-Martinez, R., Mutchler, S. M., Knupp, H. E., Baust, J., Novelli, E. M., Ross, M., St Croix, C., Kutten, J. C., Czajka, C. A., Sembrat, J. C., Rojas, M., Labrousse-Arias, D., Bachman, T. N., Vanderpool, R. R.,

Vanhoutte, D., Schips, T. G., Vo, A., Grimes, K. M., Baldwin, T. A., Brody, M. J., Accornero, F., Sargent, M. A. & Molkentin, J. D. 2021. Thbs1 induces lethal cardiac atrophy through PERK-ATF4 regulated autophagy. *Nat Commun,* 12**,** 3928.

Gao, Q., Chen, K., Gao, L., Zheng, Y. & Yang, Y. G. 2016. Thrombospondin-1 signaling through CD47 inhibits cell cycle progression and induces senescence in endothelial cells. *Cell Death Dis,* 7**,** e2368.

Epelman, S., Lavine, K. J., Beaudin, A. E., Sojka, D. K., Carrero, J. A., Calderon, B., Brija, T., Gautier, E. L., Ivanov, S., Satpathy, A. T., Schilling, J. D., Schwendener, R., Sergin, I., Razani, B., Forsberg, E.

C., Yokoyama, W. M., Unanue, E. R., Colonna, M., Randolph, G. J. & Mann, D. L. 2014a. Embryonic and adult-derived resident cardiac macrophages are maintained through distinct mechanisms at steady state and during inflammation. *Immunity,* 40**,** 91-10 Dick, S. A., Macklin, J. A., Nejat, S., Momen, A., Clemente-Casares, X., Althagafi, M. G., Chen, J., Kantores, C., Hosseinzadeh, S., Aronoff, L., Wong, A., Zaman, R., Barbu, I., Besla, R., Lavine, K. J., Razani, B., Ginhoux, F., Husain, M., Cybulsky, M. I., Robbins, C. S. & Epelman, S. 2019. Self-renewing resident cardiac macrophages limit adverse remodeling following myocardial infarction. *Nat Immunol,* 20**,** 29-39.

Dick, S. A., Wong, A., Hamidzada, H., Nejat, S., Nechanitzky, R., Vohra, S., Mueller, B., Zaman, R., Kantores, C., Aronoff, L., Momen, A., Nechanitzky, D., Li, W. Y., Ramachandran, P., Crome, S. Q., Becher, B., Cybulsky, M. I., Billia, F., Keshavjee, S., Mital, S., Robbins, C. S., Mak, T. W. & Epelman, S. 2022. Three tissue resident macrophage subsets coexist across organs with conserved origins and life cycles. *Sci Immunol,* 7**,** eabf7777.

Dick, S. A., Macklin, J. A., Nejat, S., Momen, A., Clemente-Casares, X., Althagafi, M. G., Chen, J., Kantores, C., Hosseinzadeh, S., Aronoff, L., Wong, A., Zaman, R., Barbu, I., Besla, R., Lavine, K. J., Razani, B., Ginhoux, F., Husain, M., Cybulsky, M. I., Robbins, C. S. & Epelman, S. 2019. Self-renewing resident cardiac macrophages limit adverse remodeling following myocardial infarction. *Nat Immunol,* 20**,** 29-39.

Revelo, X. S., Parthiban, P., Chen, C., Barrow, F., Fredrickson, G., Wang, H., Yucel, D., Herman, A. & van Berlo, J. H. 2021. Cardiac Resident Macrophages Prevent Fibrosis and Stimulate Angiogenesis. *Circ Res,* 129**,** 1086-1101.

Heinen, A., Nederlof, R., Panjwani, P., Spychala, A., Tschaidse, T., Reffelt, H., Boy, J., Raupach, A., Godecke, S., Petzsch, P., Kohrer, K., Grandoch, M., Petz, A., Fischer, J. W., Alter, C., Vasilevska, J., Lang, P. & Godecke, A. 2019. IGF1 Treatment Improves Cardiac Remodeling after Infarction by Targeting Myeloid Cells. *Mol Ther,* 27**,** 46-58.

Nederlof, R., Reidel, S., Spychala, A., Godecke, S., Heinen, A., Lautwein, T., Petzsch, P., Kohrer, K. & Godecke, A. 2022. Insulin-Like Growth Factor 1 Attenuates the Pro-Inflammatory Phenotype of Neutrophils in Myocardial Infarction. *Front Immunol,* 13**,** 908023.

Karadimou, G., Plunde, O., Pawelzik, S. C., Carracedo, M., Eriksson, P., Franco-Cereceda, A., Paulsson-Berne, G. & Back, M. 2020. TLR7 Expression Is Associated with M2 Macrophage Subset in Calcific Aortic Valve Stenosis. *Cells,* 9.

Chakarov, S., Lim, H. Y., Tan, L., Lim, S. Y., See, P., Lum, J., Zhang, X. M., Foo, S., Nakamizo, S., Duan, K., Kong, W. T., Gentek, R., Balachander, A., Carbajo, D., Bleriot, C., Malleret, B., Tam, J. K. C., Baig, S., Shabeer, M., Toh, S. E. S., Schlitzer, A., Larbi, A., Marichal, T., Malissen, B., Chen, J., Poidinger, M., Kabashima, K., Bajenoff, M., Ng, L. G., Angeli, V. & Ginhoux, F. 2019. Two distinct interstitial macrophage populations coexist across tissues in specific subtissular niches. *Science,* 363.

Bajpai, G., Bredemeyer, A., Li, W., Zaitsev, K., Koenig, A. L., Lokshina, I., Mohan, J., Ivey, B., Hsiao, H. M., Weinheimer, C., Kovacs, A., Epelman, S., Artyomov, M., Kreisel, D. & Lavine, K. J. 2019. Tissue Resident CCR2- and CCR2+ Cardiac Macrophages Differentially Orchestrate Monocyte Recruitment and Fate Specification Following Myocardial Injury. *Circ Res,* 124**,** 263-278.

Gong, S., Zhai, M., Shi, J., Yu, G., Lei, Z., Shi, Y., Zeng, Y., Ju, P., Yang, N., Zhang, Z., Zhang, D., Zhuang, J., Yu, Q., Zhang, X., Jian, W., Wang, W. & Peng, W. 2024. TREM2 macrophage promotes cardiac repair in myocardial infarction by reprogramming metabolism via SLC25A53. *Cell Death Differ,* 31**,** 239-253.

Valiente-Alandi, I., Potter, S. J., Salvador, A. M., Schafer, A. E., Schips, T., Carrillo-Salinas, F., Gibson, A. M., Nieman, M. L., Perkins, C., Sargent, M. A., Huo, J., Lorenz, J. N., DeFalco, T., Molkentin, J. D., Alcaide, P. & Blaxall, B. C. 2018. Inhibiting Fibronectin Attenuates Fibrosis and Improves Cardiac Function in a Model of Heart Failure. *Circulation,* 138**,** 1236-1252.

Sawaki, D., Czibik, G., Pini, M., Ternacle, J., Suffee, N., Mercedes, R., Marcelin, G., Surenaud, M., Marcos, E., Gual, P., Clement, K., Hue, S., Adnot, S., Hatem, S. N., Tsuchimochi, I., Yoshimitsu, T., Henegar, C. & Derumeaux, G. 2018. Visceral Adipose Tissue Drives Cardiac Aging Through Modulation of Fibroblast Senescence by Osteopontin Production. *Circulation,* 138**,** 809-822.

Gao, F., Liang, T., Lu, Y. W., Pu, L., Fu, X., Dong, X., Hong, T., Zhang, F., Liu, N., Zhou, Y., Wang, H., Liang, P., Guo, Y., Yu, H., Zhu, W., Hu, X., Chen, H., Zhou, B., Pu, W. T., Mably, J. D., Wang, J., Wang,

D. Z. & Chen, J. 2023. Reduced Mitochondrial Protein Translation Promotes Cardiomyocyte Proliferation and Heart Regeneration. *Circulation,* 148**,** 1887-1906.

Guilliams, M., Ginhoux, F., Jakubzick, C., Naik, S. H., Onai, N., Schraml, B. U., Segura, E., Tussiwand, R. & Yona, S. 2014. Dendritic cells, monocytes and macrophages: a unified nomenclature based on ontogeny. *Nat Rev Immunol,* 14**,** 571-8.

Piva, L., Tetlak, P., Claser, C., Karjalainen, K., Renia, L. & Ruedl, C. 2012. Cutting edge: Clec9A+ dendritic cells mediate the development of experimental cerebral malaria. *J Immunol,* 189**,** 1128-32.

Satpathy, A. T., Kc, W., Albring, J. C., Edelson, B. T., Kretzer, N. M., Bhattacharya, D., Murphy, T. L. & Murphy, K. M. 2012. Zbtb46 expression distinguishes classical dendritic cells and their committed progenitors from other immune lineages. *J Exp Med,* 209**,** 1135-52.

Durai, V. & Murphy, K. M. 2016. Functions of Murine Dendritic Cells. *Immunity,* 45**,** 719-736.

Crozat, K., Guiton, R., Contreras, V., Feuillet, V., Dutertre, C. A., Ventre, E., Vu Manh, T. P., Baranek, T., Storset, A. K., Marvel, J., Boudinot, P., Hosmalin, A., Schwartz-Cornil, I. & Dalod, M. 2010. The XC chemokine receptor 1 is a conserved selective marker of mammalian cells homologous to mouse CD8alpha+ dendritic cells. *J Exp Med,* 207**,** 1283-92.

Jirmo, A. C., Grychtol, R., Gaedcke, S., Liu, B., DeStefano, S., Happle, C., Halle, O., Monteiro,

Brown, C. C., Gudjonson, H., Pritykin, Y., Deep, D., Lavallee, V. P., Mendoza, A., Fromme, R., Mazutis, L., Ariyan, C., Leslie, C., Pe'er, D. & Rudensky, A. Y. 2019. Transcriptional Basis of Mouse and Human Dendritic Cell Heterogeneity. *Cell,* 179**,** 846-863 e24.

Jirmo, A. C., Grychtol, R., Gaedcke, S., Liu, B., DeStefano, S., Happle, C., Halle, O., Monteiro, J. T., Habener, A., Breiholz, O. D., DeLuca, D. & Hansen, G. 2023. Single cell RNA sequencing reveals distinct clusters of Irf8-expressing pulmonary conventional dendritic cells. *Front Immunol,* 14**,** 1127485.

Gargaro, M., Scalisi, G., Manni, G., Briseno, C. G., Bagadia, P., Durai, V., Theisen, D. J., Kim, S., Castelli, M., Xu, C. A., Meyer Zu Horste, G., Servillo, G., Della Fazia, M. A., Mencarelli, G., Ricciuti, D., Padiglioni, E., Giacche, N., Colliva, C., Pellicciari, R., Calvitti, M., Zelante, T., Fuchs, D., Orabona, C., Boon, L., Bessede, A., Colonna, M., Puccetti, P., Murphy, T. L., Murphy, K. M. & Fallarino, F. 2022. Indoleamine 2,3-dioxygenase 1 activation in mature cDC1 promotes tolerogenic education of inflammatory cDC2 via metabolic communication. *Immunity,* 55**,** 1032-1050 e14.

Bajana, S., Turner, S., Paul, J., Ainsua-Enrich, E. & Kovats, S. 2016. IRF4 and IRF8 Act in CD11c+ Cells To Regulate Terminal Differentiation of Lung Tissue Dendritic Cells. *J Immunol,* 196**,** 1666-77.

Sprenkeler, E. G. G., Zandstra, J., van Kleef, N. D., Goetschalckx, I., Verstegen, B., Aarts, C. E. M., Janssen, H., Tool, A. T. J., van Mierlo, G., van Bruggen, R., Jongerius, I. & Kuijpers, T. W. 2022. S100A8/A9 Is a Marker for the Release of Neutrophil Extracellular Traps and Induces Neutrophil Activation. *Cells,* 11.

Geng, R., Zhao, Y., Xu, W., Ma, X., Jiang, Y., Han, X., Zhao, L. & Li, Y. 2024. SIRPB1 regulates inflammatory factor expression in the glioma microenvironment via SYK: functional and bioinformatics insights. *J Transl Med,* 22**,** 338.

Tang, J., Wan, X., Zhang, J., Diao, N., Zhang, C., Gao, X. & Ren, D. 2023. A frameshift variant in the SIRPB1 gene confers susceptibility to Crohn's disease in a Chinese population. *Front Genet,* 14**,** 1130529.

Mori, Y., Kondo, C., Tonomura, Y., Torii, M. & Uehara, T. 2010. Identification of potential genomic biomarkers for early detection of chemically induced cardiotoxicity in rats. *Toxicology,* 271**,** 36-44.

Zahradka, P. 2008. Novel role for osteopontin in cardiac fibrosis. *Circ Res,* 102**,** 270-2.

Hulsmans, M., Schloss, M. J., Lee, I. H., Bapat, A., Iwamoto, Y., Vinegoni, C., Paccalet, A., Yamazoe, M., Grune, J., Pabel, S., Momin, N., Seung, H., Kumowski, N., Pulous, F. E., Keller, D., Bening, C., Green, U., Lennerz, J. K., Mitchell, R. N., Lewis, A., Casadei, B., Iborra-Egea, O., Bayes-Genis, A., Sossalla, S., Ong, C. S., Pierson, R. N., Aster, J. C., Rohde, D., Wojtkiewicz, G. R., Weissleder, R., Swirski, F. K., Tellides, G., Tolis, G., Jr., Melnitchouk, S., Milan, D. J., Ellinor, P. T., Naxerova, K. & Nahrendorf, M. 2023. Recruited macrophages elicit atrial fibrillation. *Science,* 381**,** 231-239.

Yu, S., Zhou, X., Steinke, F. C., Liu, C., Chen, S. C., Zagorodna, O., Jing, X., Yokota, Y., Meyerholz, D. K., Mullighan, C. G., Knudson, C. M., Zhao, D. M. & Xue, H. H. 2012. The TCF-1 and LEF-1 transcription factors have cooperative and opposing roles in T cell development and malignancy. *Immunity,* 37**,** 813-26.

Klement, J. D., Paschall, A. V., Redd, P. S., Ibrahim, M. L., Lu, C., Yang, D., Celis, E., Abrams, S. I., Ozato, K. & Liu, K. 2018. An osteopontin/CD44 immune checkpoint controls CD8+ T cell activation and tumor immune evasion. *J Clin Invest,* 128**,** 5549-5560.

Heinrichs, M., Ashour, D., Siegel, J., Buchner, L., Wedekind, G., Heinze, K. G., Arampatzi, P., Saliba, A. E., Cochain, C., Hofmann, U., Frantz, S. & Campos Ramos, G. 2021. The healing myocardium mobilizes a distinct B-cell subset through a CXCL13-CXCR5-dependent mechanism. *Cardiovasc Res,* 117**,** 2664-2676.

Bayer, A. L., Zambrano, M., Elwell, H., Smolgovsky, S., Kaur, K., Asnani, A. & Alcaide, P. 2023. Cytotoxic T-cells Drive Doxorubicin Induced Cardiac Fibrosis And Systolic Dysfunction. *Circulation Research,* 133.

Bayer, A. L., Zambrano, M. A., Smolgovsky, S., Robbe, Z. L., Ariza, A., Kaur, K., Sawden, M., Avery, A., London, C., Asnani, A. & Alcaide, P. 2024. Cytotoxic T cells drive doxorubicin-induced cardiac fibrosis and systolic dysfunction. *Nat Cardiovasc Res,* 3**,** 970-986.

Choukrani, G., Visser, N., Ustyanovska Avtenyuk, N., Olthuis, M., Marsman, G., Ammatuna, E., Lourens, H. J., Niki, T., Huls, G., Bremer, E. & Wiersma, V. R. 2023. Galectin-9 has non-apoptotic cytotoxic activity toward acute myeloid leukemia independent of cytarabine resistance. *Cell Death Discov,* 9**,** 228.

Itoh, A., Nonaka, Y., Ogawa, T., Nakamura, T. & Nishi, N. 2019. Galectin-9 induces atypical ubiquitination leading to cell death in PC-3 prostate cancer cells. *Glycobiology,* 29**,** 22-35.

Fujita, K., Iwama, H., Oura, K., Tadokoro, T., Samukawa, E., Sakamoto, T., Nomura, T., Tani, J., Yoneyama, H., Morishita, A., Himoto, T., Hirashima, M. & Masaki, T. 2017. Cancer Therapy Due to Apoptosis: Galectin-9. *Int J Mol Sci,* 18.

Satoh, M., Nomura, S., Harada, M., Yamaguchi, T., Ko, T., Sumida, T., Toko, H., Naito, A. T., Takeda, N., Tobita, T., Fujita, T., Ito, M., Fujita, K., Ishizuka, M., Kariya, T., Akazawa, H., Kobayashi, Y., Morita, H., Takimoto, E., Aburatani, H. & Komuro, I. 2019. High-throughput single-molecule RNA imaging analysis reveals heterogeneous responses of cardiomyocytes to hemodynamic overload. *J Mol Cell Cardiol,* 128**,** 77-89.

Man, J., Barnett, P. & Christoffels, V. M. 2018. Structure and function of the Nppa-Nppb cluster locus during heart development and disease. *Cell Mol Life Sci,* 75**,** 1435-1444.

Zhou, H., Li, N., Yuan, Y., Jin, Y. G., Guo, H., Deng, W. & Tang, Q. Z. 2018. Activating transcription factor 3 in cardiovascular diseases: a potential therapeutic target. *Basic Res Cardiol,* 113**,** 37.

Reuter, S. P., Soonpaa, M. H., Field, D., Simpson, E., Rubart-von der Lohe, M., Lee, H. K., Sridhar, A., Ware, S. M., Green, N., Li, X., Ofner, S., Marchuk, D. A., Wollert, K. C. & Field, L. J. 2023. Cardiac Troponin I-Interacting Kinase Affects Cardiomyocyte S-Phase Activity but Not Cardiomyocyte Proliferation. *Circulation,* 147**,** 142-153.

Kim, K. H., Oh, Y., Liu, J., Dababneh, S., Xia, Y., Kim, R. Y., Kim, D. K., Ban, K., Husain, M., Hui, C. C. & Backx, P. H. 2022. Irx5 and transient outward K(+) currents contribute to transmural contractile heterogeneities in the mouse ventricle. *Am J Physiol Heart Circ Physiol,* 322**,** H725-H741.

Bohne, L. J., Jansen, H. J., Daniel, I., Dorey, T. W., Moghtadaei, M., Belke, D. D., Ezeani, M. & Rose, R. A. 2021. Electrical and structural remodeling contribute to atrial fibrillation in type 2 diabetic db/db mice. *Heart Rhythm,* 18**,** 118-129.

Dallabrida, S. M., Ismail, N., Oberle, J. R., Himes, B. E. & Rupnick, M. A. 2005. Angiopoietin-1 promotes cardiac and skeletal myocyte survival through integrins. *Circulation Research,* 96

Ren, D., Zhu, Q., Li, J., Ha, T., Wang, X. & Li, Y. 2012. Overexpression of angiopoietin-1 reduces doxorubicin-induced apoptosis in cardiomyocytes. *J Biomed Res,* 26**,** 432-8.

Goodyer, W. R., Beyersdorf, B. M., Paik, D. T., Tian, L., Li, G., Buikema, J. W., Chirikian, O., Choi, S., Venkatraman, S., Adams, E. L., Tessier-Lavigne, M., Wu, J. C. & Wu, S. M. 2019. Transcriptomic Profiling of the Developing Cardiac Conduction System at Single-Cell Resolution. *Circ Res,* 125**,** 379-397.

Agarwal, R., Paulo, J. A., Toepfer, C. N., Ewoldt, J. K., Sundaram, S., Chopra, A., Zhang, Q., Gorham, J., DePalma, S. R., Chen, C. S., Gygi, S. P., Seidman, C. E. & Seidman, J. G. 2021. Filamin C Cardiomyopathy Variants Cause Protein and Lysosome Accumulation. *Circ Res,* 129**,** 751-766.

Bermudez-Jimenez, F. J., Protonotarios, A., Garcia-Hernandez, S., Perez Asensio, A., Rampazzo, A., Zorio, E., Brodehl, A., Arias, M. A., Macias-Ruiz, R., Fernandez-Armenta, J., Remior Perez, P., Munoz-Esparza, C., Pilichou, K., Bauce, B., Merino, J. L., Moliner-Abos, C., Ochoa, J. P., Barriales-Villa, R., Garcia-Pavia, P., Lopes, L. R., Syrris, P., Corrado, D., Elliott, P. M., McKenna, W. J. & Jimenez-Jaimez, J. 2024. Phenotype and Clinical Outcomes in Desmin-Related Arrhythmogenic Cardiomyopathy. *JACC Clin Electrophysiol,* 10**,** 1178-1190.

Zhao, P., Li, Y., Xu, X., Yang, H., Li, X., Fu, S., Guo, Z., Zhang, J., Li, H. & Tian, J. 2024. Neutrophil extracellular traps mediate cardiomyocyte ferroptosis via the Hippo-Yap pathway to exacerbate doxorubicin-induced cardiotoxicity. *Cell Mol Life Sci,* 81**,** 122.

Leask, A. 2010. Potential therapeutic targets for cardiac fibrosis: TGFbeta, angiotensin, endothelin, CCN2, and PDGF, partners in fibroblast activation. *Circ Res,* 106**,** 1675-80.

Pop-Moldovan, A. L., Trofenciuc, N. M., Darabantiu, D. A., Precup, C., Branea, H., Christodorescu, R. & Puschita, M. 2017. Customized laboratory TLR4 and TLR2 detection method from peripheral human blood for early detection of doxorubicin-induced cardiotoxicity. *Cancer Gene Ther,* 24**,** 203-207.

Hitsumoto, T., Tsukamoto, O., Matsuoka, K., Li, J., Liu, L., Kuramoto, Y., Higo, S., Ogawa, S., Fujino, N., Yoshida, S., Kioka, H., Kato, H., Hakui, H., Saito, Y., Okamoto, C., Inoue, H., Hyejin, J., Ueda, K., Segawa, T., Nishimura, S., Asano, Y., Asanuma, H., Tani, A., Imamura, R., Komagawa, S., Kanai, T., Takamura, M., Sakata, Y., Kitakaze, M., Haruta, J. I. & Takashima, S. 2023. Restoration of Cardiac Myosin Light Chain Kinase Ameliorates Systolic Dysfunction by Reducing Superrelaxed Myosin. *Circulation,* 147**,** 1902-1918.

Horie, T., Ono, K., Nishi, H., Nagao, K., Kinoshita, M., Watanabe, S., Kuwabara, Y., Nakashima, Y., Takanabe-Mori, R., Nishi, E., Hasegawa, K., Kita, T. & Kimura, T. 2010. Acute doxorubicin cardiotoxicity is associated with miR-146a-induced inhibition of the neuregulin-ErbB pathway. *Cardiovasc Res,* 87**,** 656-64.

Zhu, X. X., Wang, X., Jiao, S. Y., Liu, Y., Shi, L., Xu, Q., Wang, J. J., Chen, Y. E., Zhang, Q., Song, Y. T., Wei, M., Yu, B. Q., Fielitz, J., Gonzalez, F. J., Du, J. & Qu, A. J. 2023. Cardiomyocyte peroxisome proliferator-activated receptor alpha prevents septic cardiomyopathy via improving mitochondrial function. *Acta Pharmacol Sin,* 44**,** 2184-2200.

Palmen, M., Daemen, M. J., De Windt, L. J., Willems, J., Dassen, W. R., Heeneman, S., Zimmermann, R., Van Bilsen, M. & Doevendans, P. A. 2004. Fibroblast growth factor-1 improves cardiac functional recovery and enhances cell survival after ischemia and reperfusion: a fibroblast growth factor receptor, protein kinase C, and tyrosine kinase-dependent mechanism. *J Am Coll Cardiol,* 44**,** 1113-23.

Zhao, D., Zheng, H., Greasley, A., Ling, F., Zhou, Q., Wang, B., Ni, T., Topiwala, I., Zhu, C., Mele, T., Liu, K. & Zheng, X. 2020. The role of miR-711 in cardiac cells in response to oxidative stress and its biogenesis: a study on H9C2 cells. *Cell Mol Biol Lett,* 25**,** 26.

Willis, M. S., Parry, T. L., Brown, D. I., Mota, R. I., Huang, W., Beak, J. Y., Sola, M., Zhou, C., Hicks, S. T., Caughey, M. C., D'Agostino, R. B., Jr., Jordan, J., Hundley, W. G. & Jensen, B. C. 2019. Doxorubicin Exposure Causes Subacute Cardiac Atrophy Dependent on the Striated Muscle-Specific Ubiquitin Ligase MuRF1. *Circ Heart Fail,* 12**,** e005234.

Chen, D. S., Yan, J. & Yang, P. Z. 2022a. Cardiomyocyte Atrophy, an Underestimated Contributor in Doxorubicin-Induced Cardiotoxicity. *Front Cardiovasc Med,* 9**,** 812578.

Chen, Y., Shi, S. & Dai, Y. 2022b. Research progress of therapeutic drugs for doxorubicin-induced cardiomyopathy. *Biomed Pharmacother,* 156**,** 113903.

Liu Y, Asnani A, Zou L, Bentley VL, Yu M, Wang Y, Dellaire G, Sarkar KS, Dai M, Chen HH, Sosnovik DE, Shin JT, Haber DA, Berman JN, Chao W, Peterson RT. Visnagin protects against doxorubicin-

induced cardiomyopathy through modulation of mitochondrial malate dehydrogenase. Sci Transl Med. 2014 Dec 10;6(266):266ra170. doi: 10.1126/scitranslmed.3010189. PMID: 25504881; PMCID: PMC4360984.

Hefti E, Blanco JG. Anthracycline-Related Cardiotoxicity in Patients with Acute Myeloid Leukemia and Down Syndrome: A Literature Review. Cardiovasc Toxicol. 2016 Jan;16(1):5-13. doi: 10.1007/s12012-015-9307-1. PMID: 25616318; PMCID: PMC4514565.

Poonia N, Jadhav NV, Mamatha D, Garg M, Kabra A, Bhatia A, Ojha S, Lather V, Pandita D. Nanotechnology-assisted combination drug delivery: a progressive approach for the treatment of acute myeloid leukemia. Ther Deliv. 2024;15(11):893-910. doi: 10.1080/20415990.2024.2394012. Epub 2024 Sep 13. PMID: 39268925; PMCID: PMC11497954.

Jung, S. H., Hwang, B. H., Shin, S., Park, E. H., Park, S. H., Kim, C. W., Kim, E., Choo, E., Choi, I. J., Swirski, F. K., Chang, K. & Chung, Y. J. 2022. Spatiotemporal dynamics of macrophage heterogeneity and a potential function of Trem2(hi) macrophages in infarcted hearts. *Nat Commun,* 13**,** 4580.

Rizzo, G., Gropper, J., Piollet, M., Vafadarnejad, E., Rizakou, A., Bandi, S. R., Arampatzi, P., Krammer, T., DiFabion, N., Dietrich, O., Arias-Loza, A. P., Prinz, M., Mack, M., Schlepckow, K., Haass, C., Silvestre, J. S., Zernecke, A., Saliba, A. E. & Cochain, C. 2023. Dynamics of monocyte-derived macrophage diversity in experimental myocardial infarction. *Cardiovasc Res,* 119**,** 772-785.

Smart, C. D., Fehrenbach, D. J., Wassenaar, J. W., Agrawal, V., Fortune, N. L., Dixon, D. D., Cottam, M. A., Hasty, A. H., Hemnes, A. R., Doran, A. C., Gupta, D. K. & Madhur, M. S. 2023. Immune profiling of murine cardiac leukocytes identifies triggering receptor expressed on myeloid cells 2 as a novel mediator of hypertensive heart failure. *Cardiovasc Res,* 119**,** 2312-2328.

Grasemann H, Ratjen F. Cystic Fibrosis. N Engl J Med. 2023 Nov 2;389(18):1693-1707. doi: 10.1056/NEJMra2216474. PMID: 37913507.

Mall MA, Burgel PR, Castellani C, Davies JC, Salathe M, Taylor-Cousar JL. Cystic fibrosis. Nat Rev Dis Primers. 2024 Aug 8;10(1):53. doi: 10.1038/s41572-024-00538-6. PMID: 39117676.

Ong T, Ramsey BW. Cystic Fibrosis: A Review. JAMA. 2023 Jun 6;329(21):1859-1871. doi: 10.1001/jama.2023.8120. PMID: 37278811.

Shteinberg M, Haq IJ, Polineni D, Davies JC. Cystic fibrosis. Lancet. 2021 Jun 5;397(10290):2195-2211. doi: 10.1016/S0140-6736(20)32542-3. PMID: 34090606.

Nichols DP, Paynter AC, Heltshe SL, Donaldson SH, Frederick CA, Freedman SD, Gelfond D, Hoffman LR, Kelly A, Narkewicz MR, Pittman JE, Ratjen F, Rosenfeld M, Sagel SD, Schwarzenberg SJ, Singh PK, Solomon GM, Stalvey MS, Clancy JP, Kirby S, Van Dalfsen JM, Kloster MH, Rowe SM; PROMISE Study group. Clinical Effectiveness of Elexacaftor/Tezacaftor/Ivacaftor in People with Cystic Fibrosis: A Clinical Trial. Am J Respir Crit Care Med. 2022 Mar 1;205(5):529-539. doi: 10.1164/rccm.202108-1986OC. PMID: 34784492; PMCID: PMC8906485.

Graeber SY, Vitzthum C, Pallenberg ST, Naehrlich L, Stahl M, Rohrbach A, Drescher M, Minso R, Ringshausen FC, Rueckes-Nilges C, Klajda J, Berges J, Yu Y, Scheuermann H, Hirtz S, Sommerburg O, Dittrich AM, Tümmler B, Mall MA. Effects of Elexacaftor/Tezacaftor/Ivacaftor Therapy on CFTR Function in Patients with Cystic Fibrosis and One or Two *F508del* Alleles. Am J Respir Crit Care Med. 2022 Mar 1;205(5):540-549. doi: 10.1164/rccm.202110-2249OC. PMID: 34936849.

Casey M, Gabillard-Lefort C, McElvaney OF, McElvaney OJ, Carroll T, Heeney RC, Gunaratnam C, Reeves EP, Murphy MP, McElvaney NG. Effect of elexacaftor/tezacaftor/ivacaftor on airway and systemic inflammation in cystic fibrosis. Thorax. 2023 Aug;78(8):835-839. doi: 10.1136/thorax-2022-219943. Epub 2023 May 19. PMID: 37208188.

Schaupp L, Addante A, Völler M, Fentker K, Kuppe A, Bardua M, Duerr J, Piehler L, Röhmel J, Thee S, Kirchner M, Ziehm M, Lauster D, Haag R, Gradzielski M, Stahl M, Mertins P, Boutin S, Graeber SY, Mall MA. Longitudinal effects of elexacaftor/tezacaftor/ivacaftor on sputum viscoelastic properties, airway infection and inflammation in patients with cystic fibrosis. Eur Respir J. 2023 Aug 3;62(2):2202153. doi: 10.1183/13993003.02153-2022. PMID: 37414422.

Graeber SY, Mall MA. The future of cystic fibrosis treatment: from disease mechanisms to novel therapeutic approaches. Lancet. 2023 Sep 30;402(10408):1185-1198. doi: 10.1016/S0140-6736(23)01608-2. Epub 2023 Sep 9. PMID: 37699417.

Ghigo A, Murabito A, Sala V, Pisano AR, Bertolini S, Gianotti A, Caci E, Montresor A, Premchandar A, Pirozzi F, Ren K, Della Sala A, Mergiotti M, Richter W, de Poel E, Matthey M, Caldrer S, Cardone RA, Civiletti F, Costamagna A, Quinney NL, Butnarasu C, Visentin S, Ruggiero MR, Baroni S, Crich SG, Ramel D, Laffargue M, Tocchetti CG, Levi R, Conti M, Lu XY, Melotti P, Sorio C, De Rose V, Facchinetti F, Fanelli V, Wenzel D, Fleischmann BK, Mall MA, Beekman J, Laudanna C, Gentzsch M, Lukacs GL, Pedemonte N, Hirsch E. A PI3Kγ mimetic peptide triggers CFTR gating, bronchodilation, and reduced inflammation in obstructive airway diseases. Sci Transl Med. 2022 Mar 30;14(638):eabl6328. doi: 10.1126/scitranslmed.abl6328. Epub 2022 Mar 30. PMID: 35353541; PMCID: PMC9869178.

Lobo MJ, Amaral MD, Zaccolo M, Farinha CM. EPAC1 activation by cAMP stabilizes CFTR at the membrane by promoting its interaction with NHERF1. J Cell Sci. 2016 Jul 1;129(13):2599-612. doi: 10.1242/jcs.185629. Epub 2016 May 20. PMID: 27206858.

Loureiro CA, Matos AM, Dias-Alves Â, Pereira JF, Uliyakina I, Barros P, Amaral MD, Matos P. A molecular switch in the scaffold NHERF1 enables misfolded CFTR to evade the peripheral quality control checkpoint. Sci Signal. 2015 May 19;8(377):ra48. doi: 10.1126/scisignal.aaa1580. PMID: 25990958.

Lopes-Pacheco M. CFTR Modulators: The Changing Face of Cystic Fibrosis in the Era of Precision Medicine. Front Pharmacol. 2020 Feb 21;10:1662. doi: 10.3389/fphar.2019.01662. PMID: 32153386; PMCID: PMC7046560.

Carnegie GK, Smith FD, McConnachie G, Langeberg LK, Scott JD. AKAP-Lbc nucleates a protein kinase D activation scaffold. Mol Cell. 2004 Sep 24;15(6):889-99. doi: 10.1016/j.molcel.2004.09.015. PMID: 15383279.

Swiatecka-Urban A, Duhaime M, Coutermarsh B, Karlson KH, Collawn J, Milewski M, Cutting GR, Guggino WB, Langford G, Stanton BA. PDZ domain interaction controls the endocytic recycling of the cystic fibrosis transmembrane conductance regulator. J Biol Chem. 2002 Oct 18;277(42):40099-105. doi: 10.1074/jbc.M206964200. Epub 2002 Aug 7. PMID: 12167629.

Cihil KM, Ellinger P, Fellows A, Stolz DB, Madden DR, Swiatecka-Urban A. Disabled-2 protein facilitates assembly polypeptide-2-independent recruitment of cystic fibrosis transmembrane conductance regulator to endocytic vesicles in polarized human airway epithelial cells. J Biol Chem. 2012 Apr 27;287(18):15087-99. doi: 10.1074/jbc.M112.341875. Epub 2012 Mar 7. PMID: 22399289; PMCID: PMC3340218.

Gee HY, Noh SH, Tang BL, Kim KH, Lee MG. Rescue of ΔF508-CFTR trafficking via a GRASP-dependent unconventional secretion pathway. Cell. 2011 Sep 2;146(5):746-60. doi: 10.1016/j.cell.2011.07.021. PMID: 21884936.

Olayioye MA, Noll B, Hausser A. Spatiotemporal Control of Intracellular Membrane Trafficking by Rho GTPases. Cells. 2019 Nov 21;8(12):1478. doi: 10.3390/cells8121478. PMID: 31766364; PMCID: PMC6952795.

Diggins NL, Kang H, Weaver A, Webb DJ. α5β1 integrin trafficking and Rac activation are regulated by APPL1 in a Rab5-dependent manner to inhibit cell migration. J Cell Sci. 2018 Mar 6;131(5):jcs207019. doi: 10.1242/jcs.207019. PMID: 29361527; PMCID: PMC5897716.

Zhang J, Fu L, Wang H, Yonemura A, Semba T, Yasuda-Yoshihara N, Nishimura A, Tajiri T, Tong Y, Yasuda T, Uchihara T, Yamazaki M, Okamoto Y, Yamasaki J, Nagano O, Baba H, Ishimoto T. RAC1-mediated integrin alpha-6 expression in E-cadherin-deficient gastric cancer cells promotes interactions with the stroma and peritoneal dissemination. Cancer Lett. 2024 Jun 1;591:216901. doi: 10.1016/j.canlet.2024.216901. Epub 2024 Apr 17. PMID: 38641311.

Magalhaes YT, Farias JO, Silva LE, Forti FL. GTPases, genome, actin: A hidden story in DNA damage response and repair mechanisms. DNA Repair (Amst). 2021 Apr;100:103070. doi: 10.1016/j.dnarep.2021.103070. Epub 2021 Feb 13. PMID: 33618126.

Rozengurt E. Protein kinase D signaling: multiple biological functions in health and disease. Physiology (Bethesda). 2011 Feb;26(1):23-33. doi: 10.1152/physiol.00037.2010. PMID: 21357900; PMCID: PMC4381749.

di Blasio L, Droetto S, Norman J, Bussolino F, Primo L. Protein kinase D1 regulates VEGF-A-induced alphavbeta3 integrin trafficking and endothelial cell migration. Traffic. 2010 Aug;11(8):1107-18. doi: 10.1111/j.1600-0854.2010.01077.x. Epub 2010 May 6. PMID: 20477989.

Subramanian A, Capalbo A, Iyengar NR, Rizzo R, di Campli A, Di Martino R, Lo Monte M, Beccari AR, Yerudkar A, Del Vecchio C, Glielmo L, Turacchio G, Pirozzi M, Kim SG, Henklein P, Cancino J, Parashuraman S, Diviani D, Fanelli F, Sallese M, Luini A. Auto-regulation of Secretory Flux by Sensing and Responding to the Folded Cargo Protein Load in the Endoplasmic Reticulum. Cell. 2019 Mar 7;176(6):1461-1476.e23. doi: 10.1016/j.cell.2019.01.035. PMID: 30849374.

Capurro V, Tomati V, Sondo E, Renda M, Borrelli A, Pastorino C, Guidone D, Venturini A, Giraudo A, Mandrup Bertozzi S, Musante I, Bertozzi F, Bandiera T, Zara F, Galietta LJV, Pedemonte N. Partial Rescue of F508del-CFTR Stability and Trafficking Defects by Double Corrector Treatment. Int J Mol Sci. 2021 May 17;22(10):5262. doi: 10.3390/ijms22105262. PMID: 34067708; PMCID: PMC8156943.

Zhang X, Connelly J, Chao Y, Wang QJ. Multifaceted Functions of Protein Kinase D in Pathological Processes and Human Diseases. Biomolecules. 2021 Mar 23;11(3):483. doi: 10.3390/biom11030483. PMID: 33807058; PMCID: PMC8005150.

Bayer AL, Zambrano MA, Smolgovsky S, Robbe ZL, Ariza A, Kaur K, Sawden M, Avery A, London C, Asnani A, Alcaide P. Cytotoxic T cells drive doxorubicin-induced cardiac fibrosis and systolic dysfunction. Nat Cardiovasc Res. 2024 Aug;3(8):970-986. doi: 10.1038/s44161-024-00507-y. Epub 2024 Jul 17. PMID: 39196030.

Nikonova AS, Deneka AY, Kiseleva AA, Korobeynikov V, Gaponova A, Serebriiskii IG, Kopp MC, Hensley HH, Seeger-Nukpezah TN, Somlo S, Proia DA, Golemis EA. Ganetespib limits ciliation and cystogenesis in autosomal-dominant polycystic kidney disease (ADPKD). FASEB J. 2018 May;32(5):2735-2746. doi: 10.1096/fj.201700909R. Epub 2018 Jan 10. PMID: 29401581; PMCID: PMC5901382.

Durand N, Borges S, Storz P. Functional and therapeutic significance of protein kinase D enzymes in invasive breast cancer. Cell Mol Life Sci. 2015 Nov;72(22):4369-82. doi: 10.1007/s00018-015-2011-2. Epub 2015 Aug 8. PMID: 26253275; PMCID: PMC4618102.

Turner MJ, Matthes E, Billet A, Ferguson AJ, Thomas DY, Randell SH, Ostrowski LE, Abbott-Banner K, Hanrahan JW. The dual phosphodiesterase 3 and 4 inhibitor RPL554 stimulates CFTR and ciliary beating in primary cultures of bronchial epithelia. Am J Physiol Lung Cell Mol Physiol. 2016 Jan 1;310(1):L59-70. doi: 10.1152/ajplung.00324.2015. Epub 2015 Nov 6. PMID: 26545902.

RINGRAZIAMENTI

Attenzione! Questo non vuole essere un semplice elenco di ringraziamenti. Ma soprattutto, non vuole essere formale. Piuttosto, si tratta di un sincero riconoscimento verso tutte le persone che, in modi diversi, hanno avuto un impatto su questo lavoro. Perché, in fondo, non si è trattato solo di ricerca.

Ho anche deciso di aggiungere qualche considerazione qua e là – così, perché mi andava – spero non troppo fuorviante o strappalacrime, viste le circostanze. Lo so, come al solito sono stato un po' prolisso. Capisco se non avete tempo o voglia di leggere tutto. Però considerate che non ho usato ChatGPT e ci ho messo una vita: se non leggeste, il mio sforzo sarebbe vano! Magari dedicatevi solo alla vostra parte – sempre che non mi sia dimenticato di voi – o insomma, fate un po' come vi pare.

Eccoci qua, giunti al termine del dottorato. Il più importante titolo accademico. Chi l'avrebbe mai detto! Non fraintendetemi, tutto sommato so di essere sveglio (rimango umile ☺). Eppure, non ci avrei mai puntato troppo, né sperato. Soprattutto quando – sono sincero - la prospettiva di fare ricerca era solo una strategia di ripiego, soprattutto ai tempi della triennale. Un piano "B". Anzi, forse addirittura "C" o "D". Ancor di più, quando tutto era incerto e le cose andavano male. Forse non tutti lo sanno, ma volevo fare medicina. E per quanto mi sia sforzato di non pensarci, questa cosa non ha mai smesso di tormentarmi. Credetemi se vi dico: "Urca se è (stata) dura!". Troppo spesso e con insistenza ho pensato di essere fuori strada o di non essere all'altezza, di non avere un futuro e quindi di voler mollare (e lo penso tuttora, a volte). Eh sì, il *Dr. Mergiotti* non è solo l'arrogante, sicuro, saccente, rompiscatole che deve quasi sempre – dico quasi perché sento anche di essere un po' migliorato – pontificare e avere ragione, correggendo con frasi del tipo: "Eh no, quello funziona così…"; "Eh no, devi sapere che…" etc. etc. gne gne gne. Me la sono anche vista brutta, a tratti.

Non senza paure e perplessità, ho accettato la proposta di una borsa di dottorato e, mosso da chissà quale motivazione, sono andato avanti. Grazie anche, e soprattutto, alle persone che ho avuto intorno. Ma forse non si tratta solo di questo. Mi piace pensare che sia anche grazie ad un qualcosa che considero la mia personale "super etica". Una super etica del tipo:

non importa cosa, voglio provare a dare il mio contributo alla medicina, anche senza chissà quale ambizione. Anche senza essere un medico.

Parliamoci chiaro, nel nostro campo salvare le persone, magari trovando una terapia, può cambiare il mondo. Ma è roba da supereroi. E io non sono un supereroe. Credo, tuttavia, di avere delle buone possibilità di lasciare il segno. Più che altro, di porre le basi per gli altri, grazie sia ai miei successi che ai miei fallimenti. Mi immagino un po' lo staff che lavora dietro le quinte, nei teatri. Mica tutti devono salire sul palco per fare uno spettacolo! Del resto, si tratta anche di "*setting the stage*", come si dice in gergo. Mi ci è voluto un po', lo ammetto, ma forse ora mi accontento lo stesso se non vado a Stoccolma a prendere il Nobel. O forse no, chissà! ☺

Dopo questa mia premessa, di cui immagino non fregherà niente a nessuno, passerei quindi a riconoscere i meriti delle persone.

Innanzitutto, desidero ringraziare i due revisori di questo lavoro, il Dr. Carlos Farinha e il Dr. Wouter Meijers, per aver accettato di correggere la mia tesi. Il loro feedback critico è stato uno stimolo a rivedere, riflettere e affinare il mio lavoro, rendendolo più solido e completo.

Un mio profondo ringraziamento va alla mia mentore, Alessandra Ghigo, per essere stata l'unica a rendersi disponibile, quando ancora in magistrale e nel pieno della pandemia, era molto difficile entrare in un laboratorio. Negli anni, ho visto in lei una guida solida e scientificamente brillante, sempre pronta ad ascoltarmi e a trovare soluzioni. Grazie per aver avuto pazienza e fiducia con me, facendomi sentire prima parte integrante dei progetti e, piano piano, una figura importante all'interno gruppo. Grazie soprattutto a lei, ho conosciuto grandi scienziati e collaborato con super ricercatori. Ho trovato nel suo lab un ambiente estremamente stimolante con persone molto preparate, sia giovani che senior. Spero di aver mantenuto gli standard alti!

Non posso che ringraziare profondamente anche il Prof. Emilio Hirsch per avermi spronato costantemente e per aver sempre condiviso con me il suo prezioso feedback. Confrontarmi con lui in questi anni mi ha sempre aiutato ad avere nuove idee, ma anche – e forse soprattutto – a sviluppare uno spirito critico, qualità fondamentale per fare questo lavoro. Certo, è evidente che parlarci alle sei o sette di sera, proprio quando sono pronto per uscire o mentre sto sistemando le slides per i suoi talk... beh, non è sempre piacevole. Ma credo che, in fondo, non si possa fare altrimenti e me lo faccio andare bene lo stesso.

Un riconoscimento particolare va a Michela Noseda e Yue Qin, per il lavoro e per l'enorme supporto nell'analisi bioinformatica, un mondo che era completamente inesplorato per me. Yue, hai mostrato con me una pazienza incredibile, gran parte di ciò che ho imparato dell'analisi e del mondo *single-cell* lo devo soprattutto a te. Ringrazio quindi tutti i collaboratori che hanno permesso di realizzare questo lavoro.

Grazie anche a tutti i membri, attuali e passati, dei Lab Martini e Gulluni, per essere stati sempre molto disponibili e aperti alla discussione. Grazie quindi a tutte le persone dell'MBC che mi hanno aiutato in questi anni.

Voglio poi ringraziare le persone del mio lab, passate e presenti. Grazie a Polly per avermi insegnato e per avermi dato un metodo scientifico di base. Non è stato facile affrontare le tante difficoltà negli anni, soprattutto nell'ultimo periodo, e forse io per primo, a volte, non sono stato bravo a gestire le dinamiche e a saper comunicare. Diciamoci la verità, forse non è andata come volevamo, e ci sta. Comunque, ti sarò sempre grato per gli insegnamenti e per il supporto, e ti auguro il meglio nella tua nuova avventura.

Grazie di cuore a Jens, per aver dato un contributo importante al nostro progetto, con grande motivazione e rigore scientifico. E' bello avere un solido alleato su cui contare. Grazie quindi anche a te per gli insegnamenti, sei forte.

Grazie ad Angela, per il tuo "sempreverde ottimismo", qualità davvero rara in questo ambiente; a Janki, la persona che ho visto crescere e maturare di più nel nostro lab; a Giulia, esempio di passione e determinazione; a Sophie, con cui mi sono più confrontato e che mi ha più sostenuto nell'ultimo periodo in lab. Mi manca davvero tanto. Grazie a Michele, Ivan, George studenti e studentesse. Grazie a tutti per avermi aiutato nella mia attività di ricerca.

Grazie soprattutto a Paola e Giovanni, bravissimi studenti e fedeli compagni di ricerca. Il vostro contributo per me è molto importante. E' bello vedervi crescere e migliorare, lavorando con criterio e consapevolezza crescenti. Continuate così e sono sicuro raggiungerete grandi obiettivi. Mi scuso se a volte sono stato poco disponibile, ma per voi cerco di esserci sempre. Vi meritate il meglio nel lavoro e nella vita!

Ringrazio anche i ragazzi di TLB, Infermieristica e Biotech Mediche, a cui ho fatto lezione in questi anni. Grazie a loro ho capito quanto la didattica sia importante, ma al tempo stesso difficile. Soprattutto quando bisogna coinvolgere. E' anche grazie a loro se ho guadagnato un po' di "*self-confidence*" nel presentare, attraverso un bel ripasso – bisogna dire necessario - di biologia. E vi dirò di più: ho anche realizzato che mi piace insegnare! Per rimanere in tema, mi sento di dare un piccolo consiglio a tutti i docenti: usate le parolacce, funziona tantissimo per richiamare l'attenzione.

Volevo anche ringraziare tutti i volontari della delegazione FFC di Moncalieri e Nichelino, in particolare Anna e Chiara, e la piccola Mia, paziente di fibrosi cistica. Lo sforzo e l'impegno che mettete nelle vostre attività è semplicemente straordinario. Parte di questo lavoro è stato possibile anche grazie alla vostra raccolta fondi. Per me è stato un piacere conoscervi e un onore venire con voi nelle scuole di Torino a parlare di fibrosi cistica, raccontando quello che facciamo. Troppo spesso siamo concentrati solo sugli esperimenti e perdiamo di vista il "perché" e il "per chi" facciamo questo lavoro. Mi avete ricordato l'importanza della ricerca, ma soprattutto del fare informazione, comunicando alle generazioni più giovani: un pubblico

diverso dal solito, ma credo con il più grande potenziale per cambiare le cose. Ammetto che a volte pensare a voi mi ha dato la forza per andare avanti. Grazie dal profondo.

Veniamo adesso alle persone vicine nella vita. Grazie agli amici di sempre, quelli di *Onlus* e di *Geppetto*. Non è facile rimanere vicini ma è bello sapere che ogni volta che vi vedo niente o quasi è cambiato.

Vorrei ringraziare Remmi, perché è stato il vero tramite col mondo del Padel, *el mejor deporte del mundo*! E' anche grazie a te che sono uscito da un brutto loop in cui la mia unica attività quotidiana era lavorare. Si, perché bere dopo il lavoro non vale come attività extra - sono simpatico, lo so. "Stay tuned", saremo prossimi sui grandi schermi, a giocare il Premier Padel.

Grazie a Giovanni, che ogni tanto fa la sua sortita da Genova e viene a portarmi allegria e spensieratezza come solo lui sa fare. Fondamentale. Grazie alle mie amiche Francesca ed Elena, per esserci sempre, per essere semplicemente il confronto di cui ho bisogno. Non perdiamoci mai.

Grazie ad Alessandro, non solo per l'amico che è, ma anche per la guida. Grazie per avermi dato, negli ultimi anni, la chiave per scoprire un mondo nuovo e bellissimo. Hai portato una sorta di rivoluzione nella mia testa. Sentivo che forse ci eravamo un po' persi dopo Teramo. Ritrovarsi però è stata un po' quella cosa che rifai dopo tanto e pensi "ma come ho fatto senza?". Prima a Parco Dora, poi su quella montagna freddissima in Toscana, per poi finire in mezzo ai boschi della Slovenia. Non nascondo che mi capita spesso di chiedermi, nelle situazioni più svariate: "cosa farebbe o direbbe Alessandro?". Quindi oltre l'amico, sei anche fonte di ispirazione quotidiana. Se ci pensi, mi sono pure fatto il mullet dopo che lo hai fatto tu. Si scherza, a *Marcolino* serviva un "taglio da festival", come dice mamma.

E ora parlo agli amici nuovi. Inaspettatamente, molte belle persone sono entrate nella mia vita in questi anni.

Alla famiglia di feste e gruppo *Atlas-Drops*, nonché *Schicchera crew,* grazie per avermi aiutato, in circostanze quantomeno insolite, a respirare un'energia nuova, a riscoprirmi e capire cosa non andasse, ad evadere, anche solo per un attimo, dalle fatiche di questo lavoro. Vi voglio un cucchiaione di bene ☺.

Ad Albo e Albi, è stato pesante quando siete andati via e ho brancolato nel buio per un po'. Ma ero anche consapevole che ormai vi avevo trovato e che ci sareste stati sempre, per confronti di vita e di scienza. Grazie ragazzi, è sempre bello riunirsi. Non vedo l'ora di vedervi spiccare il volo.

Grazie a Lollo per essere il mio amichetto a Torino. Non nego che mi stessi un po' antipatico quando ti ho conosciuto in magistrale. Poi, chissà come, insieme a un famigerato duo musicale di nome *dilinoediseta*, sei stato una delle scoperte più belle di questi anni. Siamo diventati i *Fantastici 4*! Stento ancora a crederci. Chissà se andremo un giorno a Gardaland.

Scusa se ti copio la forma: al Dr. Prever, grazie per avermi insegnato a usare il microiniettore, per aiutarmi con i microscopi – spero sempre con meno arroganza la prossima volta. Ti ringrazio quindi per essere una fonte costante di confronto, ma anche di ispirazione, nonché una delle persone più brillanti che io abbia mai incontrato.

A Lollo, grazie per essere l'amico che sei. Ci auguro almeno altre mille di quelle piacevoli camminate per tornare a casa, magari solo senza pioggia. Grazie anche alla sua *Cumpa*, per avermi trattato fin da subito come l'amico di sempre. Voglio bene anche a voi.

Grazie a Lorenza e Lucia per aver permesso di integrarmi come mai avrei immaginato in questa città. Avete creduto in me (soprattutto Lorenza all'inizio) e mi avete scelto come amico. Siete forse le persone a cui devo di più se ho una vita a Torino adesso. Grazie per suggerirmi spesso la cosa migliore, ricordandomi di tenere di più a me stesso, di ridurre e rimandare.

Ma se c'è un merito che vi riconosco più di tutti, è quello di avermi aiutato a (ri)trovare un po' la mia identità. Grazie a voi, ho imparato a dare importanza a certe cose, ho scoperto nuove realtà e fatto miei nuovi valori, davvero. Ho conosciuto anche persone carine, alcune delle quali sono diventate amici e amiche. Penso, per esempio, a Sara, che ho avuto modo di conoscere meglio grazie a Lucia, o ai ragazzi di *Curva* e di San Salvario, con cui ho condiviso tanti momenti di vita – anche importanti. In fondo, è così che gli amici fanno la differenza, no? Sempre: "*Riduci&Rimanda*" come filosofia di vita - ogni tanto me ne dimentico, scusate! Cercherò di fare del mio meglio.

Ah, quasi dimenticavo! Mi raccomando, seguite su IG @*dilinoediseta*. Duo musicale eccelso.

Grazie a Irene, perché dopo tutti questi anni, rimane la mia più grande certezza. Grazie per prenderti cura di me, per non darmi mai per scontato, per l'entusiasmo e l'energia che hai. Ti ringrazio per aver sempre creduto in me in questi anni, soprattutto quando sconforto e paure coprivano ogni cosa. Grazie per essere cresciuta con me, fidandoti e ascoltandomi sempre, anche quando era oggettivamente complicato. Saperti poi rimettere in gioco negli anni è stata la cosa più bella che hai fatto con me, e la considero la tua più grande prova d'amore. Non immagini quanto sia fiero della donna che sei e della dottoressa salva-vite che sei diventata.

Ancora oggi, più che mai, sono convinto che salire su quel bus per Roma e venire a bussare alla tua porta in via Tiburtina sia stata la scelta migliore che abbia mai fatto.

Ringrazio anche Ida e Fortunio, per avermi accolto in Sicilia come mai mi sarei immaginato, facendomi sentire sempre a casa. Non sapete quanto significhi per me! Anche voi, a modo vostro, mi avete aiutato in questi anni a ritrovare la pace quando era necessario, grazie anche alla vostra magnifica terra.

Grazie alla mia famiglia. A Silvia e Valeria per essere sempre presenti, forti, genuine e sagge, per essere semplicemente le persone che siete. E grazie anche a mamma e papà per il supporto spirituale ma anche economico. Senza di voi, tutto questo non sarebbe stato possibile. Lo so, forse mi volevate violinista, soprattutto mamma. Anche papà, ti fermavi sempre ad ascoltarmi quando scendevi dallo studio prima di cena. Immagino che sentire

parlare di cardiotossicità da chemioterapici sia meno entusiasmante che ascoltare il concerto per violino e orchestra di Beethoven, ma le cose sono andate così, *c'est la vie!* Ho cercato di dare un senso ai vostri sacrifici e spero di esserci riuscito. Quindi alla mia famiglia, ancora una volta, grazie per l'amore incondizionato che mi mostrate e scusate per tutti i casini che combino. Vi voglio bene, anche se non lo faccio sempre vedere.

Infine, un pensiero va a chi, anche senza saperlo, ha lasciato un segno in questo percorso. Molti piccoli gesti hanno avuto un impatto, e per questo sono grato.

Sayonara,

dal *Dr. Mergiotti* e *Marcolino*, entrambi PhD ora.